ABSTRACT

O'BRIEN, SEAN EDWARD. Sensitivity Analysis of Neutron Multiplicity Counting Statistics of a Subcritical Plutonium Benchmark using First-Order Perturbation Theory. (Under the direction of Dr. John Mattingly.)

It is important to estimate the sensitivity and uncertainty of measured and computed detector responses in subcritical experiments and simulations. These uncertainties arise from the physical construction of the experiment, from uncertainties in the transport parameters, and from counting uncertainties. In particular, in subcritical experiments the moments of the neutron multiplicity counting distribution are geometrically sensitive to the induced fission neutron yield distribution. Perturbation theory enables sensitivity analysis and uncertainty quantification (SA/UQ) on integral quantities like detector responses. The aim of our work is to apply SA/UQ to statistics of subcritical neutron multiplicity counting distributions. Current SA/UQ methods have only been applied to mean detector responses and the k-effective eigenvalue. For multiplicity counting experiments, knowledge of the higher order counting moments and their uncertainties are essential for a complete SA/UQ analysis. We apply perturbation theory to compute the sensitivity of neutron multiplicity counting moments of arbitrarily high order. Each moment is determined by solving an adjoint transport equation with a source term that is a function of the adjoint solutions for lower order moments. This enables moments of arbitrarily high order to be sequentially determined, and it shows that each moment is sensitive to the uncertainties of all lower order moments. We derive forward transport closing equations that are functions of the forward flux and lower order moment adjoint fluxes. We verify our calculations for the first two moments by comparison with multiplicity counting measurements of a subcritical plutonium metal sphere. For the first two moments, the most influential parameters are ranked and the validity of linear perturbation theory demonstrated by examining the series truncation error. This enables a detailed sensitivity and uncertainty analysis of subcritical multiplicity counting measurements of fissionable material based on Boltzmann transport theory.

Sensitivity Analysis of Neutron Multiplicity Counting Statistics of a Subcritical Plutonium Benchmark using First-Order Perturbation Theory

by
Sean Edward O'Brien

A dissertation submitted to the Graduate Faculty of
North Carolina State University
in partial fulfillment of the
requirements for the Degree of
Doctor of Philosophy

Nuclear Engineering

Raleigh, North Carolina

2016

APPROVED BY:

Dr. Dmitriy Anistratov

Dr. Yousry Azmy

Dr. Ralph Smith

Dr. John Mattingly
Chair of Advisory Committee

DEDICATION

To my parents.

BIOGRAPHY

Sean Edward O'Brien was born in 1987 to Wayne and Martha O'Brien. He grew up in Farmville, VA and attended Prince Edward County Schools until 2005. He moved to Harrisonburg, Va to pursue a B.S. in Physics at James Madison University where he pursued undergraduate research on characterizing large multi-segmented NaI spectrometers. Upon graduation in 2009 he moved to Raleigh, NC to obtain a M.S. in Nuclear Engineering concerning error estimators of the neutron transport equation at North Carolina State University in 2012.

ACKNOWLEDGEMENTS

I would like to thank my advisor, my committee members, Dr. Jeff Favorite, and my friends/colleagues for their help and support. And Dr. Anistratov for suggesting the forward closing equation approach.

TABLE OF CONTENTS

LIST OF TABLES

LIST OF FIGURES

Chapter 1

Introduction

1.1 Introduction

Non-multiplying (i.e., non-fissile) neutron sources are fully characterized by the mean of the neutron multiplicity counting distribution because all higher order moments are explicit functions of the mean. Where the q^{th} order factorial moment is the average to the q^{th} power,

$$\overline{n(n-1)\dots(n-q+1)} = \overline{n}^q \tag{1.1}$$

A neutron multiplicity counting experiment measures the probability of detecting a number of neutrons during a gate interval [1]. The neutron multiplicity counting distribution is accumated over many gates as seen in Figure 1.1.

In non-multiplying systems, all neutron events are independent and the neutron multiplicity counting distribution exhibits Poisson statistics. The Poisson distribution is,

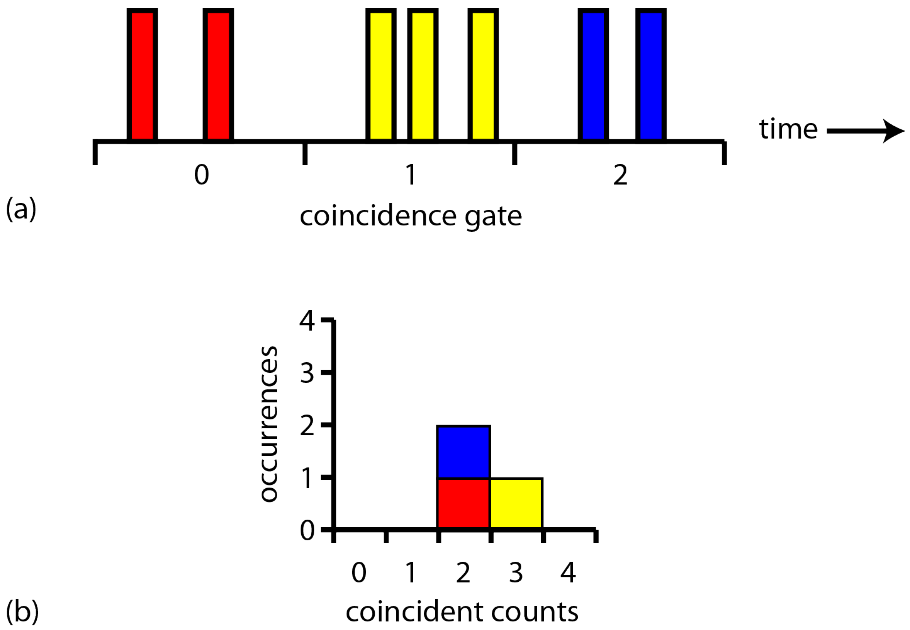

Figure 1.1: Multiplicity counting histogram is accumated over many coincident gates [2].

$$p(n;\overline{n}) = \frac{(\overline{n})^n}{n!}e^{-\overline{n}} \tag{1.2}$$

, where $\overline{n}$ is the average number of events and $p(n;\overline{n})$ is the probability of observing n events. In a system with intrinsic neutron multiplicity, either through spontaneous fission, induced fission, or $(n,2n)$ type reactions, coincident neutrons may be correlated. In fission chain-reactions, the current neutron state is dependent on the history of the fission chain-reaction. These multiplying systems introduce detectable time correlations between neutrons, such that the multiplicity counting distribution cannot be described by Poisson statistics; the higher order moments must be explicitly determined in addition to the mean [3].

In this dissertation, the first three moments are determined: the mean (singles), the second factorial moment (doubles), and the third factorial moment (triples) [1]. Passive neutron multiplicity counting is an effective tool in the nondestructive assay of special nuclear material (SNM) because knowledge of the first three moments enables one to determine the spontaneous fission rate, self-multiplication, and (α, n) rate; i.e. the kinetics parameters of a fissile system, such that an effective mass of the SNM may be estimated [4]. Measuring the first three moments provides three equations for three unknowns, providing a self-contained solution, provided the detector efficiency is well characterized [1].

The calculation of singles is possible with standard deterministic transport or Monte Carlo methods. The determination of doubles and triples requires additional consideration. Often point kinetics models are used to calculate higher moments, but we consider the full phase-space treatment by solving for the moments (singles, doubles, and triples) of the stochastic transport equation, a probabilistic description of the neutron field. The moment equations from the stochastic transport equation are forward and adjoint transport equations with unique fixed sources [5]. These equations can be solved by any deterministic transport code capable of forward/adjoint fixed source subcritical calculations. The resulting expressions for the moments of the neutron multiplicity counting distribution are inner products between forward and adjoint solutions.

The moments are defined as inner products, which enable us to consider the sensitivity of the moments to the transport parameters using perturbation theory. Previously, only the sensitivity of the mean, reaction rates, and eigenvalues (e.g. k_{eff}) were considered. We develop a sensitivity analysis (SA) method for arbitrarily high order moments of the neutron multiplicity counting distribution that uses deterministic transport solutions with special fixed sources. Knowledge of the sensitivity of the moments of the neutron multiplicity counting distribution will enable uncertainty quantification of measurements of SNM and will enable measurements of SNM to inform the evaluated nuclear data, based on Boltzmann transport theory. Now, we consider the prior work that provides the foundation of this dissertation.

1.2 Prior Work

In [1], the foundations of neutron multiplicity counting are described. Passive neutron counting experiments are a valuable nondestructive assay tool because neutrons are highly penetrating and are difficult to shield. The simplest neutron counting measurement is the total count rate, i.e. singles, and provides minimal characterization of SNM because N measured quantities are needed to determine N-unknowns. Singles counting is useful for already well characterized samples, where good assumptions can be made to decrease the number of assay unknowns [1]. Neutron coincidence counting allows singles and doubles to be measured, allowing two sample unknowns to be determined, but it increases the measurement time and cost of the detector. Doubles counting is ineffective for highly impure SNM samples, but methods have been developed to determine the mass of the sample and sample self-multiplication, by assuming the (α, n) rate is known [6], or by assuming the self-multiplication determining the mass and (α, n) rate [7]. Both count rate and coincidence counting methods are limited by the quality of the assumptions.

Neutron multiplicity counting allows singles, doubles, and triples to be measured, and is effective at determining three SNM parameters, but the detector cost and measurement time are increased. In principle the fourth moment and beyond can be obtained from the multiplicity counting distribution, but, that is impractical due to increasingly poor signal to noise ratios requiring long counting times to resolve. To reduce assay times, neutron multiplicity counters are designed to be highly efficient because the detection of triples is proportional to the cube of the detector efficiency [8]. Multiplicity counters are often 4π detectors, where the sample is placed within a detector well. Common designs rely on ^3He proportional counters embedded in a neutron moderator, such as paraffin and polyethylene, because of the large ^3He thermal cross-section. The interface between the sample and detector is often lined with a neutron absorber, such as cadmium, to diminish detector-source interaction and to remove thermal source neutrons to reduce the die-away time in the detector [9]. The die-away time τ appears in the Rossi-α distribution as an exponential and describes the exponential die-away of real coincident neutrons R superimposed with neutrons whose coincidence is accidental A,

$$N(t) = A + Re^{-t/\tau} \tag{1.3}$$

where, N is the total rate. Multiplicity counters are designed to have generally constant efficiencies with respect to neutron energies, particularly around 1 MeV, because the fission spectrum peaks at 1 MeV and averages around 1.5 MeV. Several codes model these counting experiments using a combination of Monte Carlo methods, for the detector, and point source models [10]. Hybrid Monte Carlo and analytical models of neutron multiplicity counting experiments were also developed in [11]. Using assay variance as a figure-of-merit, simulations were developed to model experiments and identify significant design parameters for future multiplicity counters in [12].

The mathematics used to model the neutron multiplicity counting experiment has chiefly relied on point kinetics models. These models require measurements of the neutron multiplicity distribution $p(\nu)$. Initial work on determining the variations in fission neutron yield was undertaken by Feynman, who developed the excess variance (Feynman-Y), as a measure of the dispersion of the number of neutrons from fission [13]. Measurements of the energy dependence of the fission neutron yield distribution were performed in [14]. Early work in determining the mathematical form for the distribution of fission neutron numbers, p_ν, was explored by Terrell in [15], who showed the cumulative probability of observing a number of fission neutrons is described by a Gaussian distribution. Verbeke, et al., developed software that used volumes of experimental multiplicity data to generate libraries of the fission yield distribution [16], whose distributions are utilized in this work. Boldeman and Hines analyzed prior multiplicity data and corrected the distributions by accounting for the time correlations between induced fissions following thermal neutron fissions and spontaneous fission [17].

Using the the multiplicity distributions of induced and spontaneous fissions, point models can be developed. The balance of neutron probabilities (e.g. fission, capture and leakage) are developed by Stewart in [9], to derive the leakage multiplication of the system. The concept of superfission, that treats induced fission neutrons as being simultaneously emitted with the inducing spontaneous fission or (α, n) neutron, regardless of the length of the fission chain-reaction, was developed by Boehnel in [18]. Superfission proved to be a good assumption given the long die-away time of neutrons in a multiplicity counter. The number of fission neutrons emitted and the fission neutron energy spectrum was shown to be uncorrelated, implying that the emission energy is generally constant, was shown in [19]. Work is underway to reevaluate the standard assumption that fission neutrons are uncorrelated in energy and in number [20]. Langner and Russo formulated a geometrically sensitive correction of the multiplication by correlating the multiplicity with nuclide density and average cord length in [21]. Cifarelli and Hage developed point model analytical expressions for the moments of the neutron multiplicity counting distribution in [22] and enabled a three parameter neutron signal correlation model, using neutron singles, doubles, and triples, to assay fissile material in [23]. The book by Pazsit and Pal encapsulates much of the theoretical development of neutron fluctuations and branching processes, for both point models and the full phase-space Boltzmann transport treatment considered in this dissertation [24].

To describe the stochastic nature of neutron multiplicity experiments, one requires information beyond the mean quantities described by the familiar Boltzmann neutron transport equation. Pal developed a probabilistic treatment of the stochastic processes of the neutron field based on transport theory in [25] using the theory of generating functions. Bell derived a probability distribution of neutrons and precursors in [26]. Lewins developed a direct derivation of Pal and Bell's equations in [27]. Muñoz-Cobo formulated the interaction of the stochastic neutron field with a neutron detector, developed the corresponding moment equations for the detected multiplicity distribution in [5], and considered the effects of delayed neutrons in [28]. The equations for the moments of the neutron multiplicity distribution were in the form of forward and downwardly coupled adjoint transport equations with fixed sources. Prasad and Snyderman showed that the neutron multiplicity distribution is described by generalized Poisson statistics, where higher order moments are not an explicit function of the mean [3]. Fichtl and Baker calculated the moments of the neutron population using deterministic transport in [29]. Mattingly solved the first two moment equations to model experimental neutron multiplicity counting data in [4].

Sensitivity analysis methods are prevalent in nuclear engineering and are commonly brought to bear to enable the uncertainty quantification of reaction rates and k-eigenvalue calculations [30]. These methods rely on perturbation theory and the adjoint form of the transport equation to determine the sensitivity of integral quantities to model parameters, in many works including [31],[30],[32]. General methods and applications of uncertainty quantification, some enabled by adjoint/perturbation theory, are well developed by Smith in [33]. Evans and Mattingly discovered inaccuracies in $\overline{\nu}$ by applying perturbation theory to the mean of the neutron multiplicity distribution [34]. Proctor utilized adjoint sensitivity analysis to compute first order nuclear data calibrations between models and experiments in [35].

1.3 Novel Elements of this Dissertation

This dissertation expands on Muñoz-Cobo's theoretical developments of the stochastic description of the neutron field with a neutron detector [5]. We use his formulation of the stochastic neutron transport equation to arrive at a master moment generating equation, a full phase-space treatment of the neutron field in terms of the standard Boltzmann transport parameters. We solve the first three downwardly coupled adjoint equations, whose solution is the importance map of source neutrons to detector contributions. For example, the third moment adjoint flux describes, at every point in phase-space, the fraction of detected triples given a source neutron born at that point in phase-space. With the adjoint fluxes (the moment importance maps to source neutrons) all we need to do to calculate the moments of the neutron multiplicity distribution is to couple the adjoint fluxes to a source distribution. Because we consider spontaneous fission sources that possess an intrinsic neutron multiplicity, we use a source probability generating function defined in [5]. The resulting moment equations are inner products between the adjoint flux and average forward source, and for moments above the mean an additional inner product that is a function of the factorial moments of the spontaneous fission source.

We have developed a method for computing the sensitivities of the high-order moments of the neutron multiplicity counting distribution to the transport parameters using first-order perturbation theory. The downwardly coupled nature of the moment equations complicates the sensitivity analysis because the higher order moments are explicit functions of lower order moments. For example, the third moment equation source term is a function of the mean adjoint flux cubed, plus the product of the second and first adjoint fluxes. Additionally, the second moment is function of the fist adjoint flux squared. To resolve the coupling between the moment equations, we derived a series of closing equations that are forward transport equations whose source terms are a combination of forward fluxes and adjoint fluxes. These closing equations describe the forward flux of contributing higher order neutrons (i.e. doubles and triples that are detected). Given the strong coupling between the adjoint moment equations, some closing equations are functions of lower order closing fluxes. This first set of closing equations accounts for the multiplicities arising from induced fission.

A second set of similar closing equations, also forward transport equations, account for the sensitivity of spontaneous fission source multiplicity. These spontaneous fission closing equations are a function of the source multiplicity, the source emission rate, and the adjoint flux importances. We find that the spontaneous fission closing equations are coupled by lower order closing fluxes appearing in the source terms. In particular, as source doubles can lead to detected triples, we couple the spontaneous fission production to induced fission multiplicities in the closing source term weighted by the importance to detection.

The SA closing equations allow us to write a completely self-contained first-order sensitivity of the neutron multiplicity counting distribution to all transport parameters, which accounts for both spontaneous fission multiplicity and self-multiplication. All the equations solved to enable a complete SA are either forward or adjoint equations with special fixed source terms that can be solved in any deterministic transport code capable of forward and adjoint fixed source solutions. The initial form/data of the transport operators never changes, only the source term that is a sum product of mixed forward and adjoint fluxes. There is a wealth of presently available neutron multiplicity counting distribution ripe for a complete SA, that will enable nuclear data evaluation and uncertainty quantification of assays of SNM.

In summary, the novel elements of this dissertation are:

1. generate moment equations and sensitivity formalism to arbitrarily high order
2. explicit solution of the moments up to third order for bare and reflected Pu
3. explicit derivation of sensitivity for the first, second and third moment
4. characterization of sensitivities for experiment
5. find range of applicability for first order perturbation theory

1.4 Outline of this Dissertation

The dissertation begins with the formal development of stochastic neutron transport theory and the sensitivity analysis (SA) equations in chap-two. Starting with the kernel form of the stochastic transport equation, a nonlinear equation in terms of probability generating functions. We derive a master moment generating equation and couple it to the source probability generating function to yield the inner product form of singles, doubles, and triples. Next, we derive the SA closing equations for the first three moments.

In chap-three we describe the neutron multiplicity counting experiment against which we validate our model. We simulate a counting experiment of a plutonium sphere, enclosed in several thicknesses of moderator, measured by a neutron multiplicity counter using Los Alamos National Laboratories deterministic transport code PARTISN [36]. We first confirm our calculations of the self-multiplication with prior calculations. We determine the first three moments (singles, doubles, and triples) and show they agree well with experiment.

In chap-four we compute the relative sensitivity coefficients of the three moments with respect to the transport parameters. We consider the energy dependent parameters first, and compare how the sensitivity of parameters change with increasing moment and across thicknesses of reflector. We then energy-collapse our parameter sensitivities to study an energy independent model, effectively a one-group system, allowing us to rank the overall sensitives.

To ensure our SA is valid we compute the truncation error of our first-order approximation of perturbation theory in chap-five. The truncation error is determined by comparing the first-order approximation using perturbed nuclear data with explicit transport solutions. We simplify our model by considering the relative perturbation of lumped parameters, i.e. we perturb the total forward source term not the average multiplicity or decay rate that comprise it. We compute the truncation error for the first three moments, for the bare and the reflected Pu sphere. We find that in all cases, when perturbing all parameters from $\pm 10\%$, that at worst $\approx 85\%$ of our perturbations, for a single parameter, pass. If perturbations are limited to $\approx 2.5\%$ all pass.

We conclude our discussion of the SA of the moments of the neutron multiplicity counting distribution in chap-six. We summarize our findings and describe the potential applications of this work. Finally, we offer supporting and additional data in chap:App, such as convergence studies, plots of forward and adjoint fluxes and sources, sensitivities and nuclear data.

Chapter 2

Theory

2.1 Introduction

Neutron multiplicity counting experiments are useful in characterizing the properties of special nuclear material (SNM) by nondestructive assay. These properties include neutron source strength, multiplication, and generation time; i.e. the kinetics parameters of a fissile system [4]. Neutron counting in non-multiplying (i.e., non-fissile) systems are accurately characterized by the mean of the neutron number distribution because all higher order moments of the distribution are explicit functions of the mean. These systems exhibit Poisson statistics as all interactions are independent. Multiplying (spontaneous and induced fission) systems cannot be described by Poisson statistics [3] because the varying yield of neutrons from fission introduces a dependency between simultaneous and sequential events. This deviation from Poisson statistics is evident in the broadening of the neutron multiplicity counting distribution compared to a Poisson distribution with the same mean, as seen in Figure 2.1. Which shows the multiplicity counting distribution measured from a 4.5 kg 94% ^{239}Pu metal sphere, both bare and reflected by polyethylene.

Multiplicity counting experiments measure the frequency of detecting a given number of coincident neutrons during a gate interval [1]. The result of this measurement is the neutron multiplicity distribution which estimates the probability of detecting a given number of coincident neutrons during the gate. The broadening of the distribution is primarily due to induced fission chain-reactions and also from the intrinsic multiplicity of spontaneous fission. The deviation from Poisson statistics increases with the neutron multiplication of the system, as is seen in Figure 2.1 with the addition of polyethylene reflector to the plutonium sphere as compared to the bare sphere, which has lower multiplication. Subcritical systems exhibit fluctuations in the neutron population due to variations in the intensity, and duration of fission neutron chain reactions and this varying neutron population broadens the counting distribution by introducing additional correlated neutrons to the system.

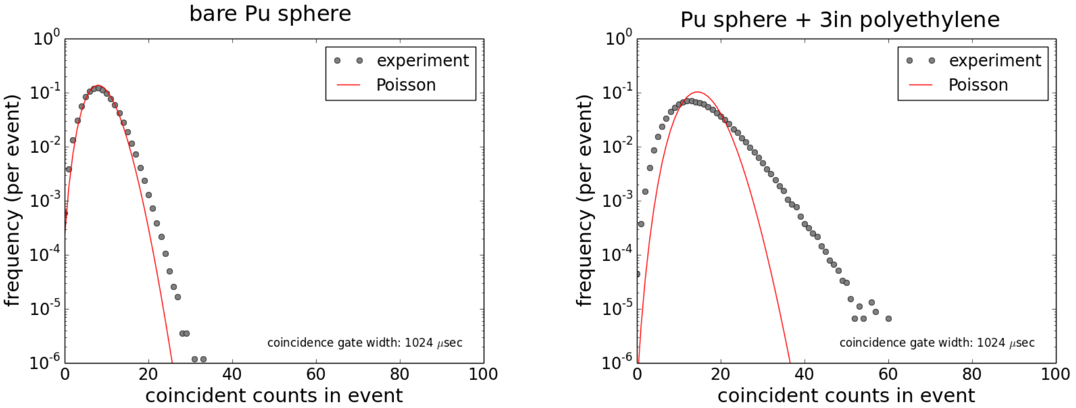

Figure 2.1: Poisson distribution compared to multiplicity distribution measured from a subcritical plutonium sphere (left), [4]. Fission chains cause a deviation from Poisson statistics, which increases with multiplication as seen by the addition of a polyethylene reflector (right).

To accurately characterize these multiplying systems it is necessary to calculate the higher order moments (variance, skewness, etc.) of the counting distribution. These moments are not explicit functions of the mean as they are for a Poisson distribution. Additionally, it is useful to know the sensitivity of these moments to the system parameters, and to propagate the nuclear parameter uncertainties onto the moments. The goal of this work is to develop a method to perform sensitivity analysis (SA) on the moments of the neutron multiplicity counting distribution in order to enable uncertainty quantification (UQ) of calculated moments. SA/UQ techniques have, so far, only been applied to the mean of neutron distributions, reaction rates, and eigenvalues, such as k_{eff} [37],[34].

The development of the SA method for the neutron multiplicity counting moments begins with the stochastic transport equation (STE), a fully probabilistic description of the neutron field. Solving the STE is computationally expensive. However, we are able to extract computationally tractable moment equations from the STE, which are standard forward/adjoint transport equations with special fixed sources [5]. From these moment equations we develop inner products to compute the moments of the multiplicity counting distribution. As the moments of the distribution are defined as inner products, the tools of perturbation theory can be brought to bear in developing the SA formalism for the moments. We develop a SA method for arbitrarily high order moments of the neutron multiplicity counting distribution that relies on standard forward/adjoint deterministic transport solutions, which enables easy implementation in most deterministic transport codes, such as PARTISN [29],[36].

We validate our model and SA methodology for the moments of the neutron counting distribution by modeling the BeRP ball (Beryllium Reflected Plutonium), a subcritical, 4.5 kg sphere of plutonium metal, containing 94% ^{239}Pu and 6% ^{240}Pu [38]. We compute moments of the neutron multiplicity counting rate distribution, as opposed to the gate/time dependent multiplicity distribution, considered in [4]. This counting rate distribution can be thought of as the asymptotic distribution for a multiplicity counting experiment with an infinitely wide gate. We compute the mean and excess variance of the distribution and show that they are in close agreement with experimental results.

We compute the sensitivity coefficients for the first two moments and rank the most influential parameters by considering the group collapsed relative sensitivity coefficients. We find that the sensitivity coefficients increase in magnitude with each moment, as expected due to the coupling between moments. Finally, we confirm our first-order perturbation theory approximation by explicit calculation of the relative truncation error. We find that the relative error is less than the relative perturbation in the parameter.

Our goal is to deterministically calculate the sensitivities of the moments of the neutron multiplicity counting distribution to neutron transport parameters, including:

- Cross-sections, σ_f (fission), σ_c (capture), σ_s (scatter), and σ_t (total).
- Nuclide densities, ρ
- Fission spectrum, χ
- Moments of fission neutron yield distribution, p_ν
- Neutron source, Q
- Detector response, σ_d

We begin by deriving the moment equations, to arbitrarily high order from the stochastic transport equation. As we will show, the moment equations are fixed source subcritical Boltzmann adjoint transport equations with source terms specific to each moment. We determine the moments of the neutron multiplicity counting distribution by taking the inner product (integrating over all phase space) of moment adjoint fluxes with the neutron source.

We exploit the adjoint/forward inner product form of the neutron multiplicity counting distribution moments to calculate the sensitivities of each moment to the system parameters by using first-order perturbation theory. For the moments higher than the mean, we construct new forward transport equations, with fixed source terms specific to each moment, to close our sensitivity analysis equations.

We derive the moment equations from the STE. While the solution of the STE would yield the complete set of discrete probabilities that form the neutron multiplicity counting distribution, it is too computationally difficult for multiplying systems as it is nonlinear, possesses a large *a priori* unbounded solution space, and has a solution that is a kernel probability generating function. As we will show, the moment equations are downwardly coupled, i.e., the q^{th} moment source is a function of all moments less than order q, which allows us to sequentially determine the moments to any order. As each moment is calculated by solving a standard adjoint transport problem with a fixed source, they are all calculable by deterministic transport codes capable of solving the fixed source form of the adjoint and forward Boltzmann neutron transport equation.

2.2 Stochastic Neutron Transport

The STE is a nonlinear integro-hyperbolic-differential equation whose solution is a probability generating function [5]. A probability generating function (PGF) is a special case of a polynomial index function, where the dummy variable z serves to order the set and the coefficients are probabilities associated with the order of z. The general form of our PGF is,

$$G(z,\vec{r},\hat{\Omega},E) = \sum_{n=0}^{\infty} p_n(\vec{r},\hat{\Omega},E) z^n \tag{2.1}$$

where p_n is the probability of n neutrons located in a unit of phase space $d\vec{X}$ about $\vec{X} = (\vec{r},\hat{\Omega},E)$, where

- $\vec{r}$ denotes position
- $\hat{\Omega}$ denotes direction
- E denotes energy

The PGF facilitates calculation of the moments of the probability distribution. The zeroth moment, the sum of all probabilities, is obtained by setting $z = 1$, and must equal one. To obtain the mean, we take the first derivative with respect to z, and set $z = 1$:

$$\begin{aligned} \bar{n} =& \frac{\partial G(z)}{\partial z}\Big|_{z=1} \\ =& \sum_{n=1} n p_n z^{n-1}\Big|_{z=1} \\ =& \sum_{n=1} n p_n, \end{aligned} \tag{2.2}$$

where the over bar denotes the expected value of n, i.e., the mean of the neutron population at $\vec{X}$. We compute the factorial moment of order q by taking the q^{th} derivative of the PGF with respect to z, and setting $z = 1$:

$$
\begin{aligned}
\overline{n(n-1)\dots(n-q+1)} =& \frac{\partial^q G(z)}{\partial z^q}\Big|_{z=1} \\
=& \sum_{n=q-1}^{\infty} n(n-1)\dots(n-q+1)p_n z^{n-q+1}\Big|_{z=1} \\
=& \sum_{n=q-1}^{\infty} n(n-1)\dots(n-q+1)p_n.
\end{aligned}
\tag{2.3}
$$

Subsequently, we define the q^{th} moment operator as

$$
M_q = \frac{\partial^q}{\partial z^q}\Big|_{z=1}. \tag{2.4}
$$

Such that

$$
\begin{aligned}
M_0 G =& 1 \\
M_1 G =& \overline{n} \\
M_q G =& \overline{n(n-1)\dots(n-q+1)}
\end{aligned}
\tag{2.5}
$$

Another useful property of the PGF is the simplicity of treating an ensemble of independent objects, which is a valid approximation for this work as we do not consider neutron-neutron interactions. The PGF for n-independent objects, such as an ensemble of neutrons, is the PGF for a single object raised to the power of n.

$$
G_n(z) = \left[G_1(z)\right]^n. \tag{2.6}
$$

We consider the steady state stochastic transport equation in terms of the kernel probability generating function $G_K(z, \vec{X}'|\vec{X})$ where $\vec{X} = (\vec{r}, \hat{\Omega}, E)$ represents the phase space. The kernel G_K describes the probability of a neutron existing at $\vec{X}'$ given the injection of a single neutron at $\vec{X}$. Now we consider the full kernel form of the stochastic transport equation,

$$\begin{aligned}\underbrace{-\hat{\Omega}\cdot\vec{\nabla}G_K}_{\text{streaming}} + \overbrace{\sigma_t G_K}^{\text{total interaction}} = \Bigg(\underbrace{\sigma_c}_{\text{capture}} + \overbrace{\int_0^\infty dE'' \int_{4\pi} d\Omega'' \sigma_s(\vec{X}'|E'', \hat{\Omega}'') G_K(z, \vec{r}', E'', \hat{\Omega}''|\vec{X})}^{\text{scattering}} \\ \underbrace{+ \sum_{j=0}^{\infty} p_j(\vec{r}', E')\sigma_f(\vec{r}', E') \left[\int_0^\infty dE'' \int_{4\pi} d\Omega'' \frac{\chi(E'')}{4\pi} G_K\right]^j \Bigg)}_{\text{fission}} + \underbrace{\frac{z}{v(E')}\delta(\vec{X}' - \vec{X})}_{\text{single neutron injected at } \vec{X}}\end{aligned} \tag{2.7}$$

where p_j is the probability of j neutrons released in a single induced fission, $v(E)$ is the neutron speed, and δ denotes the Dirac delta function. The other terms were previously defined in chap2-intro.

The delta function source term accounts for the injection of a single neutron at $\vec{X}'$ by establishing a single neutron probability of unity, $1 \times z^1$, for the kernel PGF. Likewise, the capture term is implicitly $\sigma_c z^0$, meaning a neutron is lost. The induced fission term is raised to the power of the number of neutrons emitted, which has the effect of increasing the the power of z in the PGF, to account for a growing neutron population. We assume that emergent fission neutrons are uncorrelated in energy and direction to the inducing neutron and to each other. [1] The stationary stochastic transport equation has the standard non-reentrant boundary conditions

---

[1] Ongoing theoretical and experimental studies are reevaluating this standard assumption but they have not been incorporated into deterministic transport theory and calculations yet [20].

$$G_K(z,\vec{X}'|\vec{X})\big|_{\vec{r}'=\partial V} = 1,\ \hat{n}_{\partial V}\cdot\hat{\Omega} > 0, \tag{2.8}$$

where ∂V is the surface boundary of the spatial domain V, and $\hat{n}$ is the unit normal to the boundary.

We could solve for G_K and determine the moments of the neutron multiplicity counting distribution by using the moment operator Eq. 2.4 within an inner product over all phase space. For example, the mean neutron density would be calculated as,

$$\overline{N}(\vec{X}) = \left\langle M_1 G_K(z,\vec{X}'|\vec{X}), Q(\vec{X}')\right\rangle, \tag{2.9}$$

where Q is the mean of the neutron source and the inner product is defined as,

$$\langle f,g\rangle = \int_V d^3r \int_{4\pi} d\Omega \int_0^\infty dE f(\vec{r},\hat{\Omega},E)g(\vec{r},\hat{\Omega},E). \tag{2.10}$$

However, we do not do this because solving a nonlinear equation for the probability generating function is too computationally expensive.

Instead we obtain an equation for the Green's function of the mean, $\bar{n}(\vec{X}'|\vec{X}) = M_1 G_K$, by operating on the stochastic transport equation with M_1 to yield,

$$\begin{aligned}\left(-\hat{\Omega}\cdot\vec{\nabla}+\sigma_t\right)\bar{n}(\vec{X}'|\vec{X}) = &\int_0^\infty dE'' \int_{4\pi} d\Omega'' \sigma_s(\vec{X}'|\vec{X}'',\hat{\Omega}'')\bar{n}(\vec{X}''|\vec{X}) + \\ &\bar{\nu}\sigma_f \int_0^\infty dE'' \int_{4\pi} d\Omega'' \frac{\chi(E'')}{4\pi}\bar{n}(\vec{X}''|\vec{X}) + \frac{\delta(\vec{X}'-\vec{X})}{v(E')}\end{aligned} \tag{2.11}$$

Observe that Eq. 2.11 is the standard form of the fixed source adjoint Boltzmann transport equation, which we write as

$$L^\dagger \bar{n}(\vec{X}'|\vec{X}) = \frac{\delta(\vec{X}' - \vec{X})}{v(E')} \tag{2.12}$$

where the adjoint transport operator $L^\dagger$ is defined as

$$\begin{aligned} L^\dagger = &- \hat{\Omega} \cdot \vec{\nabla} + \sigma_t - \Bigg(\int_0^\infty dE'' \int_{4\pi} d\Omega'' \sigma_s(\vec{X}'|E'', \hat{\Omega}'') \\ &+ \bar{\nu}\sigma_f \int_0^\infty dE'' \int_{4\pi} d\Omega'' \frac{\chi(E'')}{4\pi} \Bigg) \end{aligned} \tag{2.13}$$

The mean neutron Green's function $\bar{n}$ must satisfy the standard forward Boltzmann transport equation, $L\psi = Q$, where L is the forward transport operator,

$$L = \hat{\Omega} \cdot \vec{\nabla} + \sigma_t - \left(\int_0^\infty dE'' \int_{4\pi} d\Omega'' \sigma_s(E'', \hat{\Omega}''|E', \hat{\Omega}') + \frac{\chi}{4\pi} \int_0^\infty dE'' \int_{4\pi} d\Omega'' \bar{\nu}\sigma_f \right) \tag{2.14}$$

and ψ is the angular flux,

$$v(E) \langle \overline{n}, Q \rangle = \left\langle \psi, Q^\dagger \right\rangle \tag{2.15}$$

where $Q^\dagger = \frac{\delta(\vec{X}' - \vec{X})}{v(E')}$, such that

$$\begin{aligned} \psi &= v(E) \langle \overline{n}, Q \rangle \\ &= v(E)\overline{N} \end{aligned} \tag{2.16}$$

the mean neutron density is defined as $\bar{N} = \langle \bar{n}, Q \rangle$ and yields

$$Lv(E')\bar{N}(\vec{X}') = Q(\vec{X}') \tag{2.17}$$

which is an equation that is no longer in kernel form.

Using the relation of the adjoint operator to inner products,

$$\begin{aligned} \left\langle L^\dagger \psi^\dagger, \psi \right\rangle &= \left\langle \psi^\dagger, L\psi \right\rangle \\ \left\langle Q^\dagger, \psi \right\rangle &= \left\langle \psi^\dagger, Q \right\rangle, \end{aligned} \tag{2.18}$$

we recover the standard form of the mean neutron density,

$$\left\langle \bar{n}(\vec{X}'|\vec{X}), L\bar{N}(\vec{X}') \right\rangle = \left\langle L^\dagger \bar{n}(\vec{X}'|\vec{X}), \bar{N}(\vec{X}') \right\rangle. \tag{2.19}$$

Casting this expression in terms of the expected flux, $\psi(\vec{X}) = v(E)\bar{N}(\vec{X})$, we recover the forward Boltzmann transport equation, $L\psi = Q$ from the STE. We use this formalism to directly convert the kernel form of the STE Eq. 2.7 to the "master moment generating equation", [2]

$$\begin{aligned} \left(-\hat{\Omega} \cdot \vec{\nabla} + \sigma_t\right) G(z, \vec{X}) =& \sigma_c + \int_0^\infty dE' \int_{4\pi} d\Omega' \sigma_s G(z, \vec{r}, \hat{\Omega}, E|\hat{\Omega}', E') + \\ & \sum_{j=0}^\infty p_j \sigma_f \left[\int_0^\infty dE' \int_{4\pi} d\Omega' \frac{\chi}{4\pi} G(z, \vec{X}) \right]^j. \end{aligned} \tag{2.20}$$

Now we derive the first three moment equations, where the q^{th} moment adjoint flux is given by,

---

[2] This term coined by Muñoz-Cobo in [5].

$$\psi_q^\dagger = v(E) M_q G(z), \tag{2.21}$$

where we multiply the probability generating function by the neutron speed so our moments are in terms of flux-like quantities, not neutron densities. We recover the expected mean adjoint equation by operating on the "master moment generating equation", Eq. 2.20, with vM_1,

$$L^\dagger \psi_1^\dagger = Q_1^\dagger, \tag{2.22}$$

where we have a choice of adjoint source. In this work we are interested in the moments of the neutron multiplicity *counting* distribution, and therefore, we set the first moment adjoint source to the detector response function, $Q_1^\dagger = \sigma_d$, such that

$$\left\langle Q_1^\dagger, \psi \right\rangle = \langle \sigma_d, \psi \rangle \tag{2.23}$$

is the mean count rate.

In the kernel formulation of the stochastic transport equation we considered the probability distribution over all phase space given any forward source distribution. By the setting the adjoint source to the detector response function, the probability distribution accounts for detector interactions. Without neutron multiplicity all higher order moments would be given by the Poisson distribution, in which all higher order moments are a function of the mean,

$$\overline{n(n-1)(n-2)\ldots(n-q+1)}_{Poisson} = \overline{n}^q. \tag{2.24}$$

Our moment equations account for the excess to the Poisson distribution. For the q^{th}

moment the excess, H_q, is the difference between the q^{th} factorial moment of the neutron multiplicity counting distribution and the mean to the power of q,

$$H_q = \overline{n(n-1)(n-2)\dots(n-q+1)} - \overline{n}^q \tag{2.25}$$

Before we physically interpret the mean, Eq. 2.22, and the moments that follow, we derive the equations for second and third moments, $\psi_2^\dagger$ and $\psi_3^\dagger$, respectively. We obtain the second moment equation by operating on Eq. 2.20 with vM_2

$$\begin{aligned} L^\dagger \psi_2^\dagger &= \overline{\nu(\nu-1)}\sigma_f \left[\int_0^\infty dE' \int_{4\pi} d\Omega' \frac{\chi}{4\pi}\psi_1^\dagger\right]^2 \\ &= \overline{\nu(\nu-1)}\sigma_f I_1^2 = Q_2^\dagger, \end{aligned} \tag{2.26}$$

where

$$I_1 = \int_0^\infty dE' \int_{4\pi} d\Omega' \frac{\chi}{4\pi}\psi_1^\dagger \tag{2.27}$$

and in general

$$I_q = \int_0^\infty dE' \int_{4\pi} d\Omega' \frac{\chi}{4\pi}\psi_q^\dagger \tag{2.28}$$

is the importance of a fission-inducing neutron to the q^{th} moment, and

$$\overline{\nu(\nu-1)\dots(\nu-q+1)} = \sum_{j=q-1}^{\infty} j(j-1)\dots(j-q+1)p_j \tag{2.29}$$

is the factorial moment of the induced fission neutron yield distribution. Observe that the second order source term $Q_2^\dagger$ depends on the first order solution $\psi_1^\dagger$.

The third moment equation is obtained by operating on the master moment generating equation, Eq. 2.20 with vM_3

$$L^\dagger\psi_3^\dagger = \overline{\nu(\nu-1)(\nu-2)}\sigma_f I_1^3 + 3\overline{\nu(\nu-1)}\sigma_f I_1 I_2 = Q_3^\dagger. \qquad (2.30)$$

Notice that the third order source term $Q_3^\dagger$ depends on both lower order solutions, $\psi_1^\dagger$ and $\psi_2^\dagger$.

We can derive the moment equations to arbitrarily higher order by operating on the "master moment generating equation", Eq. 2.20 with $M_q v$. The higher order moment equations are of the form,

$$L^\dagger\psi_q^\dagger = Q_q^\dagger(\psi_{q-1}^\dagger, \ldots, \psi_1^\dagger). \qquad (2.31)$$

However, we limit this discussion to the third order moment, which is sufficient to illustrate the salient properties of the moment equations. We observe that the moments are downward-coupled: the q^{th} moment source is a function of all lower order moment adjoint fluxes. This coupling will require special consideration when determining the sensitivities of the moments.

2.3 Moments of the Neutron Multiplicity Counting Distribution

Now that we have derived the moment equations, we turn our attention to their utility in determining the moments of the neutron multiplicity counting distribution and to their physical interpretation. We have considered the contribution of induced fission multiplicity to the moments of the neutron multiplicity counting distribution without regard to the forward source. To fully model the neutron multiplicity counting distribution we must account for the intrinsic multiplicity of the spontaneous fission source. The spontaneous fission contribution to the moments is due to the intrinsic multiplicity of source neutrons emitted by spontaneous fission. The moment generating function G_s accounts for source multiplicity contributions to the neutron multiplicity counting distribution, and was given by Muñoz-Cobo [5],

$$G_s(z) = exp\left(\sum_{j=0}^{\infty} p_{s,j} \int_V d^3r' S_0(\vec{r}') \left(\left[\int_0^{\infty} dE' \int_{4\pi} d\Omega' \frac{\chi_s}{4\pi} G(z, \vec{X}')\right]^j - 1\right)\right), \quad (2.32)$$

where,

- $p_{s,j}$ is the probability of j neutrons emitted during a spontaneous fission
- S_0 is the source spontaneous fission rate (fissions per unit time).
- χ_s is the spontaneous fission neutron spectrum
- G is the induced fission PGF defined in Eq. 2.20

When we derive moments from Eq. 2.32 we find the complete moment, not just the excess due to fission multiplicities. We write the q^{th} factorial moment as a sum of the excess H_q and the Poisson contribution, the mean count rate R_1 raised to the power of the moment order R_1^q. To obtain the spontaneous fission contribution to the moments, we operate on Eq. 2.32 with vM_q.

The equations for the moments of the neutron multiplicity counting distribution are broken up into several identifiable contributions. The q^{th} moment is $\overline{n(n-1)\dots(n-q+1)}$ and is the sum of the Poisson contribution $\overline{n}^q$ (recall Eq. 2.24) and the excess to Poisson

H_q (recall Eq. 2.25). The excess for a moment H_q can also be a function of lower order excesses $H_{q'<q}$. When deriving each moment we obtain a contribution that first appears for that moment, denoted R_q. The excess H_q is a function of R_q and lower order $R_{q'<q}$ moment terms, which we collect as C_q to allow us to focus our SA on the contributions unique to the present moment. The general form of the complete moment of the neutron multiplicity distribution is

$$\begin{aligned}\overline{n(n-1)\dots(n-q+1)} =& H_q(\psi_q^\dagger,\dots,\psi_1^\dagger,R_q,\dots,R_1)+R_1^q \\ =& R_q(\psi_q^\dagger,\dots,\psi_1^\dagger)+C_q(R_{q-1},\dots,R_1)+R_1^q \\ =& \left\langle Q_q^\dagger,\psi\right\rangle+\left\langle Q_{s,q}^\dagger,S\right\rangle+C_q(R_{q-1},\dots,R_1)+R_1^q.\end{aligned} \tag{2.33}$$

The spontaneous fission contribution is accounted for in the mean count rate $\overline{n} = vM_1G_s$ by the average source Q, where the mean count rate is, $\overline{n}=R_1$,

$$\begin{aligned}R_1 &= \sum_{j=0}^{N} jp_{s,j}\int_V d^3r' S_0\int_0^\infty dE'\int_{4\pi} d\Omega'\frac{\chi_s}{4\pi}\psi_1^\dagger \\ &= \int_V d^3r'\int_0^\infty dE'\int_{4\pi} d\Omega'(\frac{\chi_s}{4\pi}\bar{\nu}_s S_0)\psi_1^\dagger \\ &= \left\langle \psi_1^\dagger, Q\right\rangle \\ &= \left\langle \sigma_d,\psi\right\rangle,\end{aligned} \tag{2.34}$$

where ψ is the usual forward flux obtained by solving the forward fixed source form of the Boltzmann transport equation, $L\psi = Q$. We use the adjoint relations, Eq. 2.18, to express the mean count rate R_1 in equivalent forms.

Given this application of the adjoint flux, we interpret the mean adjoint flux $\psi_1^\dagger$ as a phase-space "importance map" of source neutrons to the mean neutron count rate; this is evident in Eq. 2.34. "Adjunctons" emerge from the detector response function σ_d and are backtracked through phase-space to all points of potential neutron origin. This backtracking is evident in Eq. 2.13 in the reversal of the streaming operator, $-\hat{\Omega} \cdot \vec{\nabla}$, and the incoming and outgoing neutron kernels are reversed for the scattering and fission operators.

The same importance map interpretation holds for the induced fission contributions to the higher order moments of the neutron multiplicity counting distribution R_q, which we write in equivalent forms as,

$$\begin{aligned} R_q &= \left\langle Q_q^\dagger, \psi \right\rangle + \left\langle Q_{s,q}^\dagger, S \right\rangle \\ &= \left\langle \psi_q^\dagger, Q \right\rangle + \left\langle Q_{s,q}^\dagger, S \right\rangle \end{aligned} \tag{2.35}$$

where,

$$S = \frac{\chi_s}{4\pi} S_0. \tag{2.36}$$

The adjoint sources $Q_q^\dagger$ and $Q_{s,q}^\dagger$, which we define below, are the q^{th} order detector responses to induced and spontaneous fissions, respectively. The adjoint flux $\psi_q^\dagger$ is the phase-space importance map of source neutrons to the q^{th}-moment.

The second moment adjoint source accounts for neutron doubles that are formed by pairs of singles. Taking the second derivative of Eq. 2.32 gives the total second moment $\overline{n(n-1)}$, where the excess to Poisson $H_2 = R_2$.

$$\begin{aligned}\overline{n(n-1)} =& \left\langle \psi_2^\dagger, Q \right\rangle + \left\langle \overline{\nu_s(\nu_s-1)} I_{s,1}^2, S \right\rangle + R_1^2 \\ =& \left\langle Q_2^\dagger, \psi \right\rangle + \left\langle Q_{s,2}^\dagger, S \right\rangle + R_1^2 \\ =& R_2 + R_1^2\end{aligned} \tag{2.37}$$

where $\overline{\nu_s(\nu_s-1)}$ is the second factorial moment of source neutrons emitted and the importance of spontaneous fission neutrons is

$$I_{s,1} = \int_0^\infty dE' \int_{4\pi} d\Omega' \frac{\chi_s}{4\pi} \psi_1^\dagger, \tag{2.38}$$

where $\psi_1^\dagger$ is the same adjoint flux used in Eq. 2.22. Observe that we have weighted the adjoint flux with the source fission spectrum, χ_s. The adjoint source terms for induced and source fission multiplicity have the same form,

$$\begin{aligned}R_2 =& \left\langle \overline{\nu(\nu-1)} \sigma_f I_1^2, \psi \right\rangle + \left\langle \overline{\nu_s(\nu_s-1)} I_{s,1}^2, S \right\rangle \\ =& \left\langle \overline{\nu(\nu-1)} I_1^2, \sigma_f \psi \right\rangle + \left\langle \overline{\nu_s(\nu_s-1)} I_{s,1}^2, S \right\rangle\end{aligned} \tag{2.39}$$

where the first term on the right-hand side is the mean rate of fission reactions and the second term is the mean rate of rate of spontaneous fissions, where each term is weighted by the importance of pairs of singles.

We obtain the third moment by taking the third derivative of Eq. 2.32.

$$\begin{aligned}\overline{n(n-1)(n-2)} &= \left\langle \psi_3^\dagger, Q \right\rangle + \left\langle \overline{\nu_s(\nu_s-1)(\nu_s-2)} I_{s,1}^3 + 3\overline{\nu_s(\nu_s-1)} I_{s,1} I_{s,2}, S \right\rangle + 3R_1R_2 + R_1^3 \\ &= \left\langle Q_3^\dagger, \psi \right\rangle + \left\langle Q_{s,3}^\dagger, S \right\rangle + 3R_1R_2 + R_1^3.\end{aligned} \tag{2.40}$$

Where the excess to the Poisson is

$$\begin{aligned}H_3 =& \overline{n(n-1)(n-2)} - R_1^3 \\ =& \left\langle Q_3^\dagger, \psi \right\rangle + \left\langle Q_{s,3}^\dagger, S \right\rangle + 3R_1R_2 \\ =& R_3(\psi_2^\dagger, \psi_1^\dagger) + C_3(R_2, R_1).\end{aligned} \tag{2.41}$$

Where we write the third moment excess, for the purpose of SA, in terms of contributions from R_3,

$$R_3 = \left\langle \psi_3^\dagger, Q \right\rangle + \left\langle \overline{\nu_s(\nu_s-1)(\nu_s-2)} I_{s,1}^3 + 3\overline{\nu_s(\nu_s-1)} I_{s,1} I_{s,2}, S \right\rangle \tag{2.42}$$

and lower order excesses $C_3(R_2, R_1)$.

The third moment adjoint source details how triples are constructed by three singles, and combinations of singles and doubles. The source construction from lower order moments is apparent graphically in Figure 2.2. The importance of neutron singles is denoted by I_1 and can be thought of as an average fission chain. Doubles can be formed from pairs of singles I_1^2 and is represented as two coincident singles graphically. Likewise, triples can be formed from a triad of singles I_1^3 and from coincident singles and doubles

$I_1 I_2$.

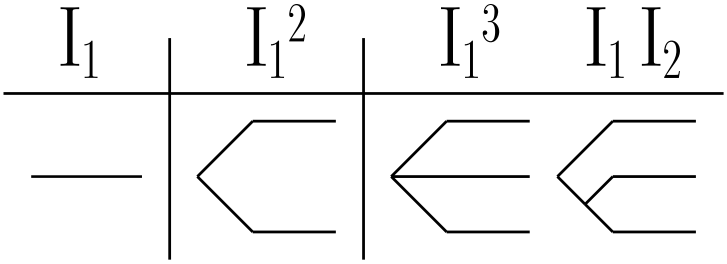

Figure 2.2: Fission chains for singles Eq. 2.22, doubles Eq. 2.26, and triples Eq. 2.30, respectively.

To calculate any moment of the neutron multiplicity counting distribution requires only one fixed source adjoint solution of the Boltzmann transport equation, where the adjoint operator $L^\dagger$ remains the same and only the source $Q_q^\dagger$ changes.

$$\begin{array}{ccc} L^\dagger \psi_1^\dagger = Q_1^\dagger & & R_1 = \left\langle \psi_1^\dagger, Q \right\rangle \\ L^\dagger \psi_2^\dagger = Q_2^\dagger & \rightarrow & R_2 = \left\langle \psi_2^\dagger, Q \right\rangle + \left\langle Q_{s,2}^\dagger, S \right\rangle \\ L^\dagger \psi_3^\dagger = Q_3^\dagger & & R_3 = \left\langle \psi_3^\dagger, Q \right\rangle + \left\langle Q_{s,3}^\dagger, S \right\rangle \\ \vdots & & \vdots \end{array}$$

2.4 Sensitivity of Multiplicity Counting Moments

Now that we have calculated the moments of the neutron multiplicity counting distribution due to both source and induced fission neutron yields, we determine the sensitivities of the moments to variations in neutron transport parameters. Our counting experiment is defined by a collection of parameters, $\alpha = (\alpha_1, \ldots, \alpha_N)$, such as cross-sections, nuclide densities, fission neutron spectra, and moments of the fission neutron yield distribution p_ν: $\overline{\nu}$, $\overline{\nu(\nu-1)}$, and $\overline{\nu(\nu-1)(\nu-2)}$. We write each moment as a function of the parameters, $R_q(\alpha)$, and we determine how R_q responds to perturbations in our parameters. If the change in the parameters $\delta\alpha$ are sufficiently small, we may approximate the perturbed response as first order Taylor series.

$$R_q(\alpha_0+\delta\alpha) \approx R_q(\alpha_0) + \sum_m \frac{\partial R_q}{\partial \alpha_m}\Big|_{\alpha=\alpha_0} \delta\alpha_m \tag{2.43}$$

Our task is to determine the derivatives of the moments with respect to each parameter, $\partial R_q/\partial\alpha$.

2.4.1 Sensitivity of the Mean

First, we review the established sensitivity of the mean response by considering the derivative with respect to the parameters.

$$\frac{\partial R_1}{\partial \alpha} = \left\langle \frac{\partial \sigma_d}{\partial \alpha}, \psi \right\rangle + \left\langle \sigma_d, \frac{\partial \psi}{\partial \alpha} \right\rangle \tag{2.44}$$

The first term on the right, the derivative of the detector response function, $\partial\sigma_d/\partial\alpha$, is calculable but the derivative of the forward flux, $\partial\psi/\partial\alpha$, is computationally intractable; it would require additional transport solutions to calculate each derivative, and the dimension of α is large, possessing thousands of elements, depending on the number of neutron energy groups. This computational roadblock is circumvented by utilizing the adjoint flux enabling us to eliminate derivatives of the forward flux. By using the adjoint inner product relation, Eq. 2.18, and the first derivative of the forward transport equation,

$$\frac{\partial L}{\partial \alpha}\psi + L\frac{\partial \psi}{\partial \alpha} = \frac{\partial Q}{\partial \alpha} \tag{2.45}$$

we write the sensitivity of the mean as

$$\begin{aligned}
\frac{\partial R_1}{\partial \alpha} &= \left\langle \frac{\partial \sigma_d}{\partial \alpha}, \psi \right\rangle + \left\langle \sigma_d, \frac{\partial \psi}{\partial \alpha} \right\rangle \\
&= \left\langle \frac{\partial \sigma_d}{\partial \alpha}, \psi \right\rangle + \left\langle L^\dagger \psi_1^\dagger, \frac{\partial \psi}{\partial \alpha} \right\rangle \\
&= \left\langle \frac{\partial \sigma_d}{\partial \alpha}, \psi \right\rangle + \left\langle \psi_1^\dagger, L\frac{\partial \psi}{\partial \alpha} \right\rangle \\
&= \left\langle \frac{\partial \sigma_d}{\partial \alpha}, \psi \right\rangle + \left\langle \psi_1^\dagger, \frac{\partial Q}{\partial \alpha} - \frac{\partial L}{\partial \alpha}\psi \right\rangle
\end{aligned} \tag{2.46}$$

where the forward derivatives are now calculable in terms of the source and the transport operator, which requires no additional transport solves. We utilized the adjoint to weight the forward source perturbations to variations of the mean response.

2.4.2 Sensitivity of the Second Moment

Now we derive the sensitivity of the second moment excess. First, consider the general case of the the higher order moments, R_q for $q > 1$.

$$\frac{\partial R_q}{\partial \alpha} = \left\langle \frac{\partial Q_q^\dagger}{\partial \alpha}, \psi \right\rangle + \left\langle \psi_q^\dagger, \frac{\partial Q}{\partial \alpha} - \frac{\partial L}{\partial \alpha}\psi \right\rangle + \frac{\partial}{\partial \alpha}\left\langle Q_{s,q}^\dagger, S \right\rangle . \tag{2.47}$$

Recall that the higher order adjoint source terms are a function of all lower order adjoint fluxes, $Q_q^\dagger(\alpha, \psi_{q-1}^\dagger, \ldots, \psi_1^\dagger)$, and therefore contains derivatives of adjoint fluxes,

$$\begin{aligned}\frac{\partial R_q}{\partial \alpha} = & \left\langle \frac{\partial Q_q^\dagger}{\partial \alpha}, \psi \right\rangle + \left\langle \psi_q^\dagger, \frac{\partial Q}{\partial \alpha} \right\rangle - \left\langle \psi_q^\dagger, \frac{\partial L}{\partial \alpha}\psi \right\rangle \\ & + \left\langle \frac{\partial Q_{s,q}^\dagger}{\partial \alpha}, S \right\rangle + \left\langle Q_{s,q}^\dagger, \frac{\partial S}{\partial \alpha} \right\rangle \end{aligned} \tag{2.48}$$

The terms that contain flux derivatives cannot be efficiently calculated,

$$\frac{\partial Q_q^\dagger(\alpha, \psi_{q^\dagger}^\dagger(\alpha))}{\partial \alpha} = \frac{\partial Q_q^\dagger}{\partial \beta} + \frac{\partial Q_q^\dagger}{\partial \psi_{q'}^\dagger}\frac{\partial \psi_{q'}^\dagger}{\partial \alpha} \text{ for } q' < q \tag{2.49}$$

$$\frac{\partial Q_{s,q}^\dagger(\alpha, \psi_{q'}^\dagger(\alpha))}{\partial \alpha} = \frac{\partial Q_{s,q}^\dagger}{\partial \beta} + \frac{\partial Q_{s,q}^\dagger}{\partial \psi_{q'}^\dagger}\frac{\partial \psi_{q'}^\dagger}{\partial \alpha} \text{ for } q' < q \tag{2.50}$$

where $\beta = (\sigma_f, \chi, \chi_s, \overline{\nu}, \overline{\nu_s}, \overline{\nu(\nu-1)}, \overline{\nu_s(\nu_s-1)}\ldots)$ is a subset of α that accounts for the parameters that explicitly appear in the adjoint moment sources.

In the case of the mean, we utilized the adjoint to account for forward flux derivatives via the adjoint definition, Eq. 2.18. We use the adjoint definition again for the higher order moments by constructing new forward problems that preserve the value of the inner products by accounting for the forward contributions of q-tuple neutrons to the response.

Consider the derivative of the second moment adjoint source term, $Q_2^\dagger$, with respect to the mean adjoint flux.

$$\begin{aligned}\left\langle \frac{\partial Q_2^\dagger}{\partial \psi_1^\dagger}\frac{\partial \psi_1^\dagger}{\partial \alpha}, \psi \right\rangle =& 2\left\langle \overline{\nu(\nu-1)}\sigma_f I_1 \int_0^\infty dE' \int_{4\pi} d\Omega' \frac{\chi}{4\pi}\frac{\partial \psi_1^\dagger}{\partial \alpha}, \psi \right\rangle \\ =& 2\left\langle F_1^\dagger \frac{\partial \psi_1^\dagger}{\partial \alpha}, \psi \right\rangle \\ =& 2\left\langle \frac{\partial \psi_1^\dagger}{\partial \alpha}, F_1\psi \right\rangle \\ =& 2\left\langle \frac{\partial \psi_1^\dagger}{\partial \alpha}, L\Phi_1 \right\rangle \\ =& 2\left\langle L^\dagger \frac{\partial \psi_1^\dagger}{\partial \alpha}, \Phi_1 \right\rangle \end{aligned} \tag{2.51}$$

We form a new adjoint operator, $F_1^\dagger$, and by the adjoint relation, Eq. 2.18, form a corresponding forward operator, F_1, that will preserve the value of the inner product. The forward operator is used create a new forward problem to close our SA system,

$$L\Phi_1 = F_1\psi. \tag{2.52}$$

The operators are defined as,

$$F_1^\dagger = \overline{\nu(\nu-1)}\sigma_f I_1 \int_0^\infty dE' \int_{4\pi} d\Omega' \frac{\chi}{4\pi} \tag{2.53}$$

$$F_1 = I_1 \frac{\chi}{4\pi} \int_0^\infty dE' \int_{4\pi} d\Omega' \overline{\nu(\nu-1)}\sigma_f \tag{2.54}$$

The adjoint relation is used to remove the adjoint flux derivative by using the new forward source term, $F_1\psi$, to construct a new forward problem to close our system of equations,

$$\begin{aligned} L\Phi_1 =& F_1\psi \\ =& I_1 \frac{\chi}{4\pi}\int_0^\infty dE' \int_{4\pi} d\Omega' \overline{\nu(\nu-1)}\sigma_f\psi \\ =& I_1 Q_{f,1} \end{aligned} \tag{2.55}$$

The new forward flux Φ_1 is the flux of neutrons that contribute to the second moment response. This is apparent in the source term, $I_1 Q_{f,1}$, where the production of neutron doubles, $Q_{f,1}$, is weighted by the importance of induced fission neutrons I_1.

Now we consider sensitivities to the spontaneous fission source intrinsic multiplicity

$$\begin{aligned} \frac{\partial Q^\dagger_{s,2}}{\partial \psi^\dagger_1}\frac{\partial \psi^\dagger_1}{\partial \alpha} =& 2\left\langle \overline{\nu_s(\nu_s-1)} I_{s,1}\int_0^\infty dE' \int_{4\pi} d\Omega' \frac{\chi_s}{4\pi}\frac{\partial \psi^\dagger_1}{\partial \alpha}, S \right\rangle \\ =& 2\left\langle F^\dagger_{s,1}\frac{\partial \psi^\dagger_1}{\partial \alpha}, S \right\rangle . \end{aligned} \tag{2.56}$$

We use the new adjoint operator to construct a new forward problem to close the system,

$$L\Phi_{s,1} = F_{s,1} S \tag{2.57}$$

where the spontaneous fission source operators are defined as,

$$F^\dagger_{s,1} = \overline{\nu_s(\nu_s-1)} I_{s,1}\int_0^\infty dE' \int_{4\pi} d\Omega' \tag{2.58}$$

$$F_{s,1} = I_{s,1}\int_0^\infty dE' \int_{4\pi} d\Omega' \overline{\nu_s(\nu_s-1)} \tag{2.59}$$

and yields the sensitivity to the multiplicity of the spontaneous fission source,

$$\frac{\partial Q^{\dagger}_{s,2}}{\partial \psi^{\dagger}_1}\frac{\partial \psi^{\dagger}_1}{\partial \alpha} = 2\left\langle \frac{\partial \sigma_d}{\partial \alpha} - \frac{\partial L^{\dagger}}{\partial \alpha}\psi^{\dagger}_1, \Phi_{s,1} \right\rangle \tag{2.60}$$

We use these new equations, and the first derivative of the mean adjoint equation to close our sensitivity system for the second moment excess, and arrive at a fully calculable expression,

$$\begin{aligned}\frac{\partial R_2}{\partial \alpha} &= \left\langle \psi^{\dagger}_2, \frac{\partial Q}{\partial \alpha} - \frac{\partial L}{\partial \alpha}\psi \right\rangle + \left\langle \frac{\partial Q^{\dagger}_2}{\partial \beta}, \psi \right\rangle + 2\left\langle \frac{\partial \sigma_d}{\partial \alpha} - \frac{\partial L^{\dagger}}{\partial \alpha}\psi^{\dagger}_1, \Phi_1 \right\rangle \\ &+ \left\langle Q^{\dagger}_{s,2}, \frac{\partial S}{\partial \alpha} \right\rangle + \left\langle \frac{\partial Q^{\dagger}_{s,2}}{\partial \beta}, S \right\rangle + 2\left\langle \frac{\partial \sigma_d}{\partial \alpha} - \frac{\partial L^{\dagger}}{\partial \alpha}\psi^{\dagger}_1, \Phi_{s,1} \right\rangle\end{aligned} \tag{2.61}$$

Using the above we write the full sensitivity to the second moment, including the Poisson contribution, for completeness as,

$$\frac{\partial \overline{n(n-1)}}{\partial \alpha} = \frac{\partial R_2}{\partial \alpha} + 2R_1\frac{\partial R_1}{\partial \alpha} \tag{2.62}$$

2.4.3 Sensitivity of the Third Moment

The third moment source sensitivity equation includes derivatives of the first and second moment adjoint fluxes, as theses moments appear in the source term Eq. 2.30. Considering the derivative with respect to the mean adjoint flux gives,

$$\begin{aligned}\left\langle \frac{\partial Q_3^\dagger}{\partial \psi_1^\dagger}\frac{\partial \psi_1^\dagger}{\partial \alpha}\right\rangle =&3\Big\langle\overline{\nu(\nu-1)(\nu-2)}\sigma_f I_1^2\int_0^\infty dE'\int_{4\pi} d\Omega' \frac{\chi}{4\pi}\frac{\partial \psi_1^\dagger}{\partial \alpha}+ \\ &\overline{\nu(\nu-1)}\sigma_f I_2\int_0^\infty dE'\int_{4\pi} d\Omega'\frac{\chi}{4\pi}\frac{\partial \psi_1^\dagger}{\partial \alpha},\psi\Big\rangle \\ =&3\left\langle F_2^\dagger\frac{\partial \psi_1^\dagger}{\partial \alpha},\psi\right\rangle .\end{aligned} \tag{2.63}$$

The derivative with respect to the second moment adjoint flux is expressible in terms of the first fission adjoint operator $F_1^\dagger$ Eq. 2.53,

$$\begin{aligned}\left\langle \frac{\partial Q_3^\dagger}{\partial \psi_2^\dagger}\frac{\partial \psi_2^\dagger}{\partial \alpha}\right\rangle =&3\left\langle\overline{\nu(\nu-1)}\sigma_f I_1\int_0^\infty dE'\int_{4\pi} d\Omega'\frac{\chi}{4\pi}\frac{\partial \psi_2^\dagger}{\partial \alpha},\psi\right\rangle \\ =&3\left\langle F_1^\dagger\frac{\partial \psi_2^\dagger}{\partial \alpha},\psi\right\rangle\end{aligned} \tag{2.64}$$

These derivatives are resolved, as in the second moment by constructing new forward equations.

First, we address the mean adjoint derivative Eq. (2.63), we derive an equation that accounts for the contribution of singles to forming triples,

$$L\Phi_2 = F_2\psi \tag{2.65}$$

where we define the second induced fission operators as,

$$F_2^\dagger = \overline{\nu(\nu-1)(\nu-2)}\sigma_f I_1^2 \int_0^\infty dE' \int_{4\pi} d\Omega' \frac{\chi}{4\pi} + \overline{\nu(\nu-1)}\sigma_f I_2 \int_0^\infty dE' \int_{4\pi} d\Omega' \frac{\chi}{4\pi} \tag{2.66}$$

$$F_2 = \frac{\chi}{4\pi}\left(I_1^2 \int_0^\infty dE' \int_{4\pi} d\Omega' \overline{\nu(\nu-1)(\nu-2)}\sigma_f + I_2 \int_0^\infty dE' \int_{4\pi} d\Omega' \overline{\nu(\nu-1)}\sigma_f \right) \tag{2.67}$$

Addressing the second adjoint flux derivatives in Eq. 2.64 we encounter our first closing equation Eq. 2.55, and after utilizing the adjoint inner product relation and derivative of the second moment adjoint equation, we form another forward closing equation.

$$\begin{aligned}\left\langle \frac{\partial Q_3^\dagger}{\partial \psi_2^\dagger}\frac{\partial \psi_2^\dagger}{\partial \alpha}, \psi \right\rangle &= 3\left\langle F_1^\dagger \frac{\partial \psi_2^\dagger}{\partial \alpha}, \psi \right\rangle \\ &= 3\left\langle \frac{\partial Q_2^\dagger}{\partial \alpha} - \frac{\partial L^\dagger}{\partial \alpha}\psi_2^\dagger, \Phi_1 \right\rangle \end{aligned} \tag{2.68}$$

We have closed one step of the third moment sensitivity but the second adjoint source term still includes derivatives of the mean adjoint flux.

$$\left\langle \frac{\partial Q_2^\dagger}{\partial \psi_1^\dagger}\frac{\partial \psi_1^\dagger}{\partial \alpha}, \Phi_1 \right\rangle = \left\langle F_1^\dagger \frac{\partial \psi_1^\dagger}{\partial \alpha}, \Phi_1 \right\rangle \tag{2.69}$$

To fully close this system we use the same technique to yield another forward closing equation,

$$L\Phi_3 = F_1\Phi_1 \tag{2.70}$$

that accounts for the contribution of neutron triples initiated by contributing doubles.

We arrive at similar expressions for the third moment spontaneous fission source sensitivity, where the closing equations are

$$L\Phi_{s,2} = F_{s,2}S \tag{2.71}$$

$$L\Phi_{s,3} = F_1\Phi_{s,1} \tag{2.72}$$

where in the last case, $F_1\Phi_{s,1}$, we use the induced fission operator F_1, as it accounts for sensitivities of the mean adjoint flux in the induced second moment adjoint source, $Q_2^\dagger$. Where spontaneous fission operators are defined as,

$$F_{s,2}^\dagger = \overline{\nu_s(\nu_s-1)(\nu_s-2)}I_{s,1}^2\int_0^\infty dE'\int_{4\pi}d\Omega' + \overline{\nu_s(\nu_s-1)}I_{s,2}\int_0^\infty dE'\int_{4\pi}d\Omega' \tag{2.73}$$

$$F_{s,2} = I_{s,1}^2\int_0^\infty dE'\int_{4\pi}d\Omega'\overline{\nu_s(\nu_s-1)(\nu_s-2)} + I_{s,2}\int_0^\infty dE'\int_{4\pi}d\Omega'\overline{\nu_s(\nu_s-1)} \tag{2.74}$$

Combining all expressions gives the sensitivity of the third moment excess to the Poisson statistics and lower order moment contributions,

$$\begin{aligned}\frac{\partial R_3}{\partial\alpha} =& \left\langle \frac{\partial Q_3^\dagger}{\partial\beta}, \psi\right\rangle + \left\langle \psi_3^\dagger, \frac{\partial Q}{\partial\alpha} - \frac{\partial L}{\partial\alpha}\psi\right\rangle + 3\left\langle \frac{\partial Q_2^\dagger}{\partial\beta} - \frac{\partial L^\dagger}{\partial\alpha}\psi_2^\dagger, \Phi_1\right\rangle \\ &+ 3\left\langle \frac{\partial\sigma_d}{\partial\alpha} - \frac{\partial L^\dagger}{\partial\alpha}\psi_1^\dagger, \Phi_2 + 2\Phi_3\right\rangle \\ &+ \left\langle \frac{\partial Q_{s,3}^\dagger}{\partial\beta}, S\right\rangle + \left\langle Q_{s,3}^\dagger, \frac{\partial S}{\partial\alpha}\right\rangle + 3\left\langle \frac{\partial Q_2^\dagger}{\partial\beta} - \frac{\partial L^\dagger}{\partial\alpha}\psi_2^\dagger, \Phi_{s,1}\right\rangle \\ &+ 3\left\langle \frac{\partial\sigma_d}{\partial\alpha} - \frac{\partial L^\dagger}{\partial\alpha}\psi_1^\dagger, \Phi_{s,2} + 2\Phi_{s,3}\right\rangle.\end{aligned} \tag{2.75}$$

The complete sensitivity of the third moment is the sum of the sensitivities of the third moment adjoint source, the product of lower order moments, and the Poisson distribution,

$$\begin{aligned}\frac{\partial\overline{n(n-1)(n-2)}}{\partial\alpha} =& \frac{\partial H_3}{\partial\alpha} + \frac{\partial R_1^3}{\partial\alpha} \\ =& \frac{\partial R_3}{\partial\alpha} + \frac{\partial C_3}{\partial\alpha} + \frac{\partial R_1^3}{\partial\alpha} \\ =& \frac{\partial R_3}{\partial\alpha} + 3R_1\frac{\partial R_2}{\partial\alpha} + 3R_2\frac{\partial R_1}{\partial\alpha} + 3R_1^2\frac{\partial R_1}{\partial\alpha}.\end{aligned} \tag{2.76}$$

Our scheme of producing additional importance weighted forward problems continues to any order, given the downward-only coupling of the adjoint moment equations of the neutron multiplicity counting distribution.

2.5 Conclusion

We developed the equations to describe the supra-Poisson contributions of the neutron multiplicity counting distribution for configurations of multiplying systems and neutron detectors. The moment excess equations were derived from the stochastic transport equation, a complete phase-space description of the probability distribution of the neutron field. The STE is too expensive to solve numerically. So instead, we take moments of the STE to yield computationally tractable fixed source adjoint equations. These moment equations are downwardly coupled via the source term to lower order moment adjoint fluxes, which allows us to sequentially solve to a given moment using forward/adjoint deterministic transport codes capable of fixed source solutions.

We find the moment counting rates of the neutron multiplicity counting distribution by forming inner products between the adjoint moment equations, the forward flux, and the moments of the multiplicity of a spontaneous fission source. Because our formulation of the moments is in terms of inner products we can apply first-order perturbation theory to find the sensitivity of the moments to the transport parameters. After reviewing the established mean SA we find that new forward equations, with fixed source terms that are a blend of forward and adjoint fluxes, close our SA system of equations for the higher order moments.

Chapter 3

Moment Calculations

3.1 Introduction

We begin by describing the neutron multiplicity counting experiment that we simulate, using the deterministic code PARTISN, to test our SA. Experimental neutron multiplicity counting data is available for the BeRP ball, a 4.5 kg sphere of α-phase plutonium metal. We simulate experiments of the bare BeRP ball and the BeRP ball reflected by high-density polyethylene. We verify our material and geometric assumptions by comparing our calculations of k_{eff} with previous calculations. The nPod, an array of polyethylene-moderated ^{3}He-tubes, was our neutron multiplicity counter. An MCNP model allows us to treat the detector as an efficiency on the external boundary of BeRP ball.

Next, we find good agreement between our calculation and the mean of the multiplicity counting distribution with the experimental results for the bare BeRP ball and for several thickness of reflector. The softening of the neutron spectrum increases with the addition of reflector and has significant impact on the moments of the neutron multiplicity counting distribution. The reflector increases the neutron multiplication but also slows neutrons to energies to which the detector is insensitive. We show how the leakage, adjoint flux, and forward flux are affected by the addition of reflector. In particular, we show how the addition of reflector alters the adjoint flux, the importance of source neutrons to the mean, by considering the ratio of reflected to bare adjoint fluxes over the space of the plutonium region.

Similarly, for the second and third moments, we compare our calculation of the moment excess to experiment, for several thicknesses of reflector, and find adequate agreement. We introduce metrics of relative excess to Poisson statistics, that are ratios of the higher moment excesses with respect to powers of the mean. These relative excess metrics exhibit asymptotic behavior with regard to gate width and increase in magnitude with neutron multiplication; our model captures both of these behaviors. Finally, we investigate the impact of reflectors between two cases by examining the ratios of adjoint fluxes in the neutron multiplying region.

3.2 The BeRP Ball and Polyethylene Reflectors

To validate our model, we simulate the neutron multiplicity counting experiment of a 4.5 kg sphere of α-phase plutonium metal with a radius of 3.794 cm, a density of $19.86 g/cm^3$ and an isotopic composition of 94% ^{239}Pu, the multiplying medium, and 6% ^{240}Pu, the spontaneous fission source [2]. In our model, we disregard other nuclides and do not model the thin (0.3 mm) steel cladding outside the plutonium sphere. This particular plutonium sphere is called the BeRP (beryllium-reflected plutonium) ball; it was originally used for criticality safety experiments at Los Alamos National Laboratory (LANL) the beryllium reflectors are not utilized in our study [39]. In addition to the bare BeRP ball, we consider the effects of enclosing the sphere in several thicknesses, up to 6 inches, of polyethylene reflector/moderator with an average density, over shell thicknesses, of 0.96 g/cm^3. A comprehensive description of the BeRP ball and shells can be found in the Sandia National Laboratory report [38]. The BeRP ball nested in the center of several layers of reflector is shown in Figure 3.1.

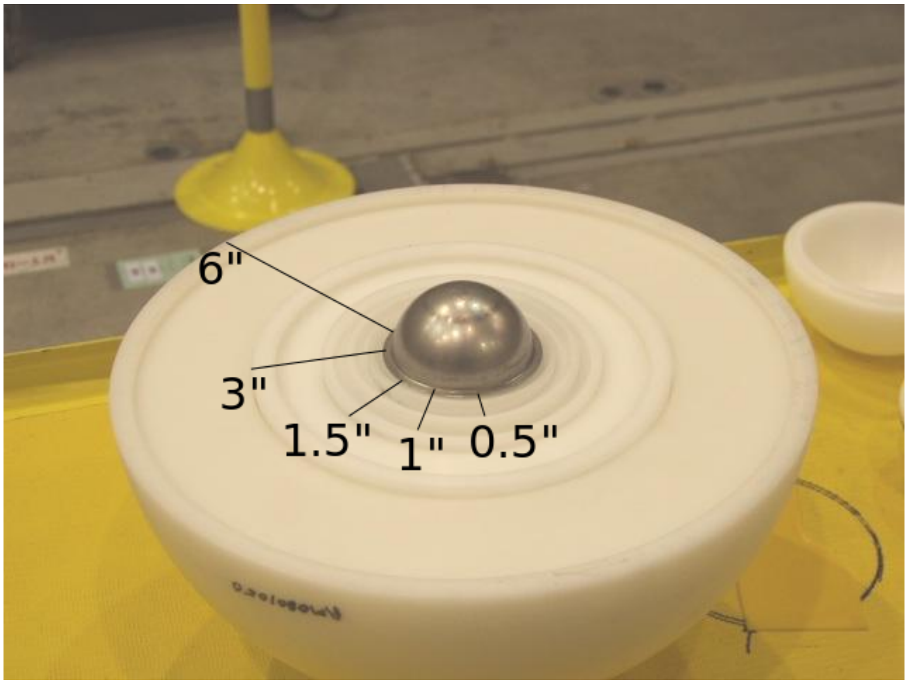

Figure 3.1: The BeRP ball, a plutonium metal sphere, enclosed by the lower hemispheres of polyethylene reflectors [39].

We model the BeRP ball using LANL's deterministic transport code PARTISN for all of our forward, adjoint, and eigenvalue computations [36]. Given the spherical symmetry of the BeRP ball, we use one-dimensional spherical geometry in our PARTISN models. The 44-group ENDF-VII cross-section library is used because it contains the covariance data required for future UQ. To effectively model the forward peaked scattering in plutonium metal, third-order scattering P_3 is used combined with S_{32} angular quadrature to resolve the higher order scattering terms in the discrete ordinates model. Before turning to simulations of the BeRP ball and polyethylene reflectors, we consider the nuclear data, such as cross-sections, of the two distinct regions under study.

The BeRP ball is chiefly characterized by the ratio of two isotopes of plutonium: ^{239}Pu and ^{240}Pu. We describe the number density of nuclides in per barn×cm in Table 3.1.

Table 3.1: Number density of plutonium isotopes in the BeRP ball per $barn \times cm$.

nuclide	density $[1/barn \times cm]$
^{239}Pu	0.046421
^{240}Pu	0.002951

The ^{239}Pu serves as the principle multiplying medium. While induced fission is possible in ^{240}Pu, the contribution of fission neutron production is negligible, as seen in the comparison between the macroscopic fission cross-section multiplied by the average number of induced fission neutrons, $\overline{\nu}\sigma_f$, in Figure 3.2. It is important to note that the fission neutron production cross-section is orders of magnitude greater in the slow regions, this will become important when reflectors are added to slow the fast sources of neutrons from induced and spontaneous fission.

Due to the disparity between the fission cross-sections between plutonium isotopes, we ignore the contribution of induced fissions from ^{240}Pu when constructing the adjoint source terms. The adjoint sources depend on the factorial moments of the fission neutron multiplicity distribution. The fission cross-section is maximum at low energies and the moments of the neutron multiplicity are greater for fast fissions, as seen in Figure 3.3. While we ignore the induced fission terms due to ^{240}Pu in the adjoint sources, they are implicitly included in forward and adjoint PARTISN calculations in the transport

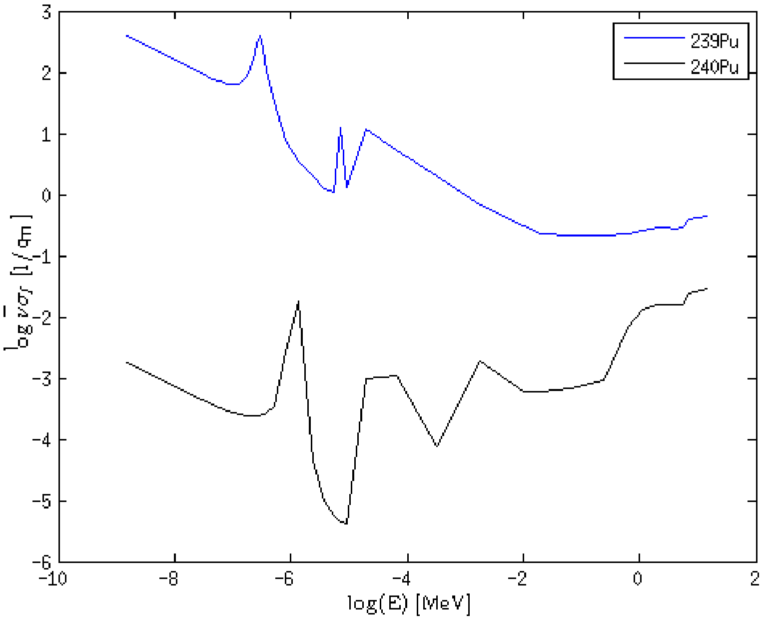

Figure 3.2: Macroscopic fission neutron production cross-section $\overline{\nu}\sigma_f$ for ^{239}Pu and ^{240}Pu.

operator by existing in the cross-section library.

We determine the higher order moments of the induced fission neutron multiplicity distribution by using the distribution $p_\nu(E)$ found in [16]. The moments of p_ν increase with inducing neutron energy and moment are shown in Figure 3.3.

The ^{240}Pu spontaneous fission source has an intrinsic neutron multiplicity that must be accounted for to accurately determine the higher order moments. The first three moments, considered in this work, are provided in Table 3.2.

Table 3.2: Neutron multiplicity of ^{240}Pu spontaneous fission source [16].

$\overline{\nu_s}$	2.154
$\overline{\nu_s(\nu_s-1)}$	3.788939
$\overline{\nu_s(\nu_s-1)(\nu_s-2)}$	5.210497

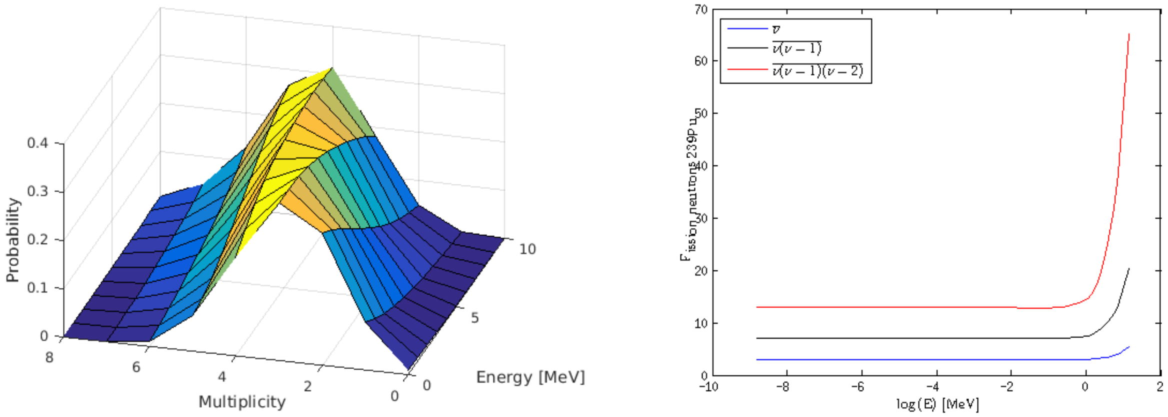

Figure 3.3: Distribution (left) and moments (right) of the induced fission neutron multiplicity for ^{239}Pu [16].

In addition to the bare BeRP ball, we consider it enclosed in polyethylene reflector. The reflector serves to slow and reflect neutrons back into the plutonium where they have a greater probability of inducing fission. The reflectors range from 0.5 inch to 6.0 inch in thickness. The shells are constructed in a nesting doll fashion, as seen in Figure 3.1. Each nested layer has its own nominal density, [38], but we average over them to define a single density for all thicknesses of polyethylene in Table 3.3.

Table 3.3: Number density of hydrogen and carbon in polyethylene shells per $barn \times cm$.

nuclide	density $[1/b \times cm]$
^{1}H	0.080988
^{12}C	0.040402

3.2.1 K-effective and Neutron Multiplication

Before determining the moments of the neutron multiplicity counting distribution, we first confirm our geometry and model assumptions. We ensure that our models are accurate by computing k_{eff} and the corresponding neutron multiplication M, a measure of the average total fission neutrons per induced fission, given in terms of k_{eff} as,

$$\begin{aligned} M &= 1 + k_{eff} + k_{eff}^2 + \dots \\ &= \sum_{n=0}^{\infty} k_{eff}^n \\ &= \frac{1}{1-k_{eff}} \end{aligned} \tag{3.1}$$

Our deterministically computed quantities for k_{eff} and multiplication are comparable to MCNP estimates shown in Table 3.4. There is generally good agreement between our calculations and those found in [39], for all thicknesses of polyethylene.

Table 3.4: Comparison of k_{eff} eigenvalue and neutron multiplication over several thicknesses of polyethylene reflectors between MCNP-PoliMi, [39], and PARTISN calculations.

Reflector	keff MCNP	keff PARTISN	Mult. MCNP	Mult. PARTISN
None	0.7768	0.7667	4.4803	4.2858
0.5”	0.8298	0.8196	5.8754	5.5425
1.0”	0.8715	0.8625	7.7797	7.2744
1.5”	0.9049	0.8948	10.5152	9.5088
3.0”	0.9390	0.9312	16.3961	14.6390
6.0”	0.9437	0.9365	17.7651	15.7369

We have validated the model of the BeRP ball and reflectors, and now we turn to the neutron multiplicity counting experiment simulations.

3.2.2 The nPod Neutron Multiplicity Counting Detector

The neutron multiplicity counting experiment uses the nPod detector, an array of 15 ^3He proportional counters embedded in a polyethylene moderator wrapped in cadmium. The proportional counters are set in the moderator in two offset rows of eight and seven tubes, front to back respectively. The enveloping moderator is $16.6in \times 15.06in \times 4in$. An exhaustive description of nPod detector can be found in [38]. The nPod was positioned $50cm$ from the center of the BeRP ball to the front face as seen in Figure 3.4.

In previous simulations of these experiments, the complete three dimensional geometry is utilized as seen in this MCNP model in Figure 3.5.

We use the complete three dimensional model of the nPod in MCNP to generate a detector efficiency on the external surface of the BeRP ball. We treat the detector response function of the nPod σ_d as the product of an intrinsic efficiency $\epsilon_{int}(E)$, in terms the energy E of a neutron leaking from the BeRP ball, and a geometric efficiency factor ϵ_{geo}. The intrinsic detection efficiency of the nPod is determined by tallying the fraction of detected neutrons that enter the nPod with a particular energy E. To use this efficiency in our deterministic calculation we group average the continuous detector efficiency over the 44-group energy structure of our nuclear data, as seen in Figure 3.6.

The intrinsic efficiency is independent of geometric effects. The geometric efficiency is determined by computing the number of neutrons entering the nPod divided by the number of neutrons leaving the BeRP ball. The geometric efficiency ϵ_{geo} factor over the thicknesses of polyethylene is provided in Table 3.5.

We combine the intrinsic and geometric efficiencies to write the total detector response

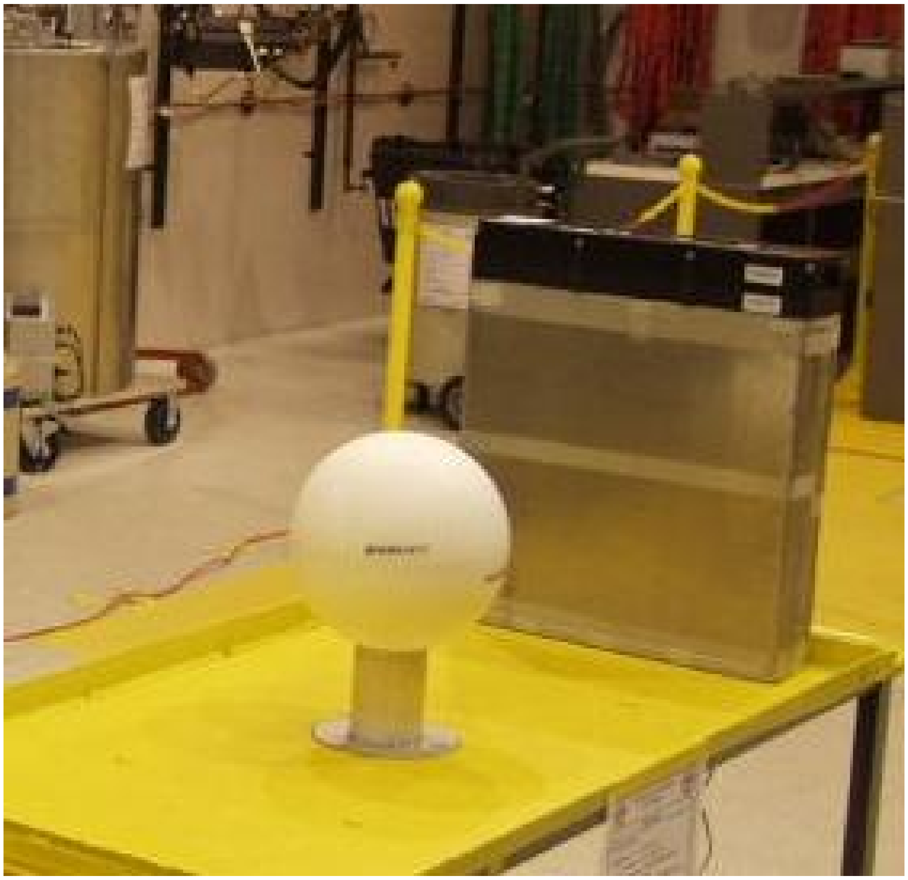

Figure 3.4: The nPod detector and the BeRP ball, enclosed by polyethylene reflectors, separated by 50 cm, center of BeRP ball to the face of nPod [39].

Table 3.5: Geometric efficiencies between the nPod and BeRP ball for various thickness of polyethylene reflector.

Reflector	ϵ_{geo}
0.0”	0.0515592924
0.5”	0.051855918
1.0”	0.0521520297
1.5”	0.0523893171
3.0”	0.0527103126
6.0”	0.0524855264

function as a function over the external surface of the BeRP ball,

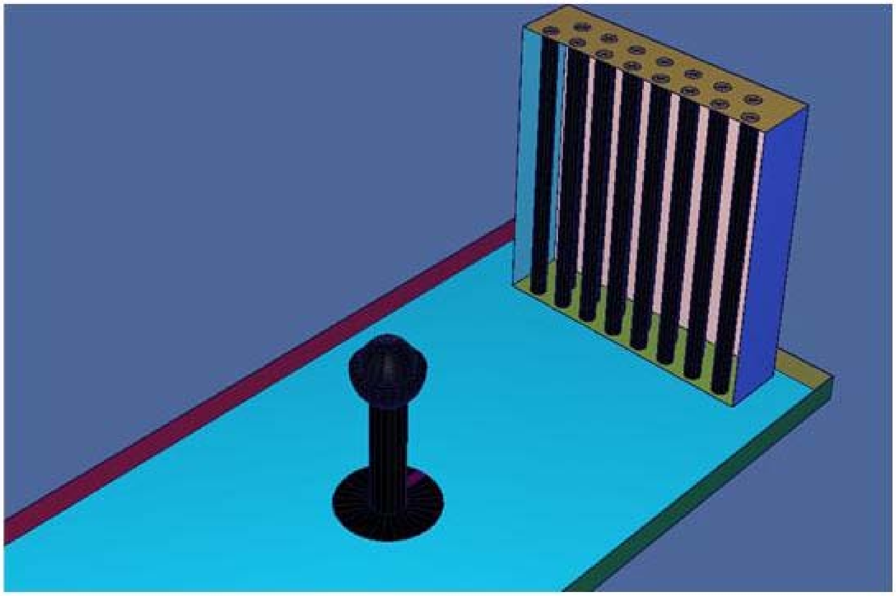

Figure 3.5: The MCNP model used to generate the effective nPod detection efficiency.

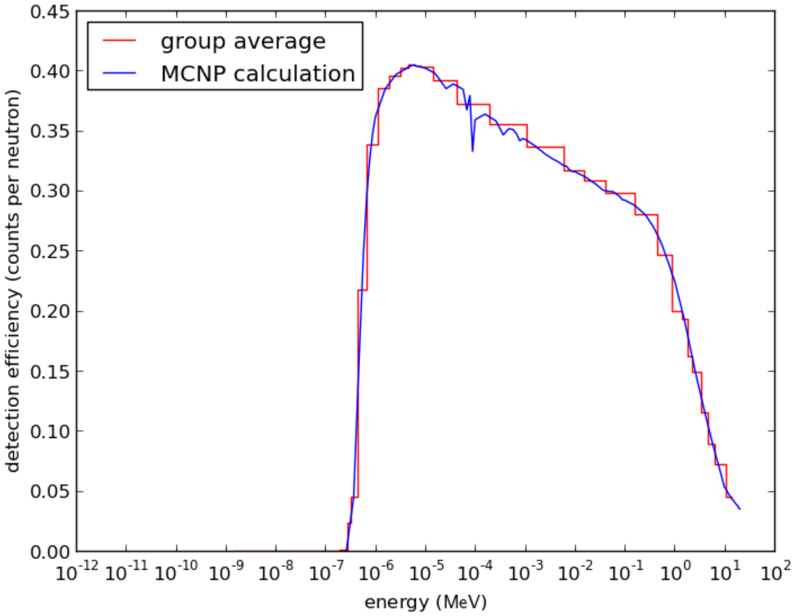

Figure 3.6: The effective nPod detection efficiency, generated by MCNP, averaged over the 44-group energy structure.

$$\sigma_d(\vec{r}, E, \vec{\Omega}) = \vec{n} \cdot \vec{\Omega}\delta(\vec{r} \in \partial V)\epsilon(E)\epsilon_{geo}. \tag{3.2}$$

Where $\hat{n}$ is the outward unit normal to the surface of the sphere ∂V. This formulation reduces the computational complexity of our model. The mean count rate R_1 is found by convolving the detector response function with the neutron leakage current, $\vec{j} = \vec{\Omega}\psi$,

$$R_1 = \int_{\vec{r}\in\partial V} d^2r \int dE \int_{\vec{n}\cdot\vec{\Omega}>0} d\Omega\epsilon_{int}(E)\vec{n} \cdot \vec{j}(\vec{r}, E, \vec{\Omega}) \tag{3.3}$$

Now we turn to comparing our calculations of the first three moments of the neutron multiplicity counting distribution to experimental values.

3.3 Mean of the Neutron Multiplicity Counting Distribution

We define the first moment in Eq. 3.3 as a continuous quantity. In the discrete form we write it as a sum product of the total neutron leakage by group J_g over the BeRP ball and the detector efficiency over that group $\sigma_{d,g}$, to give the mean count rate,

$$R_1 = \sum_{g=1}^{N_g} J_g\sigma_{d,g} \tag{3.4}$$

Alternatively, we can determine the mean count rate by using the first adjoint flux $\psi_1^\dagger$. We integrate the mean forward source with the first adjoint scalar flux $\phi_1^\dagger$, as the forward source Q is isotropic, to give,

$$
\begin{aligned}
R_1 &= \left\langle \psi_1^\dagger, Q \right\rangle \qquad (3.5)\\
&= \sum_{g=1}^{N_g} \sum_{i=1}^{N_r} \phi_1^\dagger(i,g) Q(i,g) \Delta V_i,
\end{aligned}
$$

where ΔV_i is the volume of a spatial cell. To not bias either formulation of the mean and the higher order moments, we average the analytically equivalent forward ,$\left\langle Q_q^\dagger, \psi \right\rangle$, and adjoint, $\left\langle \psi_q^\dagger, Q \right\rangle$, results that can be slightly numerically different.

We now compare our calculations with experimental data. We ensure the reliability of our calculations by performing a space-angle convergence study that is described in chap:AppConv. The neutron multiplicity counting distribution is defined over a range of coincident gate widths, from 16 μs to 4096 μs. First, we present the mean number of counts for the various thickness of polyethylene reflector in Figure 3.7. The mean number of counts is linear, as expected, because dividing by the gate width yields the same average count rate.

We compute the mean count rate of the neutron multiplicity counting distribution. To compare calculated and measured means, we multiply our count rate by the longest gate width of 4096 μs, to yield an average number of counts. There is good agreement between the experimental and calculated mean number of counts as seen in Figure 3.8. We observe an increase in the mean count rate with increasing polyethylene thickness because neutrons are slowed and reflected back into the plutonium. The returning neutrons induce more fissions as the cross section is largest at lower energies. This increase in the mean diminishes after a point in polyethylene thickness, because the leaking neutrons are sufficiently slowed down, as seen in Figure 3.9, into the insensitive energy regions of

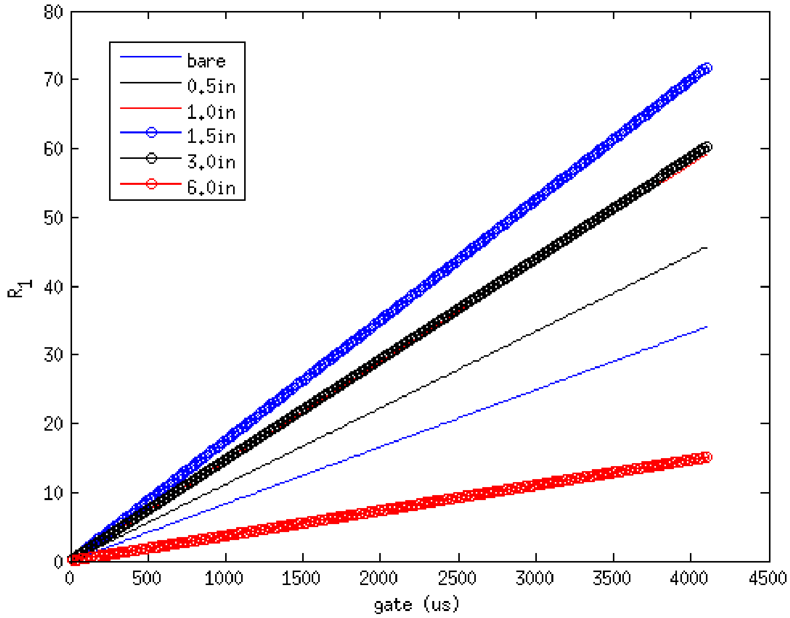

Figure 3.7: Mean number of counts of the neutron multiplicity counting distribution for various thicknesses of polyethylene reflector. Note the overlap between the 1.0 inch and 3.0 inch cases.

the detector efficiency, as seen in Figure 3.6.

The leakage spectrum J of the bare BeRP ball is nearly the same as the forward source Q, in Figure 3.10. The spectrum is similar because there is negligible slowing in plutonium metal and all neutrons are born with a fast spectra from either induced or spontaneous fission.

An important quantity in determining the moments of the neutron multiplicity counting distribution is the spatial importance map I to fission. For all moments, the q^{th} importance $I_q(\vec{r})$ describes the fraction of fission neutrons, as a function of where the fission occurs, that contribute to R_q. This is apparent in the form of any R_q response; where the fission term in the adjoint operator is explicitly considered, we have the importance multiplied by the total forward source of fission neutrons.

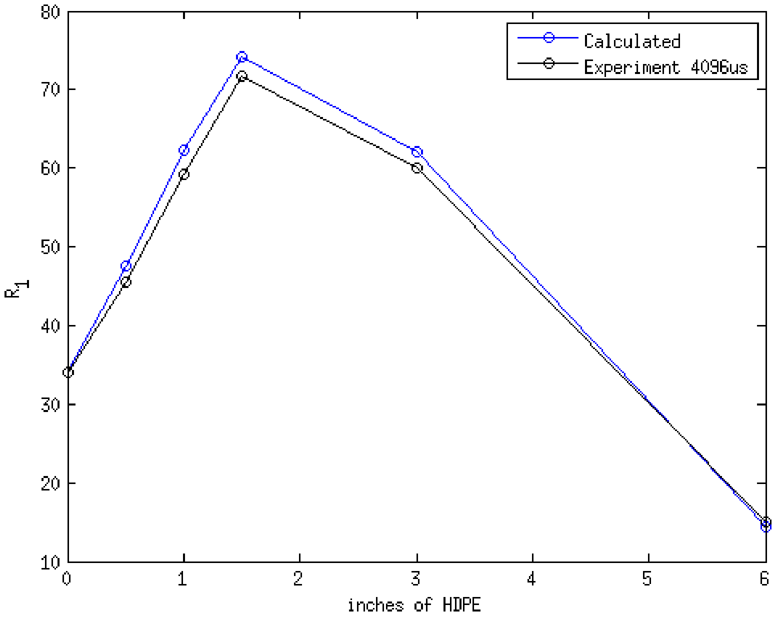

Figure 3.8: Experimental and calculated mean number of counts of the neutron multiplicity counting distribution for various thicknesses of polyethylene reflector.

$$
\begin{aligned}
R_q &= \left\langle Q_q^\dagger, \psi \right\rangle + \dots \\
&= \left\langle L^\dagger \psi_q^\dagger, \psi \right\rangle + \dots \\
&= \left\langle -\vec{\Omega} \cdot \vec{\nabla} \psi_q^\dagger + \dots \overline{\nu} \sigma_f \int_0^\infty dE' \int_{4\pi} d\Omega' \frac{\chi}{4\pi} \psi_q^\dagger, \psi \right\rangle + \dots \\
&= \left\langle -\vec{\Omega} \cdot \vec{\nabla} \psi_q^\dagger, \psi \right\rangle + \dots \langle I_q(\vec{r}), \overline{\nu} \sigma_f \psi \rangle + \dots
\end{aligned}
\tag{3.6}
$$

From the importance of fission neutrons we can garner that in the mean case, a fission that is induced in the core of the BeRP ball contributes more to R_1, this can be seen in the monotonically decreasing importances in Figure 3.11. Fission neutrons born near the center of the sphere are more likely to induce fission chain-reactions than those born

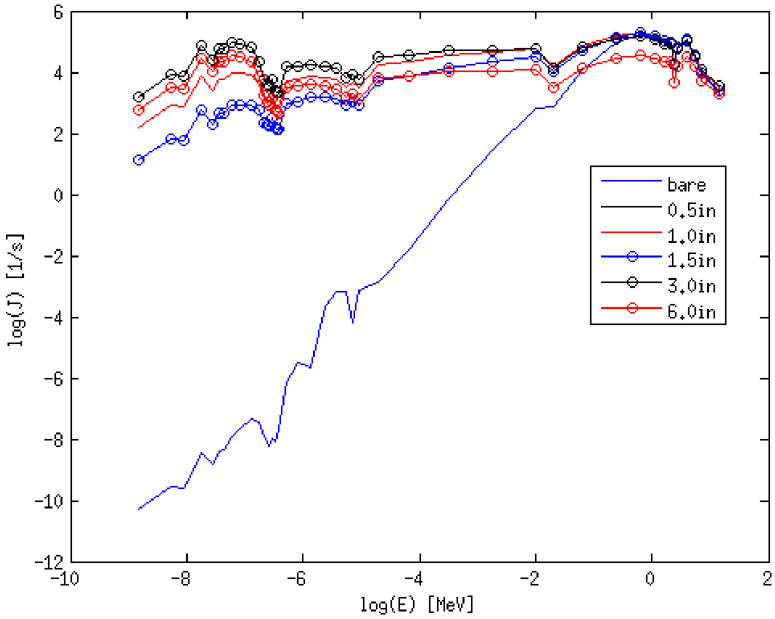

Figure 3.9: Calculated average neutron leakage J across energy for various thicknesses of polyethylene reflector.

near the boundary which are more prone to escape.

It is also insightful to examine the forward and adjoint fluxes. We compare fluxes between the bare BeRP ball and the 1.5 inch reflected case, Recall that the mean adjoint flux $\psi_1^\dagger$ represents the complete phase space importance map of fixed source neutrons to the first moment. The most striking feature shared by the two adjoint fluxes in Figure 3.12 is the trough around 10^{-6} MeV; this trough is due to a large absorption cross section in plutonium, neutrons born here will not contribute to the mean. The adjoint scalar flux shape in the polyethylene region closely resembles the spectrum of the detector response, as it is the boundary condition for the angular adjoint flux, neutrons are not ”born” in this region because there is no source term.

The reflector alters the adjoint flux within the plutonium region; this is important

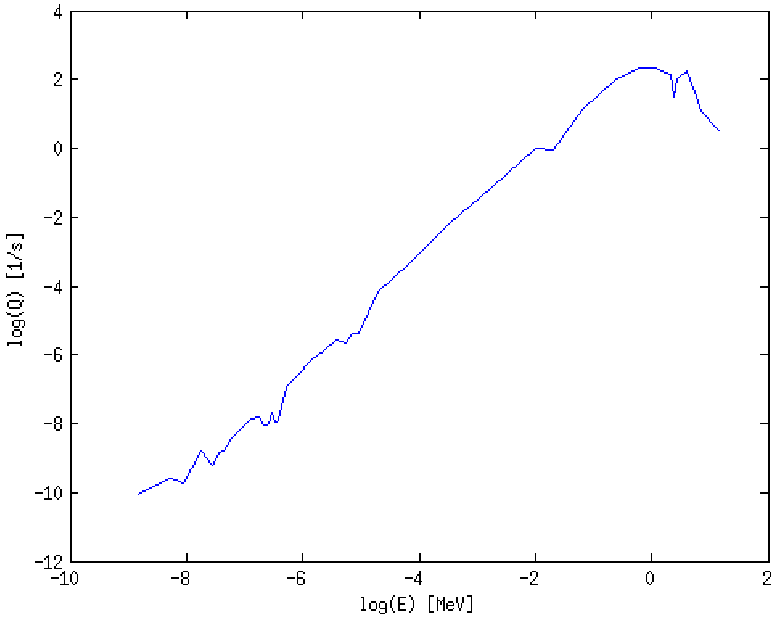

Figure 3.10: Average neutron source Q due to spontaneous fission of ^{240}Pu. The source is distributed uniformly over the volume of the BeRP ball.

as lower order adjoint fluxes are used in constructing the higher order moment adjoint source. The ratio of the reflected to bare mean adjoint scalar flux in the BeRP volume, is larger, on average, by a factor of 2.16. The ratio of computed mean count rates is 2.17; it is similar to the average ratio because the mean distributed source Q is identical. The maximum ratio between adjoint fluxes is 3.13 at the low energies where the fission cross section is largest and at the BeRP-polyethylene interface, as seen in Figure 3.13.

The last quantity we compare is the forward scalar flux ϕ, again between the bare and $1.5in$ of polyethylene arrangements, as it is constant across moments (unlike the varying adjoint flux $\psi_q^\dagger$ with order q). The principle difference in the scalar flux between the bare and reflected cases is the effect of slowing down, as seen in Figure 3.14. There obviously exists a large thermal neutron flux in the polyethylene but note how the fast spectra

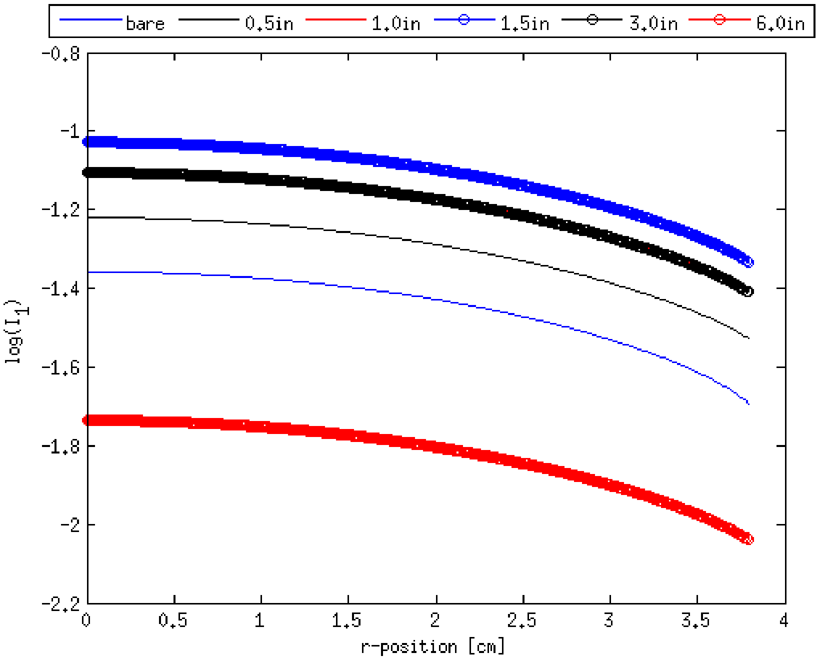

Figure 3.11: Spatial importance map of induced fission neutrons to mean R_1 for several thicknesses of HPDE reflector. Note: that the $3.0in$ case overlaps with the 1.0 inch case.

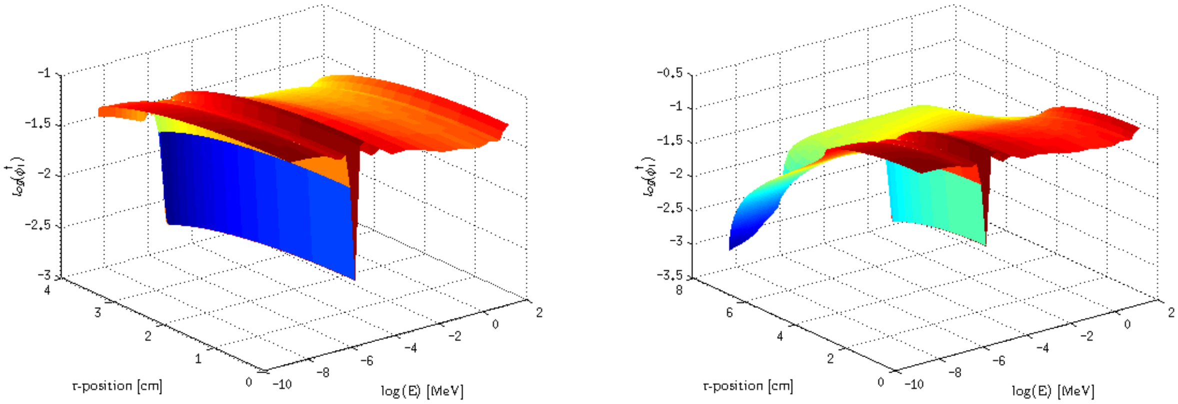

Figure 3.12: Mean adjoint scalar flux $\phi_1^{\dagger}$ for the bare (left) and reflected by 1.5 inch of polyethylene (right).

inside the plutonium is now smeared when compared to the fission spectra of the bare BeRP ball, as neutrons are slowed down in the reflector. The thermal flux of neutrons

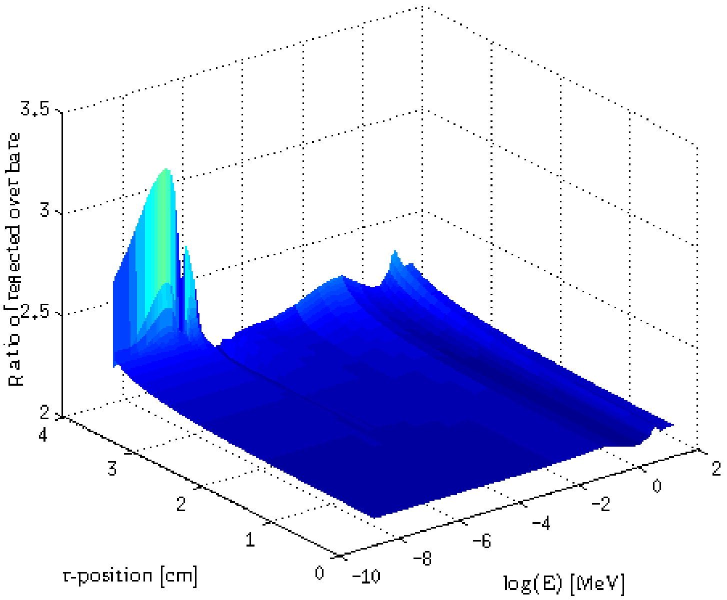

Figure 3.13: Ratio of mean adjoint scalar fluxes: 1.5*in* polyethylene:bare, over the plutonium region.

in the plutonium is still small as the fission sources are fast and slowing neutrons must pass through the resonance absorption region.

Our model for the mean of neutron multiplicity counting distribution agrees surprisingly well with experiment, given our assumptions and simplifications. Having an accurate mean is critical to determining the higher order moments because each moment is coupled to the mean adjoint flux via the adjoint source term; the SA closing equations, and the moment sensitivities, are both functions of the mean.

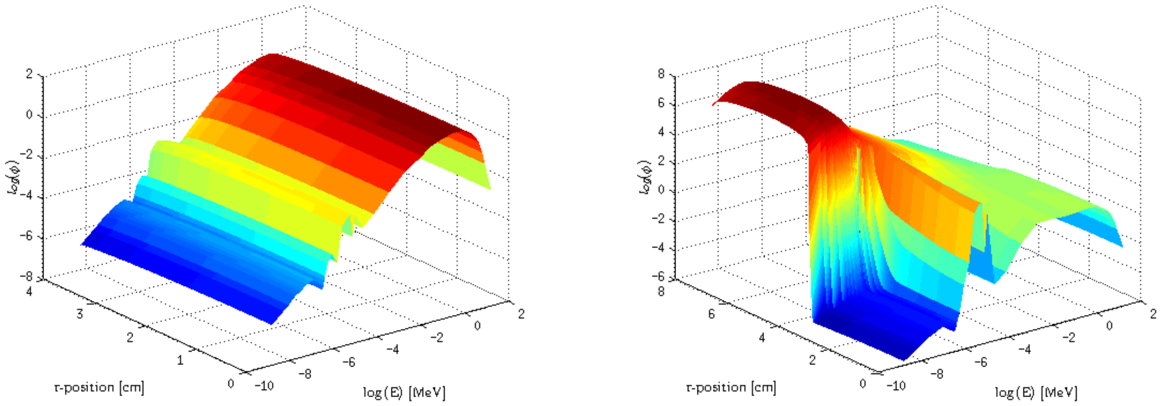

Figure 3.14: Forward scalar flux ϕ for the bare (left) and reflected by $1.5in$ of polyethylene (right).

3.4 Second Moment of the Neutron Multiplicity Counting Distribution

Now we consider the excess second moment of the neutron multiplicity counting distribution, where

$$R_2 = H_2 \tag{3.7}$$

First, we will show that our calculated second moment excess is in good agreement with experiment across all thicknesses of polyethylene. Then we consider the Feynman-Y Y_2 (usually defined as Y in the literature but we define higher order variants) which is a measure of the relative deviation from Poisson statistics, across the coincidence gate widths and layers of polyethylene to show the asymptotic behavior that our calculations approximate. Next, we compare the Feynman-Y of the bare and 1.5 inch polyethylene cases, and show that our calculations capture the asymptote of the Feynman-Y. Finally, we compare importances, adjoint fluxes, and adjoint sources, between our standard comparison cases (bare and 1.5 inch polyethylene).

First, we compare the second moment excess between the calculated and the longest experimental gate width of 4096 μs. As in the mean, we multiply the calculated R_2 by the gate width to put our calculated rate in terms of the number of coincident neutrons. In Figure 3.15 we see that there is fair agreement between experiment and calculation. The same trend is present here as in the mean, Figure 3.8, where the error is largest with increasing magnitude of the moment, and is a combination of errors compounding between the downward coupling between moments and is visually amplified by considering absolute, not relative, error.

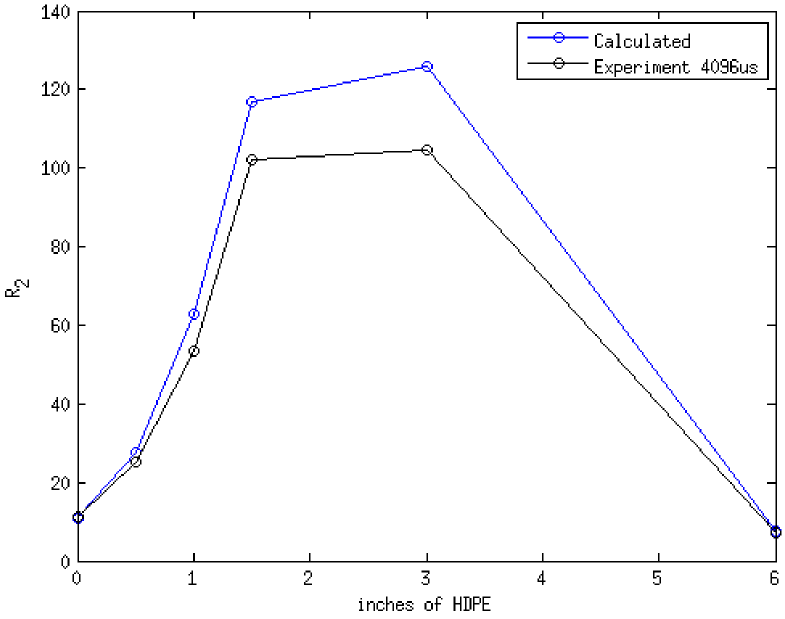

Figure 3.15: Second moment excess to Poisson, $R_2 = H_2$, across all polyethylene cases comparison between calculation and experiment at 4096 μs gate width.

The increase in the second moment excess with increasing reflector thickness is a direct consequence of the increased importance of induced fission neutrons to the second moment. The effect is similar for spontaneous fission source neutrons because the fission spectra of induced and spontaneous fissions are nearly identical. As reflector thickness increases, so does the contribution of fission neutrons as observed in Figure 3.16. The importance I_2 falls off towards the boundary because a neutron born in the center of the sphere is more likely to induce a chain-reaction, compared to a neutron born near the boundary. As in the mean case importance, the 6 inch reflected importance decreases due to the minimal nPod detection efficiency with regards to slow neutrons.

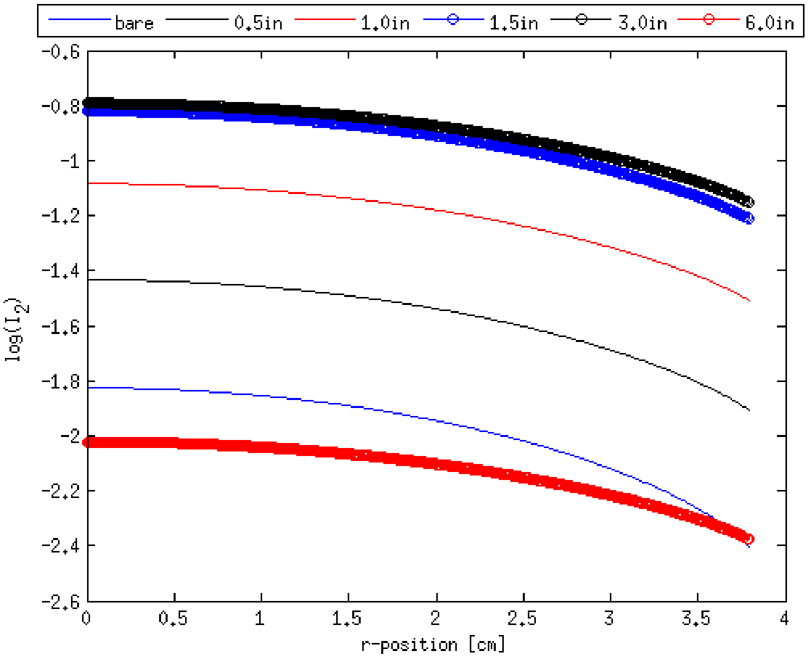

Figure 3.16: Spatial importance map of induced fissions to second moment excess R_2 contributions for thickness of reflector.

A more illustrative manner to evaluate the second moment is the Feynman-Y, a measure of the relative excess variance between the neutron multiplicity counting distribution and a Poisson distribution. We calculate the excess variance R_2 Eq. 2.25, and rewrite the equation for the Feynman-Y as a ratio of the second moment excess and the mean. Where we begin with the usual definition of the variance, $\sigma^2 = \overline{n^2} - \overline{n}^2$.

$$\begin{aligned} Y_2 =& \frac{\sigma^2}{\overline{n}} - 1 \\ =& \frac{\overline{n^2} - \overline{n}^2 - \overline{n}}{\overline{n}} \\ =& \frac{\overline{n(n-1)} - \overline{n}^2}{\overline{n}} \\ =& \frac{R_2}{R_1} \end{aligned} \tag{3.8}$$

Y_2 goes to zero if the neutron multiplicity counting distribution is pure Poisson, which only occurs in fission-less (induced or spontaneous) systems. The Feynman-Y is a function of gate width because it depends on detecting fission chain-reactions, which depend on neutron generation time. After a sufficiently long gate width the Feynman-Y reaches an asymptote, which generally increases with neutron multiplication and means we have a long enough gate to detect the neutron dispersion in chain-reactions. We observe this asymptotic behavior in the experimental data in Figure 3.17 and note that the asymptote increases with multiplication/thickness of reflector. However, the asymptote drops for the 6.0 inch case, the case with greatest multiplication, because the neutron spectrum is so slowed that the nPod is no longer sensitive to the bulk of neutrons. It is also insightful to note that with increasing reflector thickness the Feynman-Y requires more time to reach the asymptote because of increased neutron generation time resulting from neutron moderation.

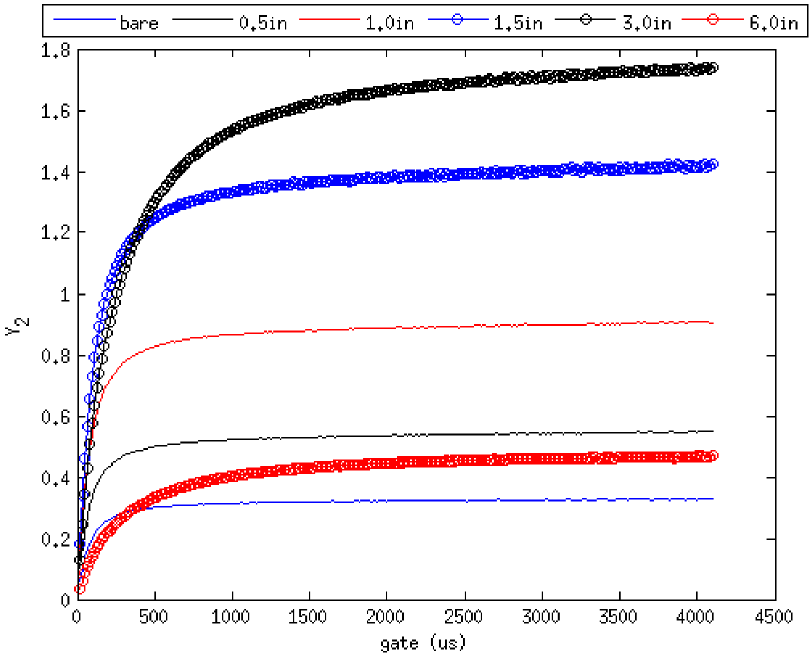

Figure 3.17: The experimental Feynman-Y (Y_2) across gate widths and over all thickness of polyethylene reflector.

Our calculations capture the asymptotic value of the Feynman-Y, as we perform a steady state calculation that corresponds to an infinite gate width. We compare our calculated Feynman-Y to the asymptotic values for our comparison cases, bare and 1.5 inch, in Figure 3.18. We see good agreement for the bare BeRP ball and reasonable agreement for the reflected BeRP ball. Again, the point of these calculations is not to be as accurate as possible, given our simplified model, but to be accurate enough to demonstrate the newly developed SA of the moments.

The effect of adding 1.5 inch of polyethylene reflector, when compared to the bare BeRP ball, is observable in the second moment adjoint scalar fluxes Figure 3.19. Both cases possess the resonance absorption "trench", though for the reflected flux it is less pronounced. In the bare case, source neutrons born near the boundary are unlikely to

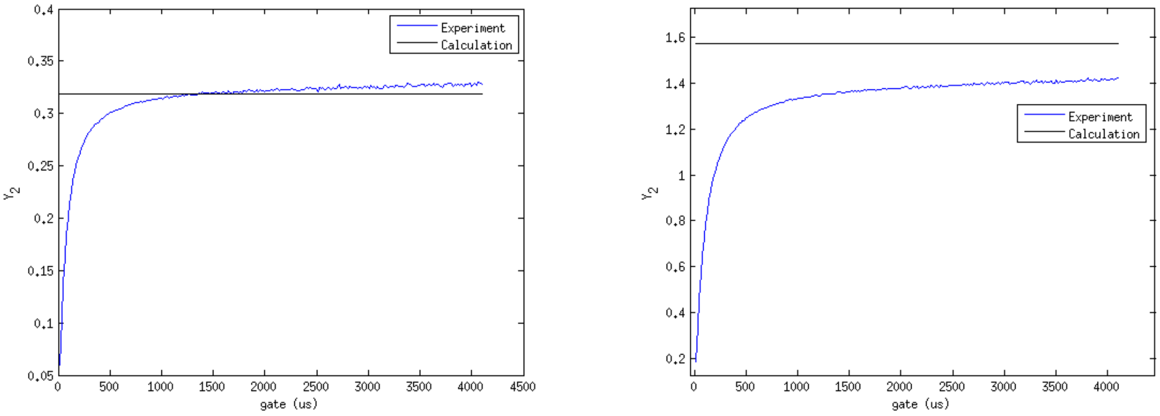

Figure 3.18: Asymptotic behavior of Feynman-Y for bare (left) and 1.5in polyethylene (right), across experiment coincident gate widths compared to calculated.

induce fission chains and neutrons that are born in the resonance absorption region are exceptionally unlikely to induce fission chain-reactions. By adding reflector, neutrons born in the absorption region, even those near the edge of the BeRP ball, have the chance to slow down in the reflector, completely out of the resonance energies, and are more likely to induce fission chain reactions in the slow regions where the fission cross-section is largest.

To observe the differences between the bare and reflected second moment adjoint scalar fluxes, we consider the ratio of the reflected to bare BeRP ball in the plutonium region, as it is the only region where source neutrons are born Figure 3.20. The first observation, is that the reflected second adjoint flux is everywhere larger, meaning a source neutron will induce more fission chain-reactions that contribute to the second moment excess. The most dramatic increase occurs at the boundary of the plutonium, because neutrons that could leak in the bare case are now more important because they can reflect/slow in the polyethylene. The effect of polyethylene is most notable at the

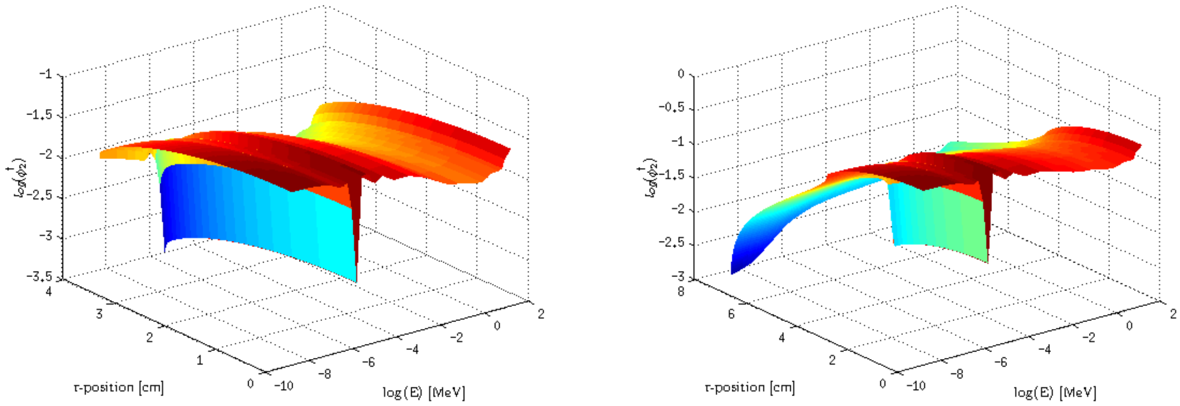

Figure 3.19: Log of second moment adjoint scalar flux $\psi_2^\dagger$ for bare (left) and 1.5in polyethylene (right).

BeRP boundary in the resonance absorption energy (around 10^{-6} MeV). By adding the reflector, the maximum ratio of fluxes is 78.33 meaning a neutron born in this region of phase space contributes significantly more. The average ratio of the second adjoint scalar fluxes over all space-energy is 10.41 and corresponds closely to the the ratio of second moment excesses between reflected and bare of 10.76.

Finally, we consider the second moment excess adjoint source terms $Q_2^\dagger$ between the bare and reflected cases in Figure 3.21. The source term accounts for doubles that are constructed by correlated pairs of singles. The second adjoint source is a product of two terms, one energy dependent and the other spatial dependent.

$$Q_2^\dagger = \overline{\nu(\nu-1)(E)}\sigma_f(E)I_1(\vec{r})^2 \tag{3.9}$$

In energy the adjoint source closely follows the profile of the fission neutron production cross-section, Figure 3.2, where we have the second factorial moment of fission neutron production $\overline{\nu(\nu-1)}$ instead of the average fission neutron production $\overline{\nu}$. The energy

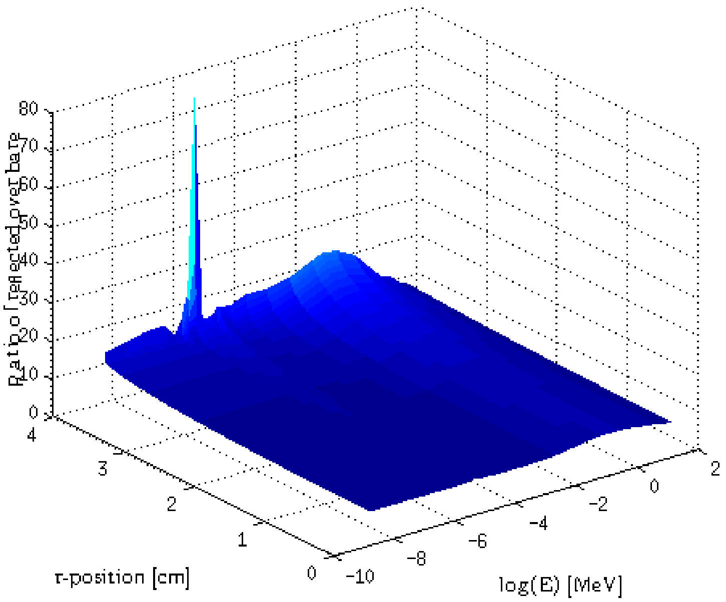

Figure 3.20: Ratio of second adjoint scalar fluxes: 1.5in polyethylene to bare, over the plutonium region.

dependent term is the same for the bare and reflected BeRP ball. The spatial portion, the square of the singles importances I_1^2, is dependent of the amount of reflector which is apparent in Figure 3.11. All mean importances across reflector thickness have similar shapes, monotonically decreasing with radius, and differ with respect to magnitude. Therefore, the two adjoint moment sources principally differ by a scaling factor that generally trends with the square of the ratio of mean adjoint fluxes, recall Figure 3.13.

Our computational model of the second moment excess accurately captures the measurements for both the bare and reflected BeRP ball. We capture the general trend of the second moment excess across all thicknesses of reflector. Our model also sufficiently captures the asymptotic values of the Feynman-Y for the bare and 1.5 inch of polyethylene cases. We turn now to the third moment excesses, where the extra Poisson features

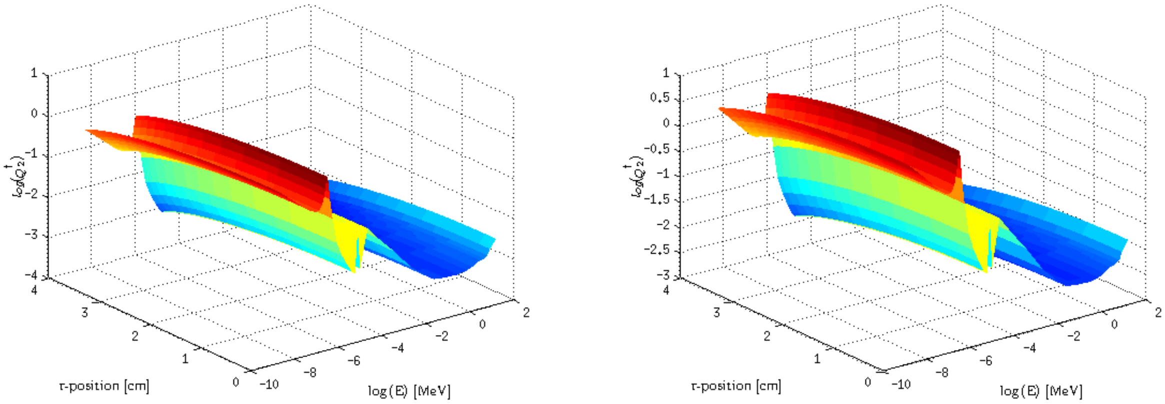

Figure 3.21: Log of second moment adjoint source term $Q_2^\dagger$ for bare (left) and $1.5in$ polyethylene (right).

found in the present moment will reoccur.

3.5 Third Moment of the Neutron Multiplicity Counting Distribution

We now consider the third moment excess, with respect to the Poisson distribution, of the neutron multiplicity counting distribution. First, we consider the two types of excess to the Poisson distribution. There is the absolute excess to Poisson statistics H_3,

$$\begin{aligned} H_3 =& \left\langle Q_3^\dagger, \psi \right\rangle + \left\langle Q_{s,3}^\dagger, S \right\rangle + 3R_1R_2 \\ =& R_3(\psi_2^\dagger, \psi_1^\dagger) + C_3(R_2, R_1). \end{aligned} \tag{3.10}$$

that accounts for true triples and triples formed by the accidental coincidence of the singles and correlated doubles. Then we consider the true triples R_3,

$$R_3 = \left\langle \psi_3^{\dagger}, Q \right\rangle + \left\langle \overline{\nu_s(\nu_s-1)(\nu_s-2)} I_{s,1}^3 + 3\overline{\nu_s(\nu_s-1)} I_{s,1} I_{s,2}, S \right\rangle \tag{3.11}$$

that are from fission-chains that produce detected triples. We compare both excesses, across thickness of polyethylene, for simulation and experiment. Then, as in the second moment case, we define a metric of the relative excess to the third moment, and observe asymptotic behavior. Next, we consider our comparison case, bare and 1.5 inch polyethylene, where we first compare H_3 and R_3 relative excesses. Finally, we compare the effects of addition of the reflector with respect to the third moment adjoint flux $\psi_3^{\dagger}$, spatial importances to induced fission, and the third moment induced fission adjoint source $Q_3^{\dagger}$.

First, we consider the agreement between simulation and experiment, at the longest available gate width (4096 μs) between both third moment excesses across several thicknesses of polyethylene in Figure 3.22. The general trend across thicknesses of polyethylene, for the both the mean Figure 3.8 and second excess Figure 3.15, of overestimating the experiment, and greater error with magnitude is also present in the third moment excesses. Disagreement between model and experiment is expected, due to the simplicity of our model, and due to the coupling of the moment equations. Our calculations are accurate enough for our purpose, and are successful in capturing the general trend and magnitude of the moment excess.

For the second moment, we used the Feynman-Y, a measure of the relative excess variance, as a metric to describe our system. The Feynman-Y had the excellent properties of asymptotic behavior with gate width and as a ratio of moments, provides a measure independent of absolute count rate. Additionally, as there is an increase in our calculations compared to experiment for all moments, this effect can be minimized/balanced

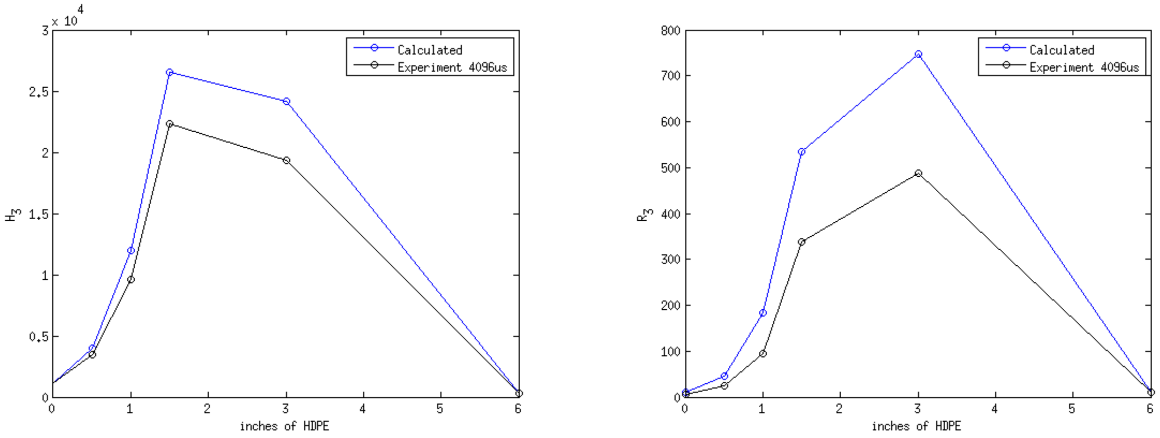

Figure 3.22: Comparison of third moment Poisson excess, H_3 (left), and independent triples excess, R_3, between simulation and experiment, using $4096\mu s$ gate, across thicknesses of polyethylene.

in the measure of relative excess. First, we consider the absolute third moment relative excess $Y_{H,3}$ which goes to zero for Poisson systems, that we define as

$$\begin{aligned} Y_{H,3} =& \frac{\mu_3 - \mu_1^3}{\mu_1^2} \\ =& \frac{H_3}{R_1^2} \\ =& \frac{R_3 + 3R_1R_3}{R_1^2}. \end{aligned} \tag{3.12}$$

As seen across the various thicknesses of polyethylene in Figure 3.23, the anticipated asymptotic behavior is present. The asymptote grows with multiplication and more moderated cases reach the asymptote more slowly due to the increase in neutron generation time. The excess $Y_{H,3}$ behaves similarly to the Feynman-Y, including the same drop of the asymptote for the 6 inch reflected case.

We turn our attention to our standard comparison case of bare and 1.5 inch polyethy-

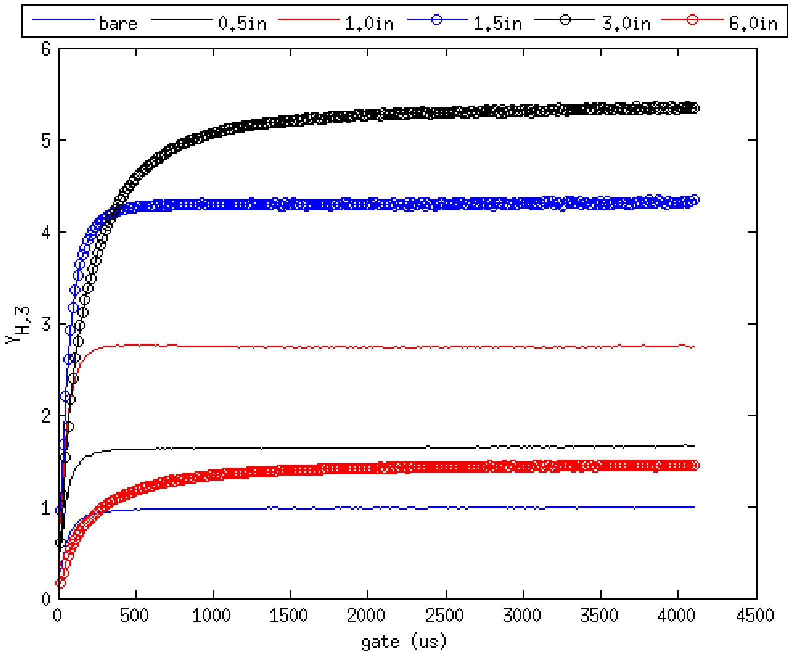

Figure 3.23: The experimental 3rd moment relative excess ($Y_{H,3}$) across gate widths and over all thickness of polyethylene reflector.

lene. First, we compare our calculation of the $Y_{H,3}$ asymptote to experiment in Figure 3.24. Our results are in fair agreement with experiment and exhibit behavior similar to the Feynman-Y comparison case Figure 3.18, in that the relative deviation from Poisson statistics increases with multiplication. We also underestimate the asymptote in the bare case and overestimate the asymptote in the reflected case, as in the second moment; recalling that our moment equations are downwardly coupled.

The differences between the bare and reflected third moment adjoint scalar fluxes are similar to those of the mean and second moment cases. What is interesting, is the ratio of the adjoint fluxes of the reflected to bare cases in Figure 3.25. The average ratio the adjoint fluxes is 52.37 and the ratio between the third moment independent triples excess R_3 is 54.04. These ratios have increased with reflector and with increasing order

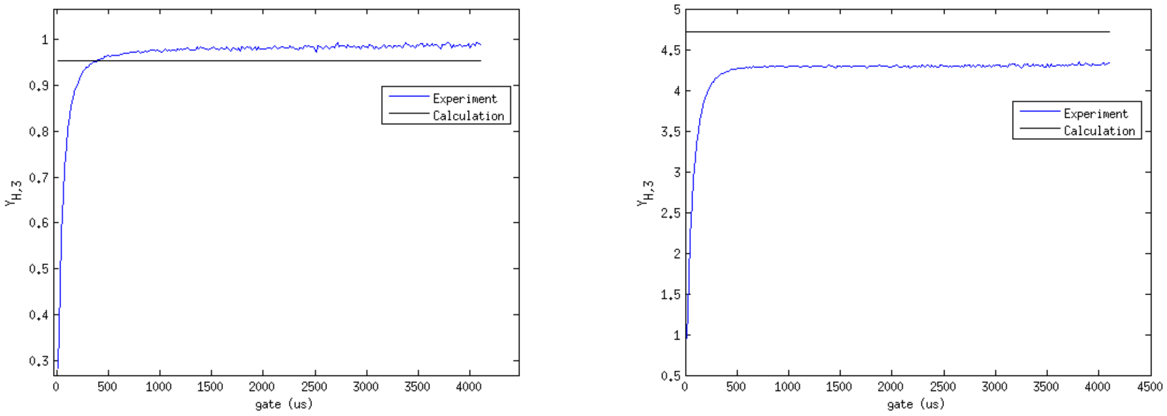

Figure 3.24: Asymptotic behavior of $Y_{H,3}$ for bare (left) and 1.5in polyethylene (right), across experiment coincident gate widths compared to calculated.

of moment excess. Similar to the second moment, the maximum ratio of adjoint fluxes occurs at the polyethylene-BeRP interface about the resonance absorption energies. For the third moment the maximum value of the ratio is 418.35, meaning that source neutrons born in the absorption resonance near the polyethylene-Pu interface are more likely to generate detectable triples compared to the bare BeRP ball.

The final comparisons that could be made between the bare and reflected case are the adjoint source terms and the spatial importance maps of induced fission. However, the information garnered is similar to the trends developed from the mean to the second moment, which continues to the third moment.

3.6 Conclusion

We construct our computational model of the neutron multiplicity counting experiment of the BeRP ball, a sphere of plutonium metal, both bare and reflected by several thickness of polyethylene. We verify our material and geometry model assumptions by calculating

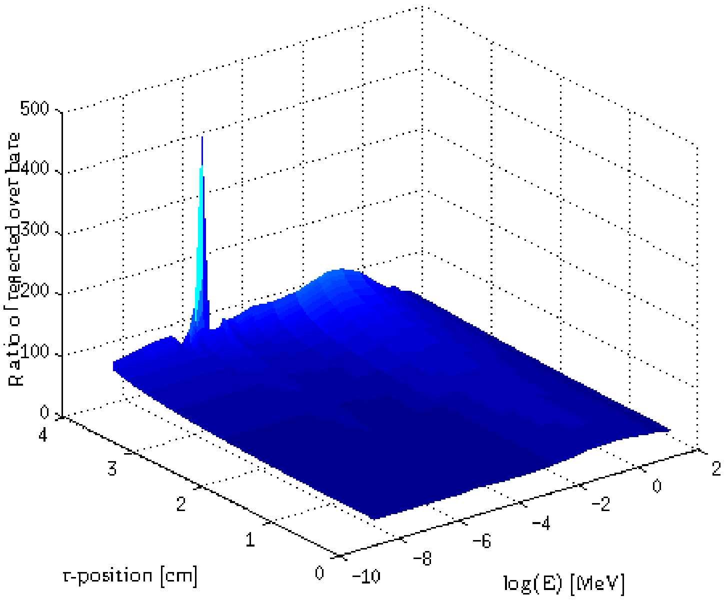

Figure 3.25: Ratio of third adjoint scalar fluxes: 1.5in polyethylene to bare, over the plutonium region.

k_{eff}, in comparison to published data on the BeRP ball. We model the nPod, the ^3He-tube neutron multiplicity counter, as a detection efficiency on the surface of sphere; the efficiency was calculated using MCNP.

We compare our deterministic calculations to experiment for the first three moments of the neutron multiplicity distribution and good agreement is observed given our model simplifications. Our measures of relative excess with respect to pure Poisson statistics for the second (Feynman-Y, Y_2) and third moments ($Y_{H,3}$) captures the asymptotic behavior and the expectation of increased asymptote value with increased neutron multiplication.

Chapter 4

Moment Sensitivity Analysis

4.1 Introduction

We begin by examining the relative sensitivity coefficients of the first three moments to the transport parameters of our neutron multiplicity counting experiment. We compare the sensitivities between the bare BeRP ball and the 1.5 inch polyethylene reflected BeRP ball. The addition of reflector increases the sensitivity of the moments of the neutron multiplicity counting distribution over all energies. The increase in sensitivity by the addition of reflector becomes readily apparent below 10 keV and increases by several orders of magnitude as low energies are reached because there is negligible slowing down in the bare plutonium sphere. For each configuration of the BeRP ball the sensitivity also increases with the order of moment because of the dependencies to lower moment solutions, governed by the moment SA closing equations.

To appreciate the differences of the energy dependent relative sensitivity coefficients across moments and configurations of polyethylene, we consider the ratios of our coefficients. We find that these ratios are informed by the differences between adjoint, forward, and closing equation fluxes. We find that these ratios are shaped by the ratios of flux spectra, both forward, adjoint, and their combination in the SA closing equations.

After we explore the energy dependent relative sensitivity coefficients, we consider the sensitivity of scalar parameters, such as nuclide density, and we also group collapse the energy dependent sensitivity coefficients. By energy-group collapsing the relative sensitivity coefficients to a scalar parameter, we can rank their influence on the moments and more directly compare the parameters across moments and configurations of reflector.

4.2 Relative Sensitivity Coefficients

It is more practical to introduce the relative sensitivity coefficient as the moments and the absolute sensitivity can vary greatly in magnitude. The relative sensitivity coefficient is defined as

$$S_{q,\alpha} = \frac{\alpha}{R_q}\frac{\partial R_q}{\partial \alpha}. \tag{4.1}$$

This enables us to directly compare the sensitivity with respect to parameters and moments that may differ in absolute value, by considering the effect of a relative perturbation of that parameter to the resulting relative change in the moment,

$$\frac{\delta R_q}{R_q} = S_{q,\alpha}\frac{\delta \alpha}{\alpha} \tag{4.2}$$

where $\delta\alpha$ is the perturbation in a parameter α, and δR_q is the resulting perturbation in the moment. In other words, $S_{q,\alpha)}$ can be interpreted as the relative change in R_q for a given relative change in α.

Most nuclear parameters are a function of energy and are defined at every energy group; consequently we need to collapse them in energy. This will allow us to rank the most influential parameters by type, for example maybe the moment is more sensitive to the fission cross-section than to the detector cross-section, which may not be true on a group by group comparison. We form the energy-group collapsed relative sensitivity coefficient by energy averaging the parameter and multiplying by the energy integrated sensitivity coefficient,

$$\overline{S_{q,\alpha}} = \frac{\overline{\alpha}}{R_q} \sum_g \frac{\partial R_q}{\partial \alpha_g} \tag{4.3}$$

where $\overline{\alpha}$ is the energy averaged value of the parameter.

We use the relative sensitivity coefficient to compare the effects of polyethylene reflector and across the moments, up to third order. The forward flux spectrum strongly influences the shape of the relative sensitivity coefficient. We arrive at the forward scalar flux spectrum dN/dE in each region by integrating over space and then normalizing with respect to energy,

$$\frac{dN}{dE} = \frac{\int_V d^3r\phi}{\int_0^\infty dE \int_V d^3r\phi} \tag{4.4}$$

There are three spectra that concern us as seen in Figure 4.1, the polyethylene region and the BeRP ball in bare and 1.5 inch reflected configurations.

The fast regions of the spectra are nearly identical but the spectra increasingly differ with softening. The effect of slowing down in the polyethylene is readily apparent with the slow spectrum being more dominant in the polyethylene and smaller in the bare Pu by many orders of magnitude. Considering the flux spectra is illuminating because the sensitivity coefficient for a physical quantity, such as the fission cross-section is only a function of energy.

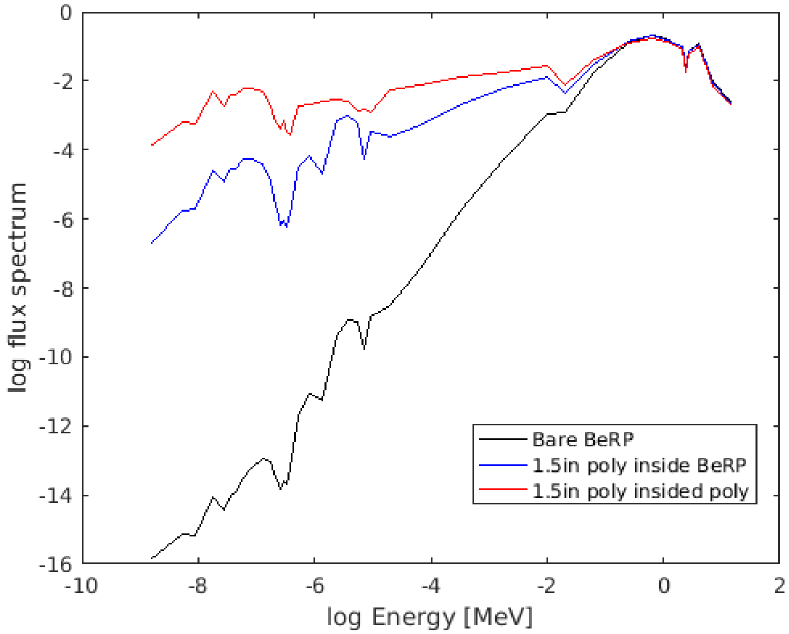

Figure 4.1: Spectra of the forward scalar flux in the polyethylene region, and inside the Pu region in bare and reflected (1.5in) configurations.

4.2.1 Fission Cross-Section of ^{239}Pu

The first parameter we consider is the fission cross-section because it is the most reoccurring parameter in our moment equations and associated sensitivity equations. It is present in the forward/adjoint operators and in the adjoint and forward closing equation source terms. As expected the relative sensitivity coefficient of the macroscopic fission cross-section of ^{239}Pu increases with increasing moment and is particularly larger in the slow region when reflector is added, as seen in Figure 4.2. The general profile of the relative sensitivity coefficients follows the spectra seen in Figure 4.1.

The log-log plot of the relative sensitivity coefficient is illuminating, but more details can be seen if we take the ratios of sensitivity coefficients across moments and across configurations of the BeRP ball. First, we consider the ratio of the moments of the

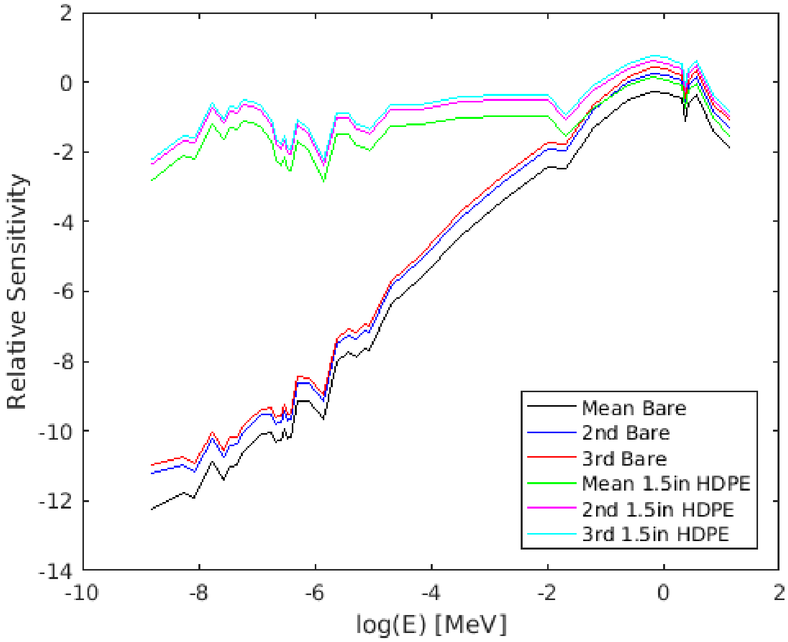

Figure 4.2: Relative sensitivity coefficient for the macroscopic fission cross-section of ^{239}Pu, across all moments and configurations of polyethylene.

bare BeRP ball. Over all energies, we divide the second and third moments by the first moment sensitivity coefficient and finally we consider the ratio of the third moment over the second. As seen in Figure 4.3 the greatest change between the higher order moments and the mean occurs in the thermal regions where the actual relative sensitivity coefficients are at a minimum. However, the actual fission cross-section is largest in the thermal region and fission chain-reactions that lead to doubles or triples ought to be increasingly sensitive to this energy region. The ratio of the third moment to the second moment is less pronounced when compared to the ratios with respect to the mean but the third moment is everywhere larger as our sensitivity equations would indicate.

Now, we consider the ratios of the relative sensitivity coefficients of the fission cross-section for the 1.5 inch polyethylene reflected BeRP ball in Figure 4.4. The most inter-

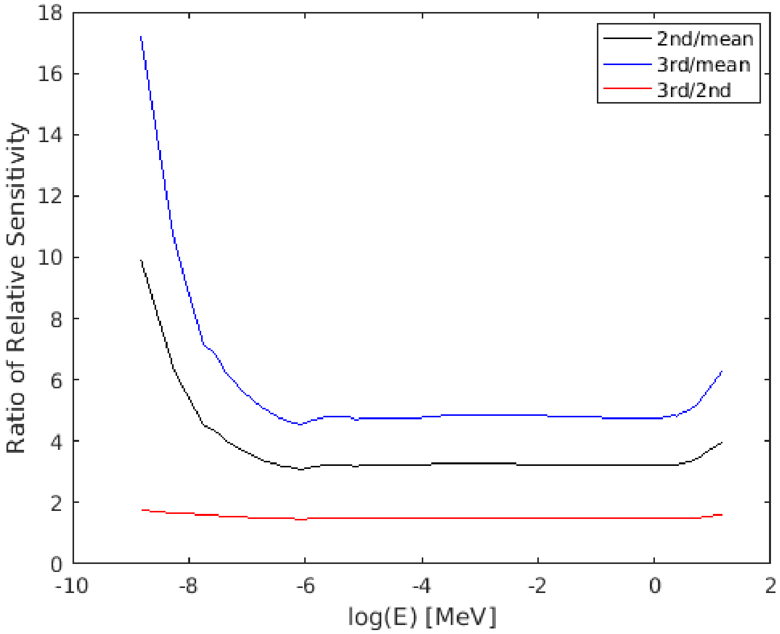

Figure 4.3: Ratio of the relative sensitivity coefficient for the macroscopic fission cross-section of ^{239}Pu with respect to each moment, for the bare BeRP ball.

esting feature is the notch in the bump around 10^{-5} MeV, which is around the resonance absorption region. This absorption feature is far more prevalent in the reflected case as was seen in ratio of the the adjoint fluxes between polyethylene and bare, over the Pu region, in Figure 3.13, Figure 3.20, and Figure 3.25, because this energy domain is not reached by the bare case due to the lack of slowing down. Apart from this feature, the ratios increase with the order of the moment and the rising tails at 10 MeV are due to the difference between the moments of p_ν (e.g. $\overline{\nu(\nu-1)\ldots}$) that dominate each moment, recall Figure 3.3.

Finally, we see how the relative sensitivity coefficient for the fission cross-section changes for a given moment with respect to reflector. In Figure 4.5 we see that the overwhelming difference between the reflected and bare cases is in the thermal regions,

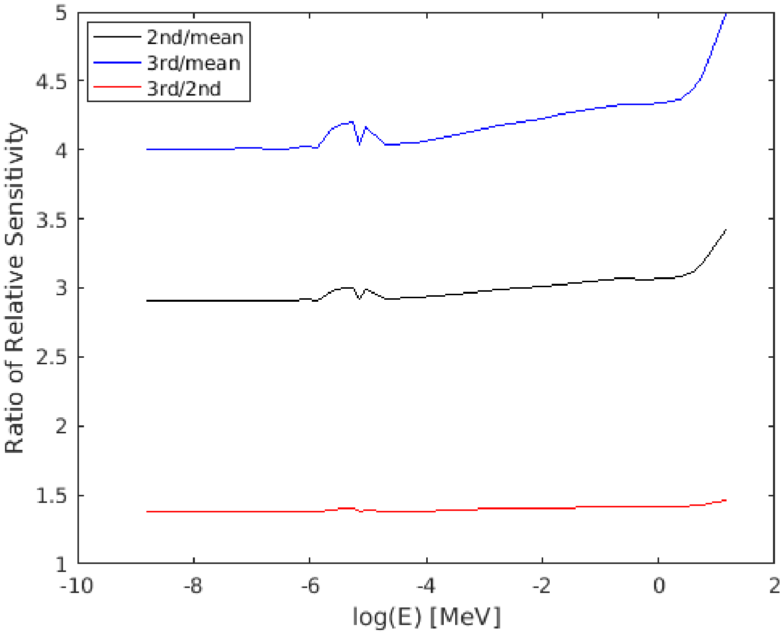

Figure 4.4: Ratio of the relative sensitivity coefficient for the macroscopic fission cross-section of ${}^{239}Pu$ with respect to each moment, for the 1.5in of polyethylene BeRP ball.

where the difference is around a factor of a billion, as in the bare case the thermal relative sensitivity coefficient is nearly zero. In the fast region, the reflected case is still more sensitive because of its larger neutron multiplication compared to the bare case.

The fission cross-section of ${}^{239}Pu$ is a highly influential parameter that is greatly affected by the addition of thermalizing reflector that enables neutrons to slow down to where the fission initiation probability is greatest. As the excess to the multiplicity counting distribution is principally governed by the fission parameters, we turn to the relative sensitivity coefficients of the moments of the neutron multiplicity distribution.

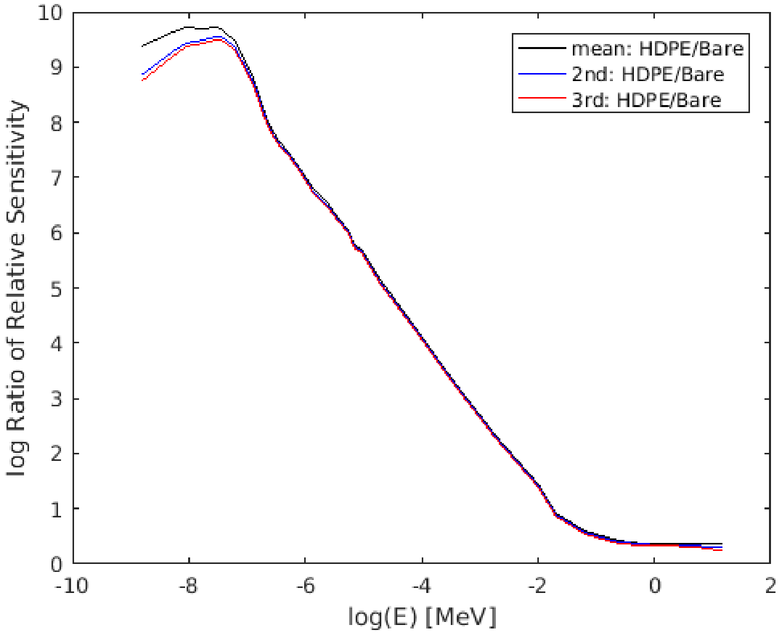

Figure 4.5: Ratio of the relative sensitivity coefficient for the macroscopic fission cross-section of ^{239}Pu for each moment with regards to 1.5in polyethylene over bare BeRP ball.

4.2.2 Moments of Induced Fission Multiplicity Distribution

Now, we consider the moments of the induced fission multiplicity distribution of ^{239}Pu. As with the fission cross-section, these parameters determine the excess to the Poisson moments because non-multiplying systems have purely Poisson moments. We consider the first three moments of the neutron multiplicity distribution:

- $\overline{\nu}$: appears in the forward and adjoint operators
- $\overline{\nu(\nu-1)}$: appears in the second and third moment adjoint and closing equation sources
- $\overline{\nu(\nu-1)(\nu-2)}$: appears in the third moment adjoint and closing equation sources

Each moment is derived from the same induced neutron multiplicity distribution p_ν but in this work we treat them as separate and independent quantities, as will be seen more explicitly when we consider the first-order perturbation truncation error in chap-five.

First, we consider the average of the neutron multiplicity distribution $\overline{\nu}$. The moments of the neutron multiplicity counting distribution are generally highly sensitive to the $\overline{\nu}$ as it is a fission parameter and is integral in determining the length of fission chain-reactions. The average is the only fission parameter that only appears in the transport operators. The higher order moments of the neutron multiplicity distribution only appear in the adjoint and moment closing equation fixed source terms, along with the fission cross-section. The relative sensitivity coefficient of $\overline{\nu}$ follows the expected trend, determined by the forward flux spectra and adjoints, as seen in Figure 4.6. The shape of the relative sensitivity coefficient is very similar to the fission cross-section as seen in Figure 4.2.

Much of the differences between the sensitivity coefficients are too minute to discern on the logarithmic scale. As above, we consider ratios of the relative sensitivity coefficients to distinguish the variation between moments. First, we consider the ratio of higher moments to the mean, and then the ratio of the third to the second moment in Figure 4.7. For the bare case the trends in magnitude between the ratios follows the same trend as the fission cross-section, with the third moment to the mean being the largest ratio. The second moment to the mean is similar to the third to the mean, as the the moment excesses R_3 and R_2 are similar in magnitude for the bare configuration. The similarity between sensitivity ratios of the second and third excess is evident in Figure 4.7, which is slightly greater than unity and is not constant.

When considering the ratios of the 1.5 inch polyethylene reflected case an interesting reversal occurs in the ordering of the magnitudes between moments between third to mean and second to mean. Also, the ratio between third and second moments has dropped

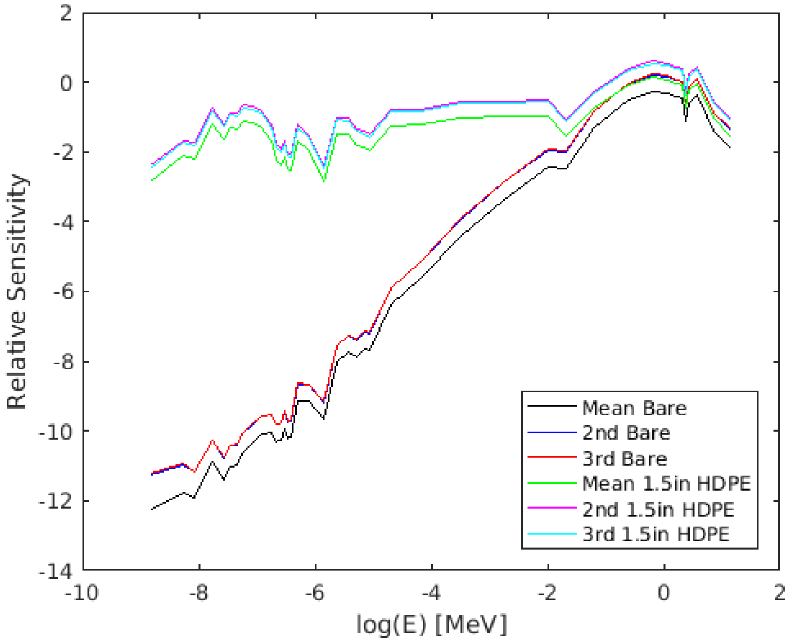

Figure 4.6: Relative sensitivity coefficient for $\overline{\nu}$ of ^{239}Pu, across all moments and configurations of polyethylene.

below unity, as seen in Figure 4.8. The notch feature in the ratios is accounted for, as in the fission cross-section above, by the ratio of adjoint fluxes in the Pu region.

The inversion of ratios is due to the higher order moment excesses being larger than the mean for the reflected case, unlike the bare case where the second and third moment excesses are both nearly one-third of the mean as seen in Table 4.1. One may expect the same inversion to occur in the fission cross-section polyethylene case but the higher order moment sensitivities are bolstered by the large high order moments of the neutron multiplicity distribution, in particular in the third moment by $\overline{\nu(\nu-1)(\nu-2)}$, where the fission cross-section appears but the average induced fission yield does not.

Next, we consider the ratio of the relative sensitivity coefficient for the average induced fission yield for each moment across configurations of reflector in Figure 4.9. As we have

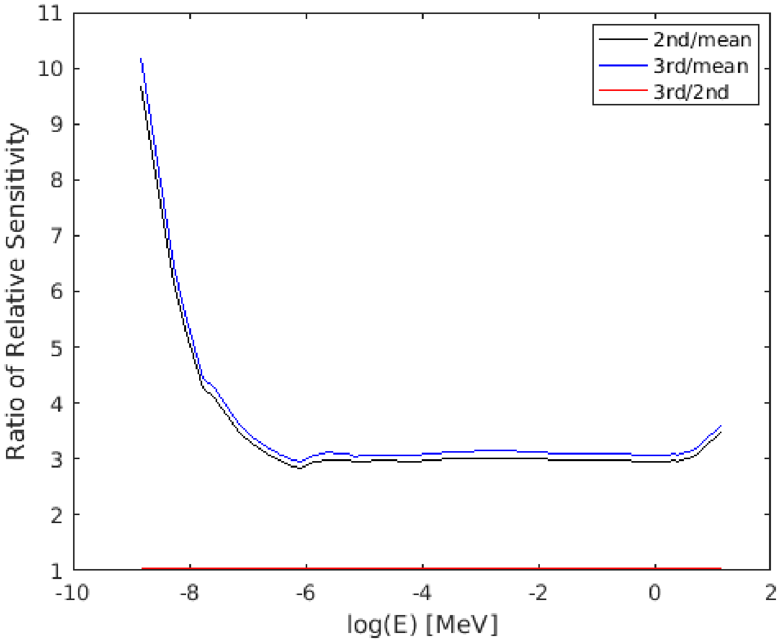

Figure 4.7: Ratio of the relative sensitivity coefficient for $\overline{\nu}$ of ^{239}Pu with respect to each moment, for the bare BeRP ball.

Table 4.1: Ratios of the moments for the bare and 1.5in polyethylene reflected BeRP ball.

Ratio/BeRP	Bare	1.5in poly
R_3/R_1	0.290	7.207
R_2/R_1	0.318	1.574
R_3/R_2	0.912	4.579

come to anticipate the reflected sensitivity coefficients are everywhere larger, implying greater sensitivity, and the reflected case is immensely greater in the thermal regions due to the bare BeRP ball being negligibly sensitive in this energy range.

We now turn to the moments of the induced fission neutron multiplicity distribution that exclusively appear in the adjoint moment source terms and in the associated SA closing equations. The second factorial multiplicity moment $\overline{\nu(\nu-1)}$ appears in the

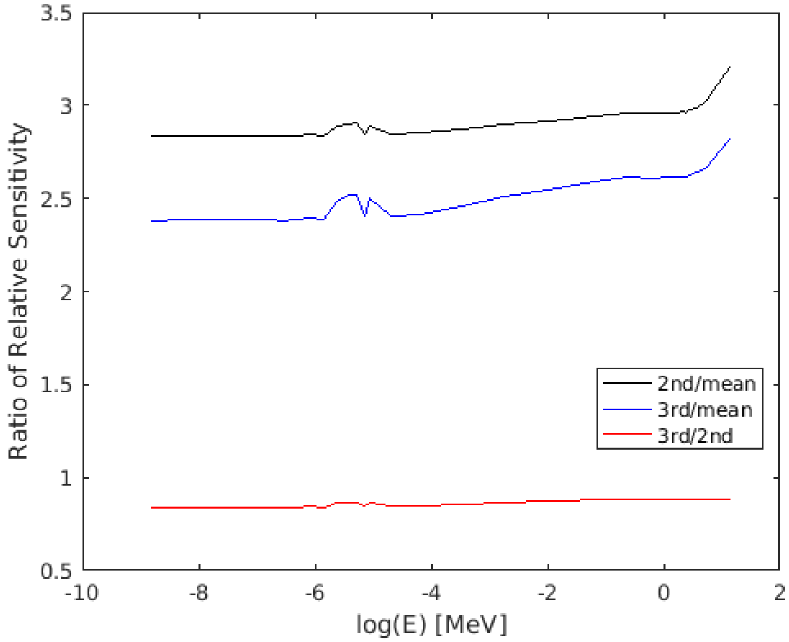

Figure 4.8: Ratio of the relative sensitivity coefficient for $\overline{\nu}$ of ^{239}Pu with respect to each moment, for the 1.5in of polyethylene BeRP ball.

second and third moment equations and has the general shape of a relative sensitivity coefficient that we expect from fission parameters, and is always multiplied by σ_f, as seen in Figure 4.10. The relative sensitivity coefficient is largest in the the fast region, even for the softened spectrum of the reflected Pu sphere, because the higher order moments of the induced fission multiplicity distribution significantly increase above 1 MeV, recalling Figure 3.3.

Finally, we turn to the third factorial moment of the induced neutron multiplicity distribution $\overline{\nu(\nu-1)(\nu-2)}$, which only appears in the third moment adjoint source term. The relative sensitivity coefficient follows the same trends between the bare and reflected BeRP balls as the other fission parameters, as seen in Figure 4.11.

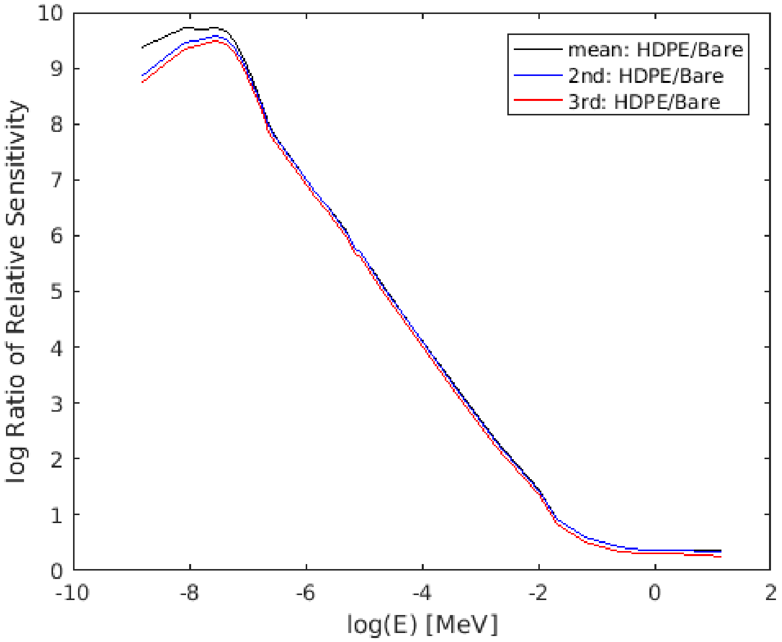

Figure 4.9: Ratio of the relative sensitivity coefficient for $\overline{\nu}$ of ^{239}Pu for each moment with regards to 1.5in polyethylene over bare BeRP ball.

Now we consider the last fission quantities, the induced and spontaneous fission neutron spectra.

4.2.3 Fission Neutron Energy Distribution

The final fission parameter we consider is the fission neutron energy distribution χ. We consider the energy spectrum of induced fissions from ^{239}Pu and from the ^{240}Pu spontaneous fission source. The induced fissions contribution from ^{240}Pu is neglected because the induced fission cross-section is small and the BeRP ball is predominately ^{239}Pu. As mentioned when developing our SA theory in chap-two, we treat the induced fission neutron distribution as independent of the inducing neutron energy.

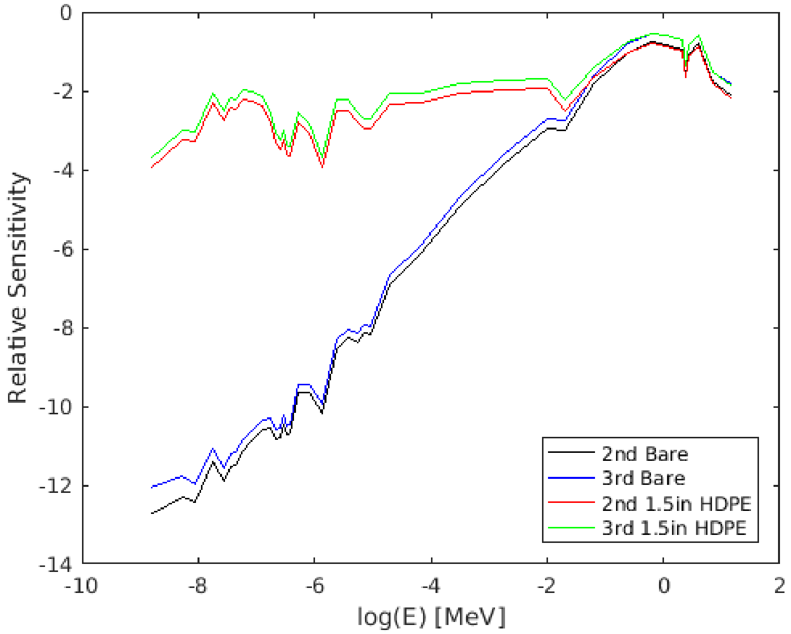

Figure 4.10: Relative sensitivity coefficient for $\overline{\nu(\nu-1)}$ of ^{239}Pu, across all moments and configurations of polyethylene.

Induced Fission

The fission neutron energy distribution is a unique parameter because it is the only non-integral production parameter in the forward transport operator and is a probability distribution. In the adjoint equations the fission neutron energy distribution appears in the operator and source terms in the importance functions, I_q; often appearing as products of importances. The most striking feature of the relative sensitivity coefficient is that the shape of the sensitivity is similar across all moments and states of reflector as seen in Figure 4.12. The fission distribution sensitivity does not drastically increase with the addition of reflector, as parameters above do, because the fission distribution is independent of the inducing fission neutron. However, the sensitivity does increase with increased multiplication as is seen in the ranking, from low to high, of the sensitivities

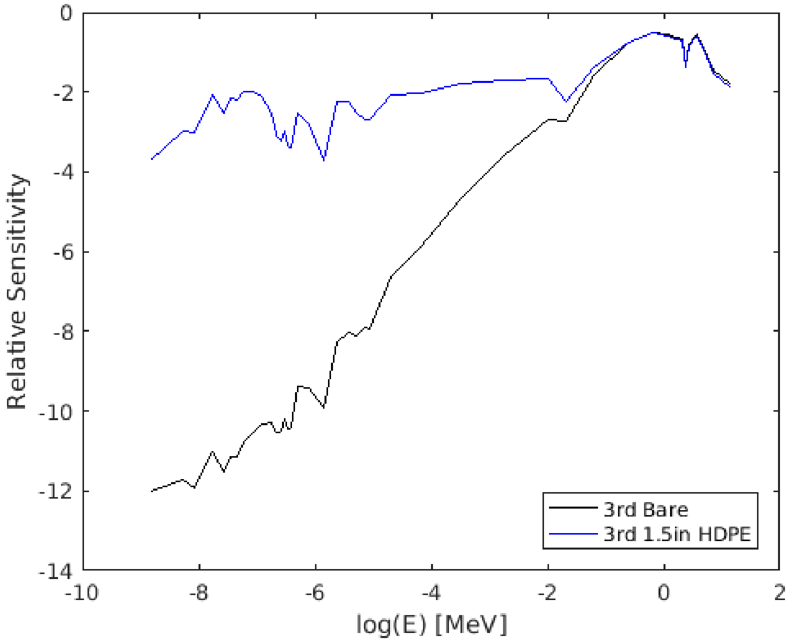

Figure 4.11: Relative sensitivity coefficient for $\overline{\nu(\nu-1)(\nu-2)}$ of ^{239}Pu, across all configurations of polyethylene.

in Figure 4.12.

As above, we consider the ratio of the sensitivities to observe the changes in the sensitivities across the moments for the bare BeRP ball in Figure 4.13. The main feature we observed is that the sensitivity increases with the order of moment. Additionally the rising edge with increasing energy is due to the higher-order induced fission multiplicities, e.g. $\overline{\nu(\nu-1)}$, that appear in the adjoint source terms, recall Figure 3.3.

Now, we consider the ratio of sensitivities for the reflected BeRP ball in Figure 4.14. As in the bare case the ratio in sensitivities across the moments is chiefly due to the induced fission multiplicities in the adjoint source terms.

Finally, we consider the ratio of the moments between the reflected and bare BeRP ball in Figure 4.15. The most striking feature is the spike around the resonance absorption

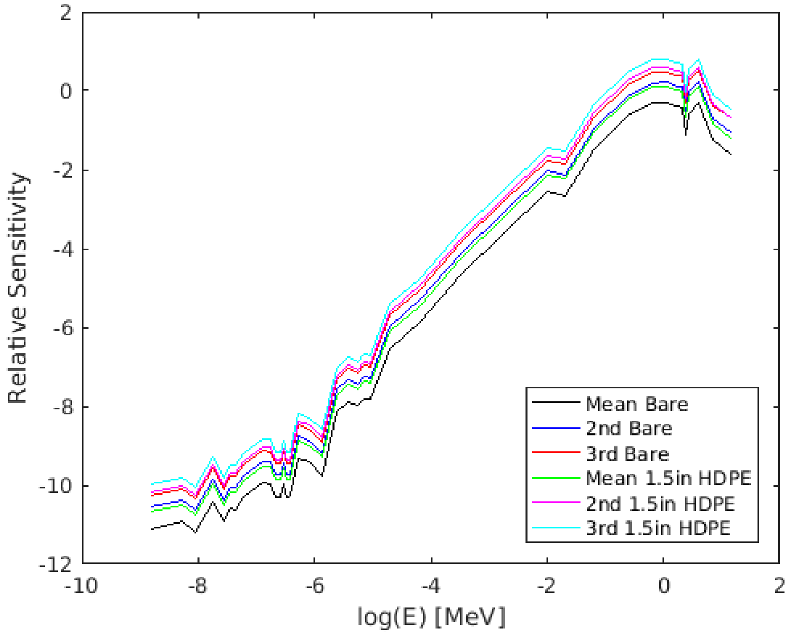

Figure 4.12: Relative sensitivity of induced fission distribution for ^{239}Pu.

region. In the reflected case fission neutrons born in this energy region, particularly those near the Pu-polyethylene interface, can be slowed and reflected back into the plutonium to continue fission chain-reactions. In the higher energy region, above 1 MeV, we observe the peak in the fission neutron distribution and notice a decline in the higher order moments. This decline, particularly for the higher moments corresponds to the decrease in the fission neutron energy distribution. At the highest energies there is decreasing difference between the bare and reflected cases because the fast neutrons have not been slowed in the reflector.

The induced fission neutron energy distribution is an important parameter that like the fission cross-section appears in every term of the higher moment adjoint source terms and SA closing equation source terms. It is also requires special consideration when evaluating perturbations as it must remain a probability distribution, i.e. it must integrate

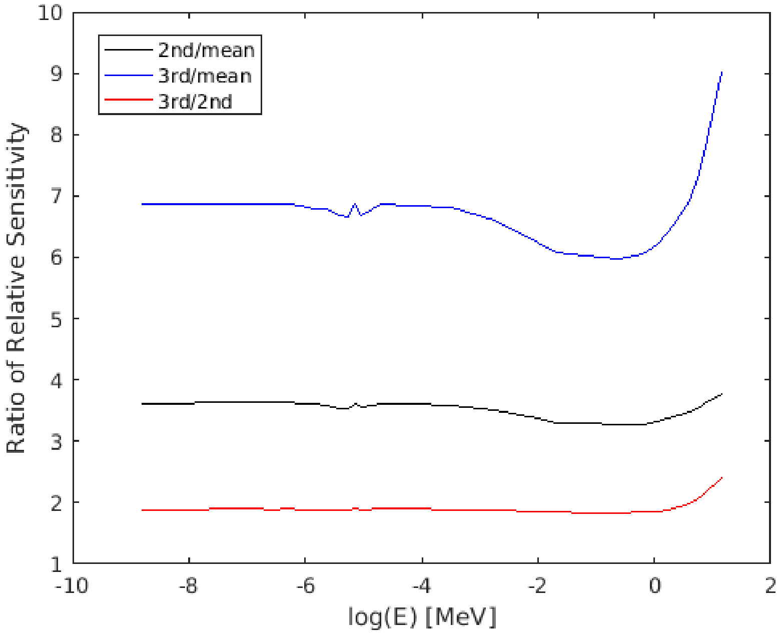

Figure 4.13: Ratio of sensitivities between moments of induced fission distribution for ^{239}Pu for the bare BeRP ball.

to unity, and therefore we do not directly consider its perturbations in the following chap-five.

Spontaneous Fission

The spontaneous fission neutron distribution χ_s is part of the forward source term Q that drives the entire multiplicity counting distribution measurement. As the forward source has its own high order neutron multiplicity moments, e.g. $\overline{\nu_s(\nu_s-1)}$, the spontaneous fission neutron energy distribution also appears in the source adjoint source terms for the moments above the mean and in the associated SA closing equations. We also make the assumption that the fission neutron energy distribution is independent of the number of spontaneous fission neutrons released.

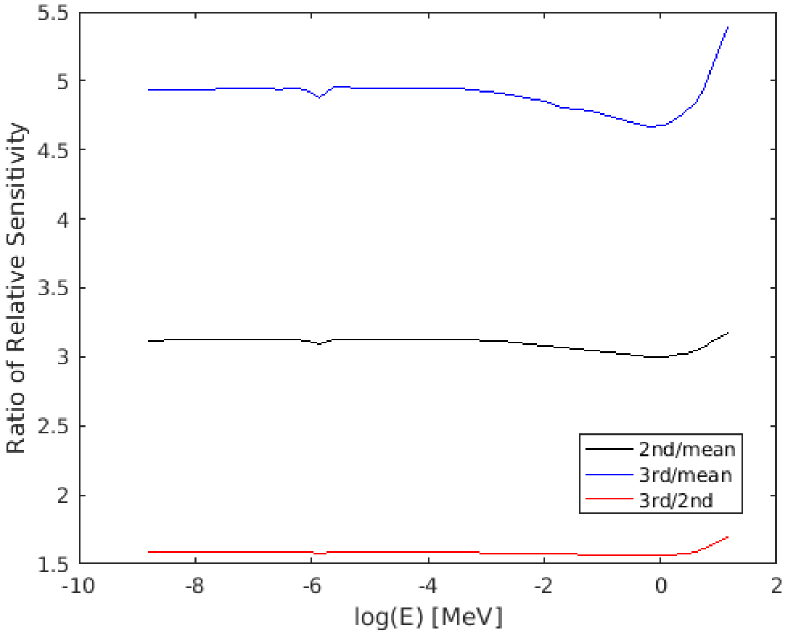

Figure 4.14: Ratio of sensitivities between moments of induced fission distribution for ^{239}Pu for the 1.5in polyethylene reflected BeRP ball.

We first consider the relative sensitivities across all moments for both the bare and reflected Pu sphere in Figure 4.16. The sensitivities are very similar for all cases and are less than the sensitives of the induced fission neutron energy distribution Figure 4.12. The sensitivity is less than the induced sensitivity because both systems have a neutron multiplication greater than one and the spontaneous fission contribution to the higher order moments is less than the induced fission contributions to the moment excesses. This is partially due to the smaller multiplicity moments of spontaneous fission neutrons Table 3.2.

Consider the ratio of the moments for the bare BeRP ball in Figure 4.17. The first feature to note is the small linear scale of the ratio. The principle differences occur in the lower energies where neutrons born here can induce fission chain-reactions that can

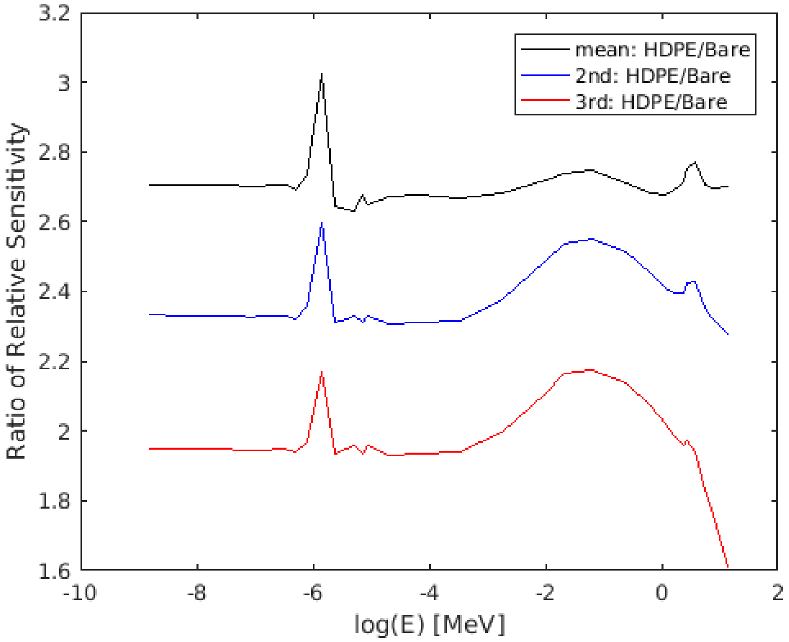

Figure 4.15: Ratio of sensitivities of induced fission distribution for ^{239}Pu for each moment between the reflected to bare BeRP ball.

lead to doubles and triples. Again we observe the spike in the resonance absorption region and observe little difference between the moments between 10 keV and 1 MeV, the most probable region for source neutrons to be born. The increased ratio beyond 1 MeV is due to source neutrons inducing fission chains where the higher order induced neutron multiplicity is largest. The differences between the third and second moments are minimal because they both describe excesses to the Poisson moments, unlike the mean.

Now consider the reflected ratios of the spontaneous fission neutron energy distribution in Figure 4.18. The ratios here are even smaller than the mean case because the addition of reflector diminishes the importance of the original source spectrum by slowing and spreading the neutron energy distribution throughout the plutonium region.

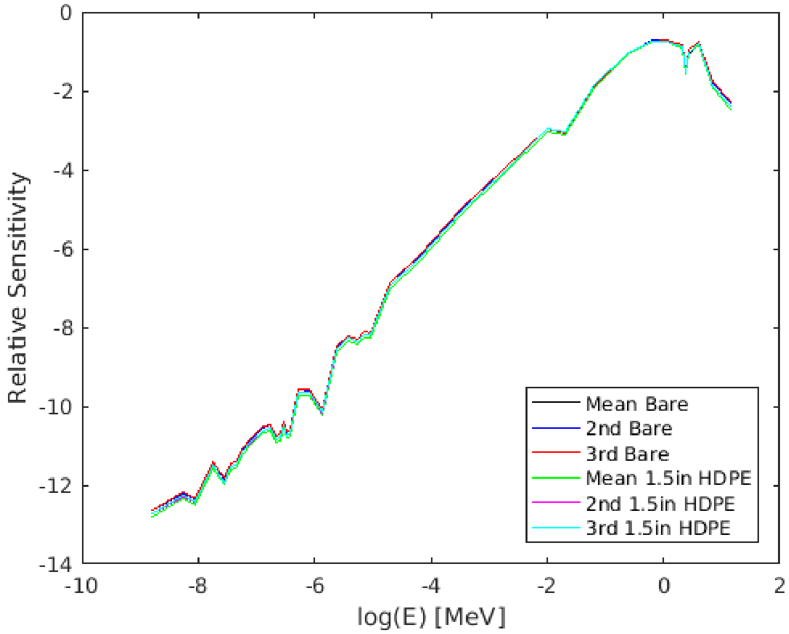

Figure 4.16: Relative sensitivity of spontaneous fission forward source spectrum.

The high energy ratios are due to the large induced fission neutron multiplicity. The ratio around the resonance absorption region is diminished, compared to the bare case, because neutrons can be slowed past this region in the reflector.

Finally, we consider the ratios of the relative sensitivities for each moment between the reflected and bare BeRP ball in Figure 4.19, which are generally small. Beginning with the mean ratio, it is nearly unity across all energies because in an inner product, e.g. a weak sense, the mean relative sensitivity is approximately linear with respect to the forward source. For the second and third moments the bare sphere is most sensitive to the low energy portion of the distribution because the fission cross-section is largest there, where the probability of inducing fission chain-reactions that lead to doubles and triples is greatest. The low energy region is mainly accessed by neutrons being born here because they minimally slow down in the plutonium metal and have to traverse the

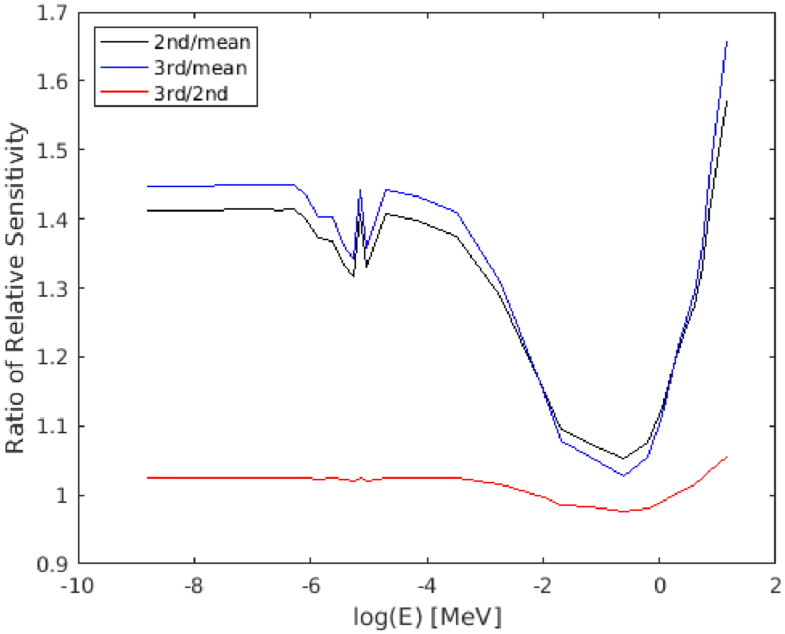

Figure 4.17: Ratio of sensitivities of forward source spectrum between moments for the bare BeRP ball.

resonance absorption region. The bare sensitivities are also larger in the higher energy domain because of the increased neutron multiplicity in this region, that leads to doubles and triples. There is a balancing between fission production verses energy; where the fission cross-section is largest the higher order moments of the induced fission multiplicity are smallest and where the fission cross-section is smallest the multiplicity is largest. Overall, the differences are small, showing that the moment sensitivities, particularly the spontaneous fission multiplicity contribution to the overall neutron multiplicity counting distribution are nearly equally sensitive to the spectrum of the spontaneous fission neutron energy distribution.

Now, that the fission parameters have been discussed, we turn to the other parameters of our model of the neutron multiplicity counting distribution experiment. Next we

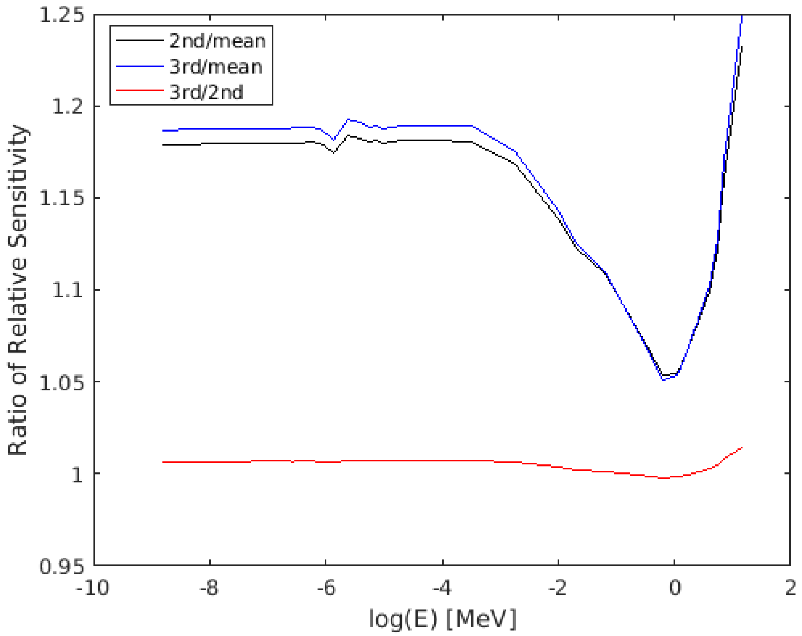

Figure 4.18: Ratio of sensitivities of forward source spectrum between moments for the 1.5in polyethylene reflected BeRP ball.

consider the detector response function because it occurs in the mean adjoint source term.

4.2.4 Detector Response Function

We now address the sensitivity of the nPod detector response function. The detector response function is the foundation of our moment calculations because it is the source term of our mean adjoint equation, to which all higher order moments are coupled. When deriving the sensitivity of the higher order moments we construct the closing equations to link the sensitivities to the mean. The detector response function is unique because it is the only parameter sensitivity determined by inner products with forward quantities, the forward flux and closing fluxes; all other parameters that appear in the transport

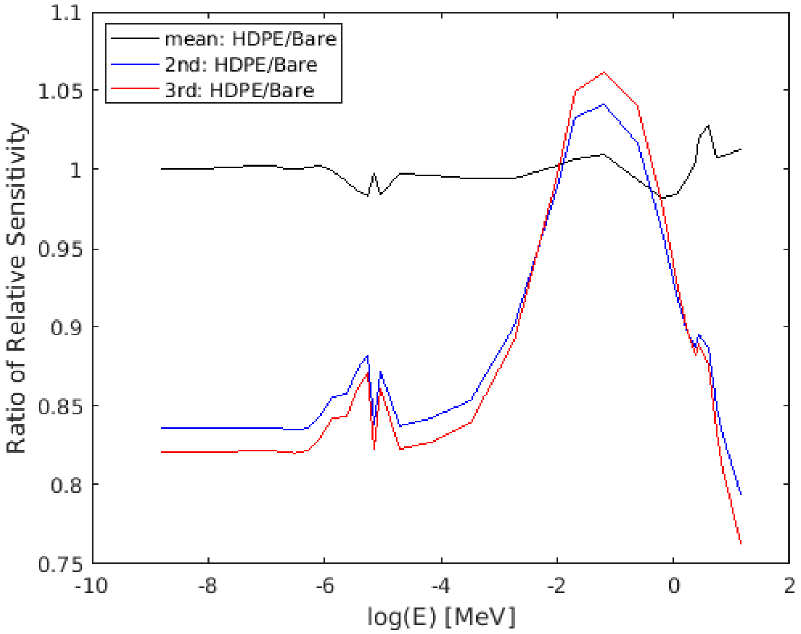

Figure 4.19: Ratio of sensitivities of forward source spectrum for each moment between the reflected to bare BeRP ball.

operators are convolved with combinations of forward and adjoint fluxes. The detector response function is also the only parameter defined as an adjoint boundary source and therefore the sensitivity is determined by a surface integral of leakage currents over the external boundary, recall the continuous Eq. 3.3 and discretized Eq. 3.4 formulations of the mean moment calculation.

The detector response function is defined as the product of the energy-group averaged detection efficiency, Figure 3.6, and the geometric efficiency, which is a function of the thickness of reflector, Table 3.5. The detector has the greatest efficiency above the cadmium cutoff, 2eV, and is insensitive to neutrons below this cutoff. The insensitivity of the nPod to thermal neutrons and the fast spectrum of the bare BeRP ball combine to yield the smallest relative sensitivity coefficient in this work, 10^{-24} which is effectively zero, as seen in Figure 4.20. The addition of reflector softens the leaking spectra, Figure 4.1, into the region where the nPod is most sensitive, between (10 eV, 100 keV), and we notice a much larger sensitivity to slowed leaking neutrons.

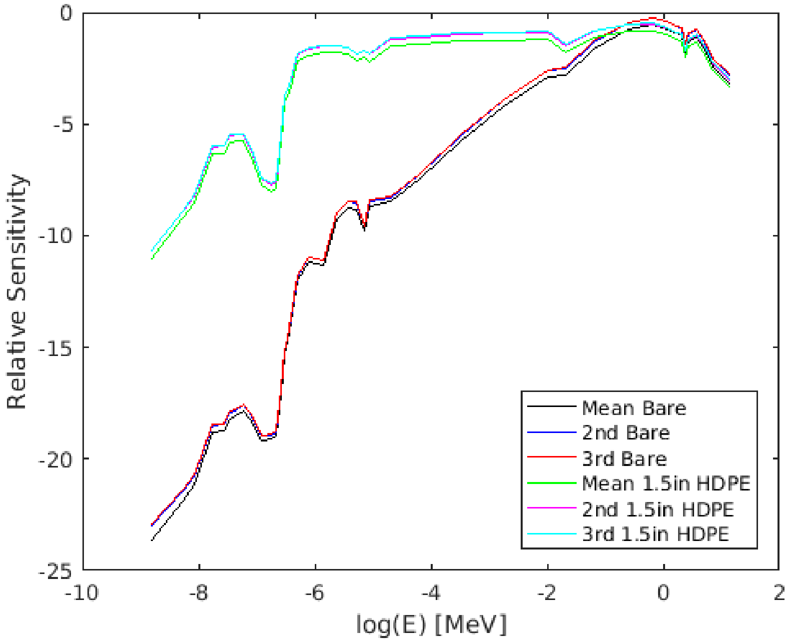

Figure 4.20: Relative sensitivity coefficient of nPod detector response function σ_d across all moments and configurations.

To better appreciate the differences between the moments and degree of reflector, we consider the ratio of the relative sensitivities in Figure 4.21 of the moments of the bare BeRP ball. As expected, the third moment is the most sensitive, followed by the second moment, and the mean, respectively. The high energy sensitivities are influenced by the moments of the induced fission neutron multiplicity distribution, Figure 3.3. The second and third moment sensitivities are closed by the leakage of the closing equations, e.g. Φ_1, Φ_2, and Φ_3, whose source terms are higher order forward fission sources

$(\overline{\nu(\nu-1)(\nu-2)}\sigma_f\psi)$ multiplied by the spatial importance to detection, e.g. I_q.

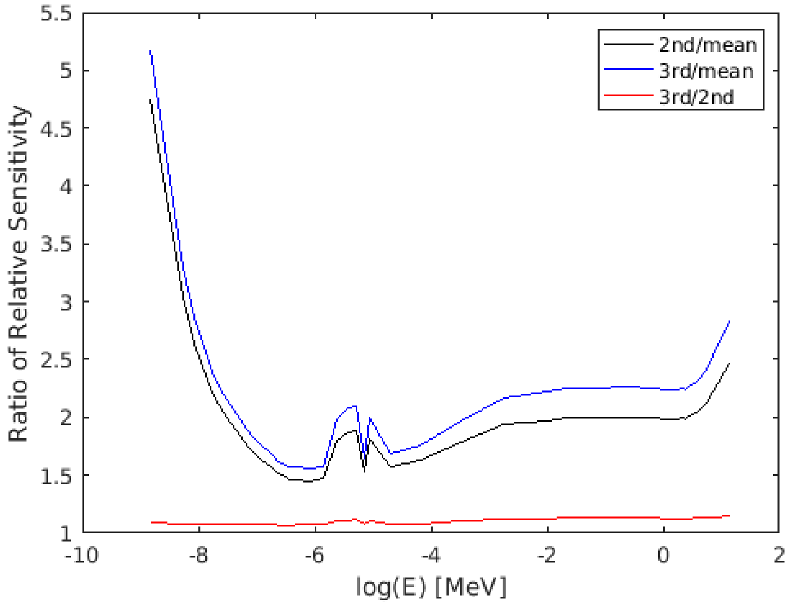

Figure 4.21: Ratio of relative sensitivity of the detector response function for the bare BeRP ball.

An interesting reversal is the presence of the hill and notch around 10 eV that existed for the reflected cases above (Figure 4.4 and Figure 4.8) but now exists for the bare Pu sphere. This switch occurs because we are dealing with a surface term and not Pu core parameters; the notch corresponds to the resonance absorption region in Pu. By the time neutrons have leaked through the polyethylene, the resonance absorption information has been lost. When neutrons leak from the bare BeRP ball, the resonance absorption effect is not moderated. The effect of the reflector smoothing over this absorption feature is evident in the ratio of the 1.5 inch polyethylene reflected relative sensitivity coefficients in Figure 4.22. The smoothing of the spectra of the forward flux is apparent in Figure 4.1;

the sensitivities are dependent on the leakage of the closing equations but these leakage currents are similar to forward flux spectrum.

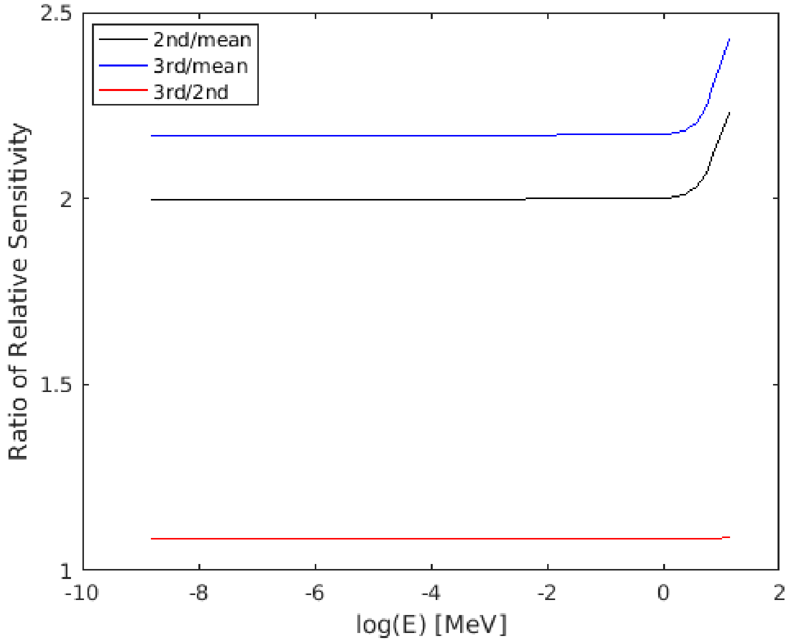

Figure 4.22: Ratio of relative sensitivity of the detector response function for the 1.5in polyethylene BeRP ball.

Lastly, we consider the ratio of reflected to bare for each moment of the multiplicity counting distribution in Figure 4.23. As for the above parameters, the spectral effects dominate, with the largest difference occurring in the thermal regions. The differences in sensitivity about the resonance absorption region manifests as a highly pronounced peak at around 10 eV. The nPod is equally sensitive to fast neutrons across configurations of reflector and across all three moments, because these represent the fission neutrons that either leaked from the bare Pu sphere or streamed, uncollided, through the reflector.

We have considered the collection of energy dependent parameters that are unique to

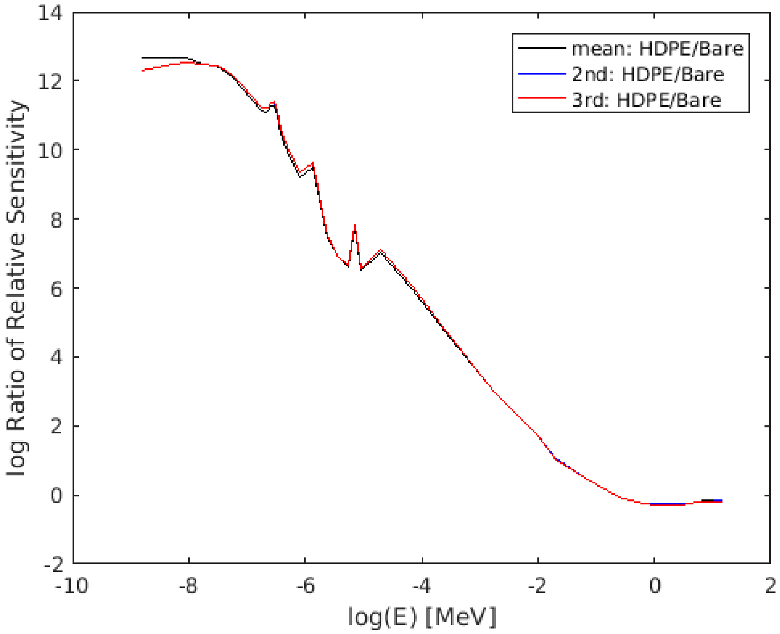

Figure 4.23: Ratios of relative sensitivity coefficients of the detector response function between reflected and bare Pu.

a particular region; the fission parameters exist only in the Pu sphere and the nPod is defined on the boundary. We now consider parameters, such as capture and scattering cross-sections, that exist in the Pu and reflector regions.

4.2.5 Capture Cross-Section

The capture cross-section accounts for neutrons that are absorbed by nuclei that do not lead to fissions, and is a pure loss term in the Boltzmann transport equation. In terms of the other cross-sections, the capture cross-section σ_c is defined as,

$$\begin{aligned}\sigma_c =&\sigma_a - \sigma_f \\ =&\sigma_t - \sigma_f - \sigma_s\end{aligned} \tag{4.5}$$

where we choose to define it in terms of parameters that appear explicitly in the transport operators [37]. The sensitivity of capture cross-section is unique because it is a pure loss term and is the only nuclear parameter, excluding the associated densities of strongly absorbing nuclides, whose sensitivity is always negative. In other words, the moments tend to decrease as σ_c increases.

Plutonium Sphere

Now we consider the relative sensitivity coefficients of the capture cross-section for ^{239}Pu in Figure 4.24. Again we see that the thermal regions are significantly more sensitive given the addition of polyethylene reflector. An interesting feature is that the sensitivity is small around the resonance absorption region because even though the capture cross-section is large because neutrons born here do not contribute to the moments; this is apparent in the adjoint fluxes. As we have come to expect for cross-sections, the magnitude of the sensitivities increases with moment within each state of reflector and the reflected case is generally more sensitive than the bare case.

The ratio of the moment sensitivities of the bare sphere in Figure 4.25 shows the importance of capture competing with induced fission in the lower energies. The higher energy ratios are governed by the large high order moments of the induced fission neutron multiplicity.

The addition of reflector alters the ratio of the moment sensitivities of the capture

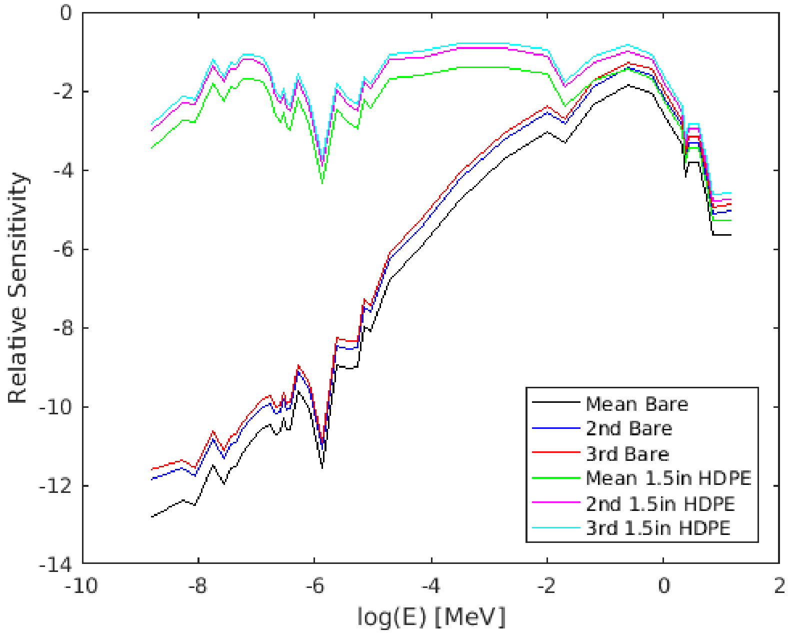

Figure 4.24: Relative sensitivity coefficients of the capture cross-section for ^{239}Pu.

cross-section in Figure 4.26. The thermal regions are no longer as sensitive, especially when comparing the lowest energies of the bare sphere capture cross-section sensitivity ratios. The slowing of neutrons in the reflector means that fission can dominate and capture is not as important in the lowest energies where the fission cross-section is largest. The other notable features are the sensitivity around the resonance absorption region and the high energy being dominated by the neutron multiplicity moments.

Finally, we consider the ratio between the capture sensitivities across the moments between the bare and reflected cases in Figure 4.27. As we have come to expect for cross-sections in the plutonium sphere the principle difference is between the fast and slow energy regimes.

Now we consider the sensitivities to the capture cross-section in the reflector. The ratio of sensitivities in the reflector differ by having no neutron production interactions

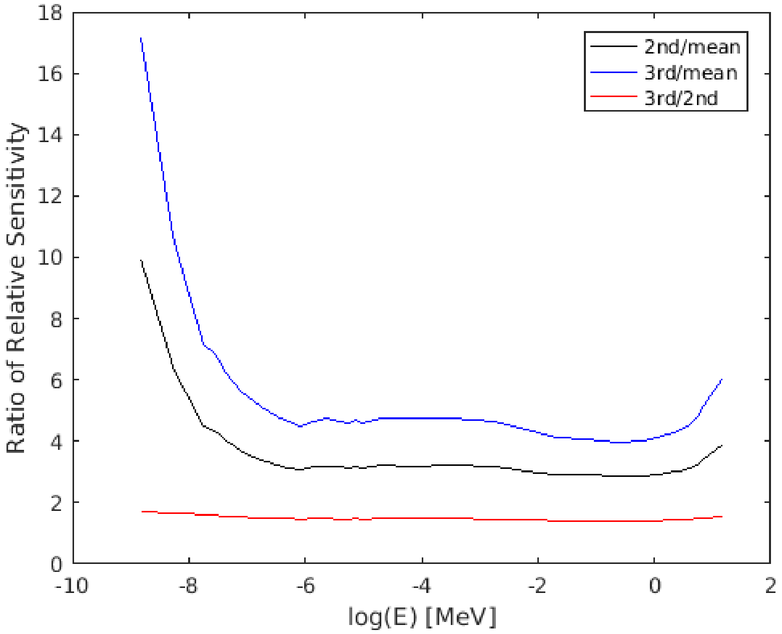

Figure 4.25: Ratio of capture cross-section sensitivities for ^{239}Pu of the bare BeRP ball.

and having zero forward and adjoint source terms.

Polyethylene Reflector

We turn to the relative sensitivity coefficients of the polyethylene reflections and consider the sensitives of the hydrogen capture cross-section and the very small carbon capture cross-section independently. First, we consider the relative sensitivities for hydrogen in Figure 4.28. The sensitivity to neutron capture is largest in the thermal regions as expected, given the shape of the hydrogen capture cross-section and the neutron spectrum in this region.

The ratio of the capture cross-section sensitivities of hydrogen in Figure 4.29 shows interesting features at the energy extremes. First, at high energy there is an increase in sensitivity with each moment that is due to the large fission multiplicity moments.

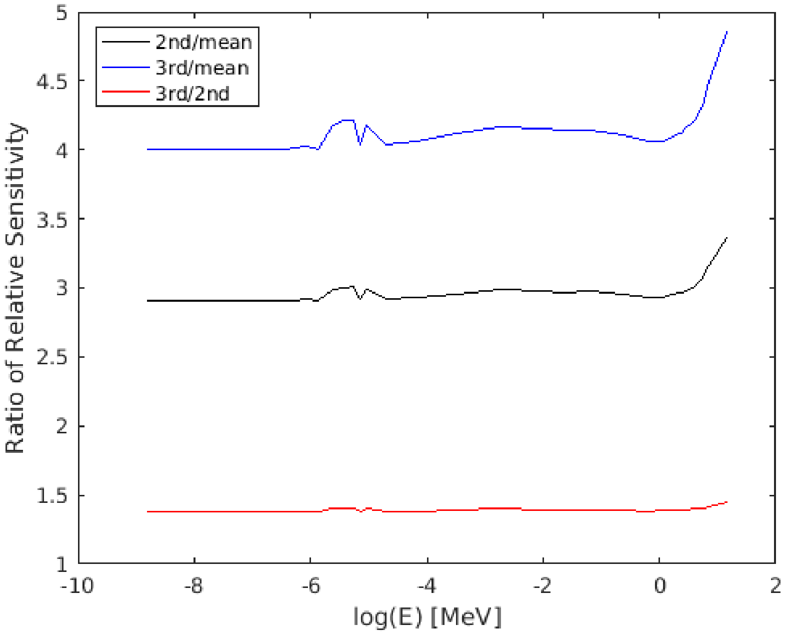

Figure 4.26: Ratio of capture cross-section sensitivities for ^{239}Pu of the reflected BeRP ball.

In the low energies there is the decreased multiplicity moment but an increase in the probability of induced fission. In between the extremes, there is a trough where the induced fission probability is low and the multiplicity is also small. So, in the reflector we see a balance between capturing a fast or slow neutron. There is a trade off in the higher order moments between slowing a neutron to the low multiplicity but high fission probability and reflecting a fast neutron to induce a high multiplicity event but with a lower fission probability.

The capture cross-section sensitivity for carbon is noticeably different in magnitude and in the high energy range when compared to hydrogen, as seen in Figure 4.30. The spike in high and low energy sensitivity is due to the balance between the capture and scattering cross-section. Carbon is effective at slowing neutrons in the higher and lower

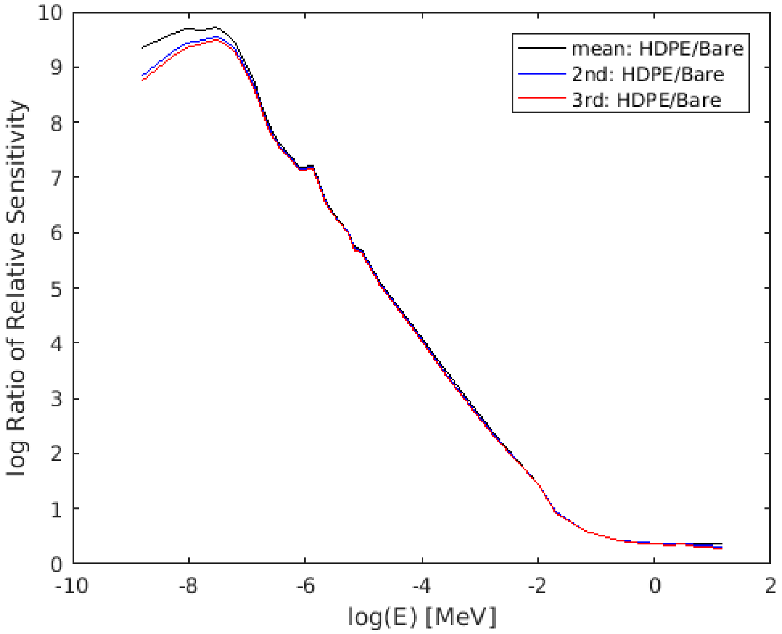

Figure 4.27: Ratio of capture cross-section sensitivities for ${}^{239}Pu$ between the reflected and bare BeRP ball.

energies, meaning that neutrons captured here had the potential to induce fissions. The trough in the sensitivity is due to the small capture cross-section and that neutrons are significantly slowed in this region.

In the ratio, it is interesting to note that even with noticeably different high energy features compared to hydrogen, the ratio of the carbon moment sensitivities in Figure 4.31 is nearly the same shape as the hydrogen ratio Figure 4.29. As with all the higher order moments, the excess is caused by fission chain-reactions and therefore even in non-multiplying regions the physics of fission dominate.

The last energy dependent parameter we consider is the scattering cross-section.

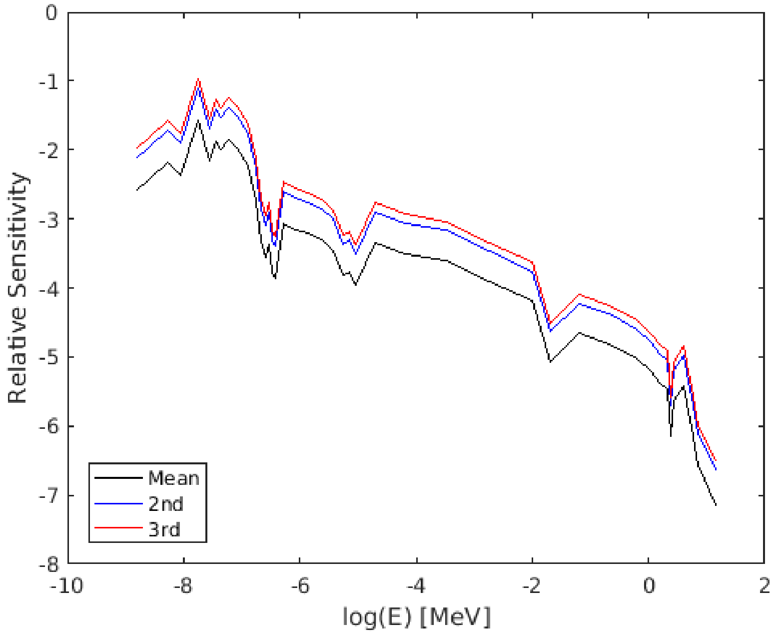

Figure 4.28: Relative sensitivities of the capture cross-section for ^1H.

4.2.6 Scattering Cross-Sections

The scattering cross-section is the final energy dependent parameter we consider. In this section we consider the sensitivity to the self-scatter cross-section. The full energy differential scattering cross-sections can be found in chap:ScatSens. We present the relative sensitivities only because the ratios are nearly the same as the capture cross-section.

First, we consider the sensitives of hydrogen in Figure 4.32. The principle feature to note is the large relative sensitivities that are greater than one (zero on the logarithm scale). These differences show that there is a strong competition between capture and the neutron surviving to either induce a fission or be detected.

The same features are present in the scattering cross-section relative sensitivities for carbon in Figure 4.33. The carbon sensitivity is much smaller than hydrogen and

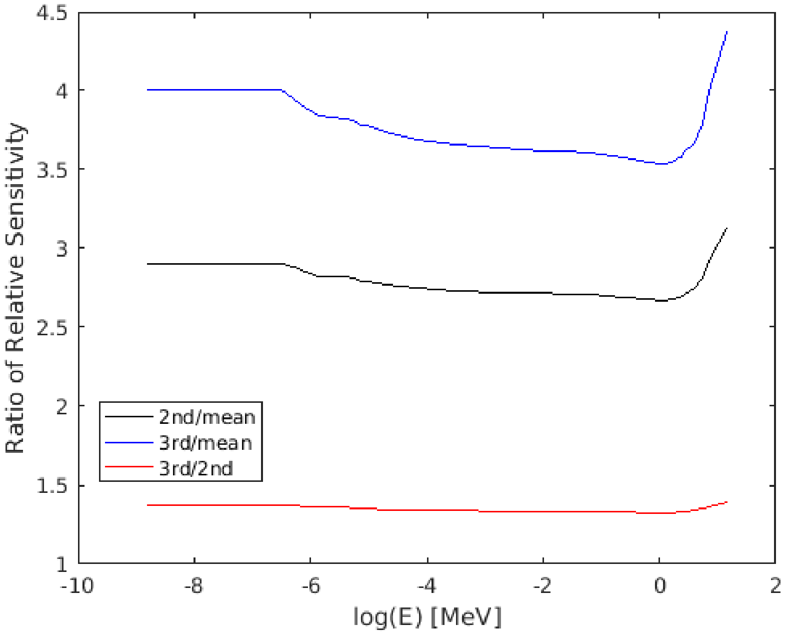

Figure 4.29: Ratio of capture cross-section sensitivities for ^1H.

noticeably so in the thermal regions, as the decrease is not just in scale. In the lower energies there is minimal competition with capture.

Finally, we see how the self-scatter cross-section of ^{239}Pu is affected by the addition of reflector in Figure 4.34. As expected the self-scatter cross-section sensitivity increases dramatically with the addition of reflector in the thermal regions because prior to the addition of polyethylene, the slow neutron population was negligible.

Now that the energy dependent parameters have been considered, we turn to the sensitivity of the scalar parameters of the neutron multiplicity counting distribution moment equations.

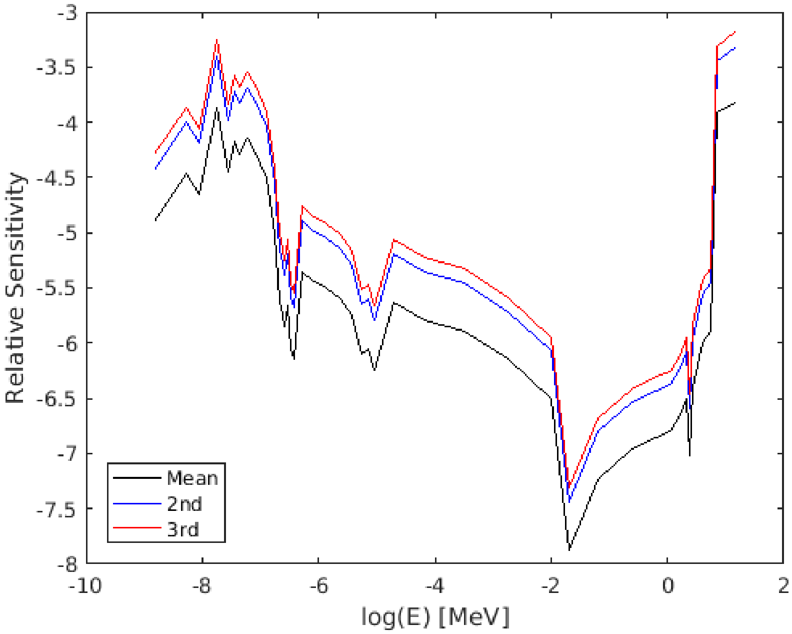

Figure 4.30: Relative sensitivities of the capture cross-section for ^{12}C.

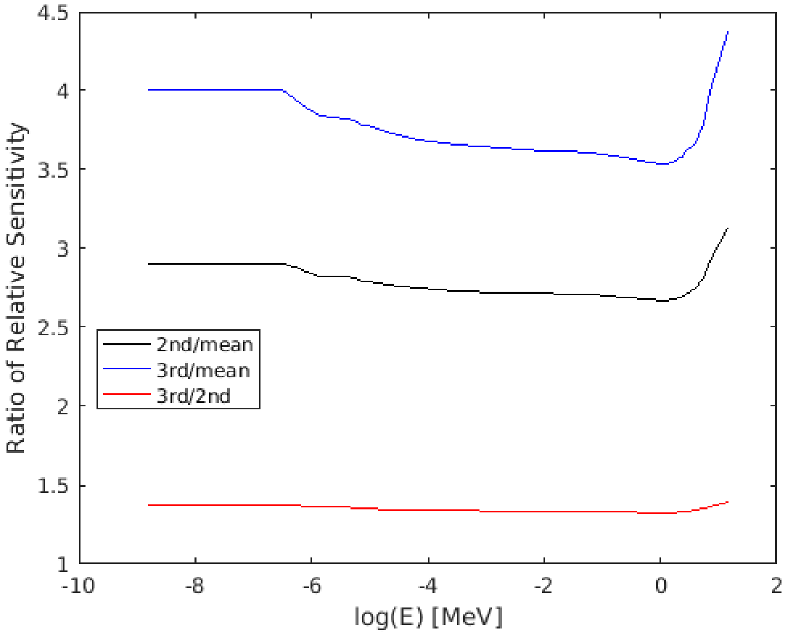

Figure 4.31: Ratio of capture cross-section sensitivities for ^{12}C.

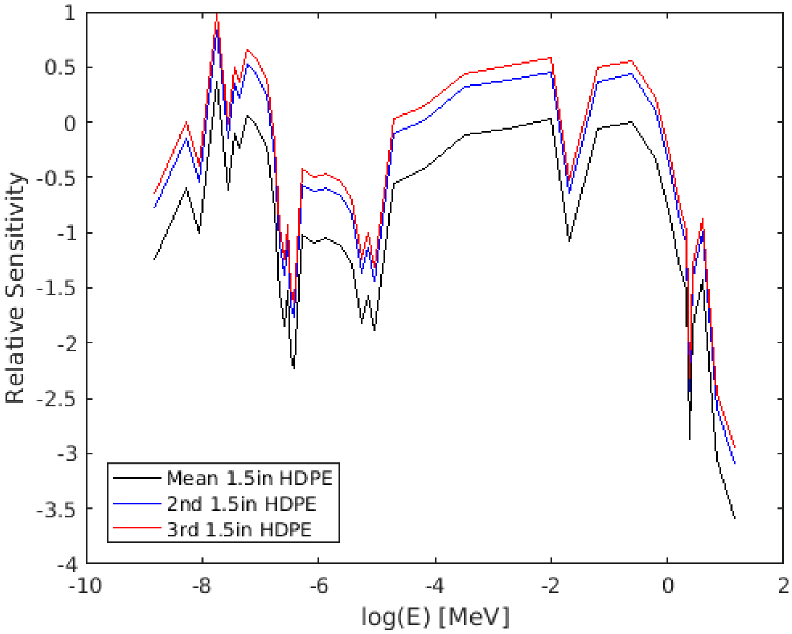

Figure 4.32: Relative sensitives of self scatter cross-section of ^{1}H.

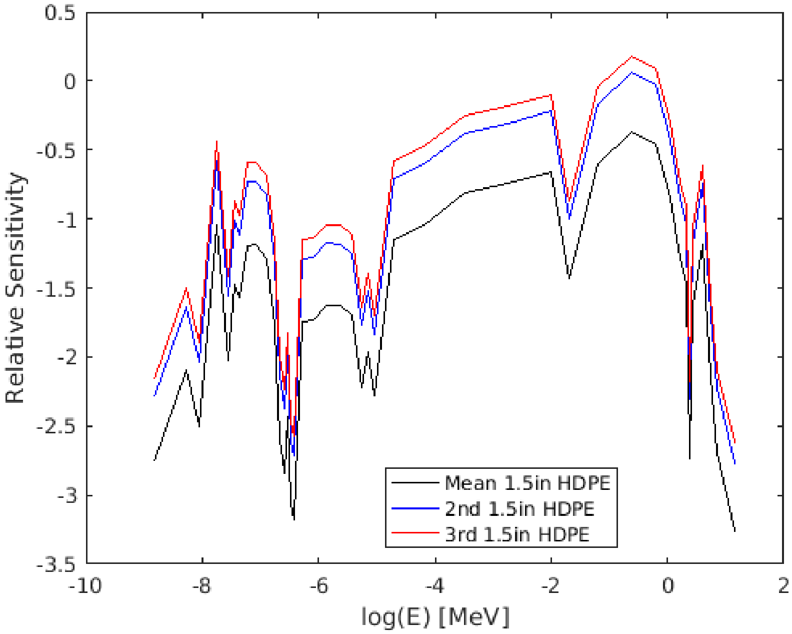

Figure 4.33: Relative sensitives of self scatter cross-section of ^{12}C.

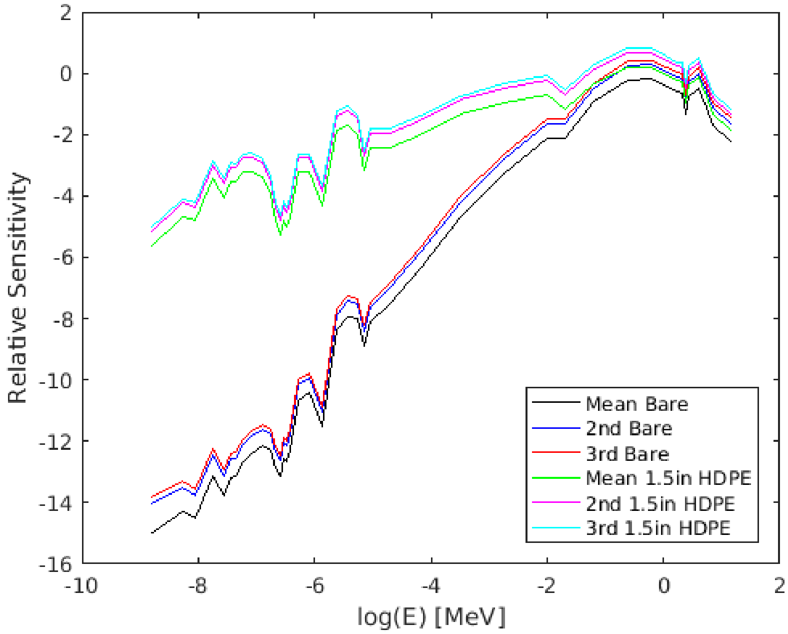

Figure 4.34: Relative sensitives of self scatter cross-section of ^{239}Pu.

4.2.7 Scalar Parameter Sensitivities

We consider the relative sensitivity coefficients of scalar parameters of our system. The scalar sensitivities are considered for each moment, allowing us to compare the effects of the addition of reflector. The scalar parameters we consider are the geometric efficiency of the nPod detector, the moments of the spontaneous fission source neutron multiplicity, and the nuclide densities.

The relative sensitivities of the mean provide the baseline of comparison for the higher order moment excess sensitivities as seen in Table 4.2. Working our way down from the top of the table, we see that the geometric efficiency of the nPod and the average number of spontaneous fission neutrons are effectively unity for both the bare and reflected BeRP ball because the mean adjoint and forward transport equations are linear. The small deviation from unity arises from our averaging of the two ways of computing the mean,

$$\begin{aligned} R_1 =& \frac{\langle \sigma_d, \psi \ \rangle + \left\langle \psi_1^\dagger, Q \right\rangle}{2} \\ =& \frac{\epsilon_{geo} \left\langle \epsilon(E), \psi \ \right\rangle + \overline{\nu_s} \left\langle \psi_1^\dagger, S \right\rangle}{2} \end{aligned} \tag{4.6}$$

and noting that the mean is linear in these parameters as well. We average the two moment calculations to not bias our calculations but the largest relative error between the two moment calculations is about 0.01%.

The next quantities are the nuclide densities. As expected the mean is most sensitive to the density of the multiplying medium ^{239}Pu in both cases. The sensitivity increases with the reflected case because of the increase in neutron multiplication. The sensitivity to the density of the spontaneous fission medium ^{240}Pu is nearly unity in both cases because its main contribution to the mean is in the overall strength of the source, in addition to the negligible induced fission contribution. A surprising result is the negative relative sensitivity of the hydrogen density, indicating that there can be too much moderation. Neutrons that leave the reflected sphere below the cadmium cut-off energy of about 2 eV are not detected by the nPod. We can see the effect of adding additional polyethylene in Figure 3.8, where the mean for the 6 inch polyethylene case, which has the largest neutron multiplication, is even less than the bare mean. We would expect the relative sensitivity to hydrogen density to be positive for thicknesses of polyethylene below 1.5 inch. It would be interesting to find the point of zero sensitivity of hydrogen density with respect to thickness of polyethylene. The last parameter considered is the density of carbon, which unlike hydrogen, is positive because it is does not slow neutrons into the unresponsive detector regions.

Table 4.2: Mean relative sensitivity coefficients for scalar variables, for bare BeRP ball and 1.5in polyethylene.

α	Bare S_{rel}	1.5 in polyethylene S_{rel}
ϵ_{geo}	1.0000003515	1.0007255442
$\overline{\nu_s}$	0.9999996485	0.9992744558
ρ_{239Pu}	2.02677758166	4.94321134895
ρ_{240Pu}	1.01809156892	1.00790548475
ρ_{1H}	—	-0.118531344268
ρ_{12C}	—	0.0102496605879

The second moment scalar sensitivities are given in Table 4.3. Again, working from top to bottom, we observe that the second moment is still linearly sensitive to the geometric detection efficiency but the linearity is lost for the average multiplicity of the spontaneous fission source. This loss of linearity is due to the new second moment excess

R_2 being the sum of two inner products, which we could write as,

$$\begin{aligned} R_2 &= \left\langle \overline{\nu(\nu-1)}\sigma_f I_1^2, \psi \right\rangle + \left\langle \overline{\nu_s(\nu_s-1)} I_{s,1}^2, S \right\rangle \\ &= \left\langle \psi_2^\dagger, \overline{\nu_s} S \right\rangle + \left\langle \overline{\nu_s(\nu_s-1)} I_{s,1}^2, S \right\rangle \\ &= \overline{\nu_s} \left\langle \psi_2^\dagger, S \right\rangle + \overline{\nu_s(\nu_s-1)} \left\langle I_{s,1}^2, S \right\rangle \end{aligned} \tag{4.7}$$

We do note that the sum of relative sensitivities of $\overline{\nu_s}$ and $\overline{\nu_s(\nu_s-1)}$ sum to unity, for both cases, preserving the total linearity of the moment excess. For the remaining densities the sensitivity increases with addition of reflector and relative to the mean. The density of ^{240}Pu increases with the moments but is smaller in the reflected case because of the increase in neutron multiplication.

Table 4.3: Second moment relative sensitivity coefficients for scalar variables, for bare BeRP ball and 1.5in polyethylene.

α	Bare S_{rel}	1.5in polyethylene S_{rel}
ϵ_{geo}	1.0000987819	1.0024044353
$\overline{\nu_s}$	0.838139261	0.9240101809
$\overline{\nu_s(\nu_s-1)}$	0.1619751545	0.0752547083
ρ_{239Pu}	6.84742696472	15.517614473
ρ_{240Pu}	1.05043046125	1.02531947217
ρ_{1H}	—	-0.102359264186
ρ_{12C}	—	0.0308674271947

The third moment scalar sensitivities all increase with respect to their lower order values as seen in Table 4.4. Again, the sum of the spontaneous fission source multiplicity moments maintain their linearity. There is a marked increase, nearly doubling, in the sensitivity of the nPod geometric efficiency for both cases of reflector. This increase is due to the two orders of coupling between the third moment and the mean, mediated by the closing equations. The final notable change is that the hydrogen sensitivity is now positive meaning that the benefits of additional moderation, that leads to fission chain-reactions, outweighs the losses due to the slowing of neutrons into the insensitive energy regions of the nPod detector.

Table 4.4: Third moment relative sensitivity coefficients for scalar variables, for bare BeRP ball and 1.5in polyethylene.

α	Bare S_{rel}	1.5in polyethylene S_{rel}
ϵ_{geo}	1.9308214972	2.0282259856
$\overline{\nu_s}$	0.8381794629	0.9252830323
$\overline{\nu_s(\nu_s-1)}$	0.1535651079	0.0724288252
$\overline{\nu_s(\nu_s-1)(\nu_s-2)}$	0.0084100466	0.0015718353
ρ_{239Pu}	10.3465240971	22.1573053857
ρ_{240Pu}	1.06958870936	1.03552436606
ρ_{1H}	—	0.00727388023
ρ_{12C}	—	0.0428647135088

Now that we have finished discussing the scalar parameters, it is useful to turn to the energy dependent sensitivities into scalar quantities in order to more readily identify their importance to the moments of the neutron multiplicity counting distribution. We also include some of the already scalar parameters in this energy integrated treatment for the ease of direct comparison.

4.3 Energy Collapsed Relative Sensitivity Coefficients

Finally, we energy collapse the relative sensitivities of the most influential parameters and rank them. We collapse the energy dependent sensitivities by integrating the absolute sensitivities over energy and then multiplying them by the energy averaged parameter over the moment, recalling Eq. 4.3,

$$\overline{S_{q,\alpha}} = \frac{\overline{\alpha}}{R_q} \sum_g \frac{\partial R_q}{\partial \alpha_g} \tag{4.8}$$

We find that the moments are most sensitive to the fission parameters and that the sensitivities generally increase with the order of the moment and with the addition of reflector.

We consider the collapsed sensitivities of mean for the bare BeRP ball first, in Figure 4.35. As we would expect the system is most sensitive the average multiplicity of induced fission $\overline{\nu}$ and followed by the fission cross-section. The system is sensitive to the scatter cross-section because it balances slowing down (leading to neutron production) and capture (leading to neutron loss). The sensitivity to the average forward source Q is unity because the transport equation is linear. Finally we see that the energy dependent detection efficiency is not unity, it is not a scalar parameter like the geometric efficiency.

We contrast the bare case to the reflected mean collapsed sensitivities in Figure 4.36. The principle difference is the significant increase in the fission parameter sensitivity, which is due to the sensitivities in the slow regions no longer being negligibly small. The system is more sensitive to carbon because it does not slow neutrons into the insensitive region of the detector, below the cadmium cutoff.

The second moment bare sensitivities increase compared to the mean as seen in Figure 4.37. The most notable change is the fission cross-section becoming the most sensitive

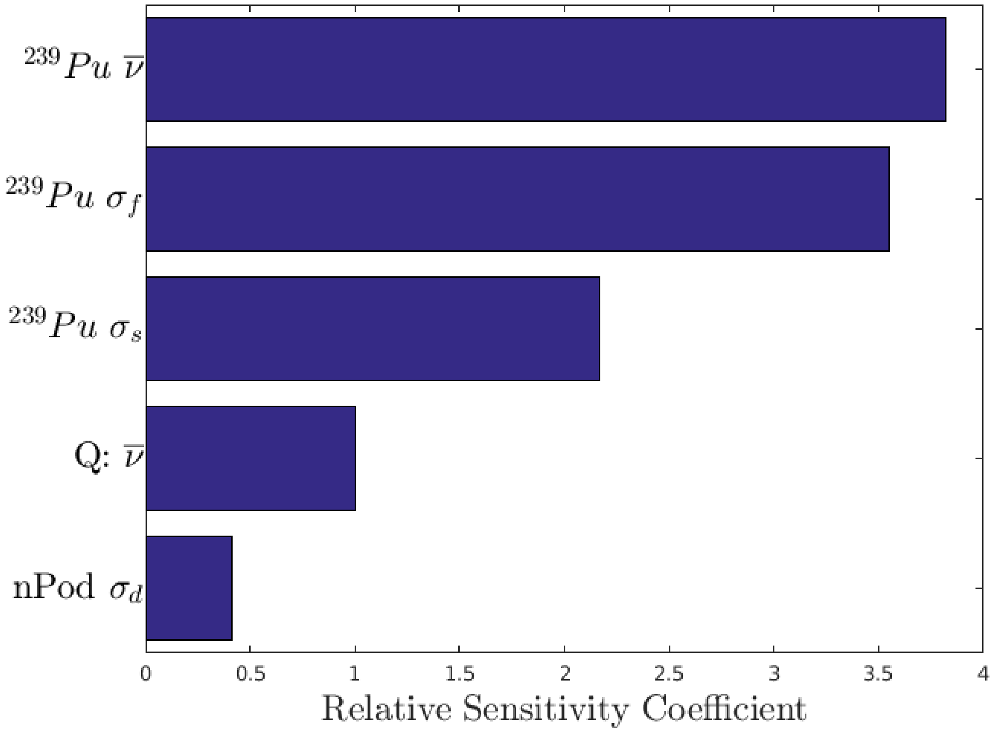

Figure 4.35: Ranked influential group collapsed mean relative sensitivity coefficients of the bare BeRP ball.

parameter, instead of the average neutron multiplicity. The fission cross-section now appears in both transport operators and in the source terms of the second adjoint and the first closing equations. However, if we considered the sensitivity of the multiplicity distribution, thereby including the sensitivity contributions of $\overline{\nu(\nu-1)}$, it would likely be the most sensitive set of parameters. We do not consider the probabilities $p_\nu(E)$ as a direct sensitivity analysis parameters due to issues with studying perturbations of a distribution, which by definition must integrate to unity.

For the reflected case the average multiplicity is the largest parameter sensitivity in Figure 4.38 because of the increase in multiplication and increased importance of slow

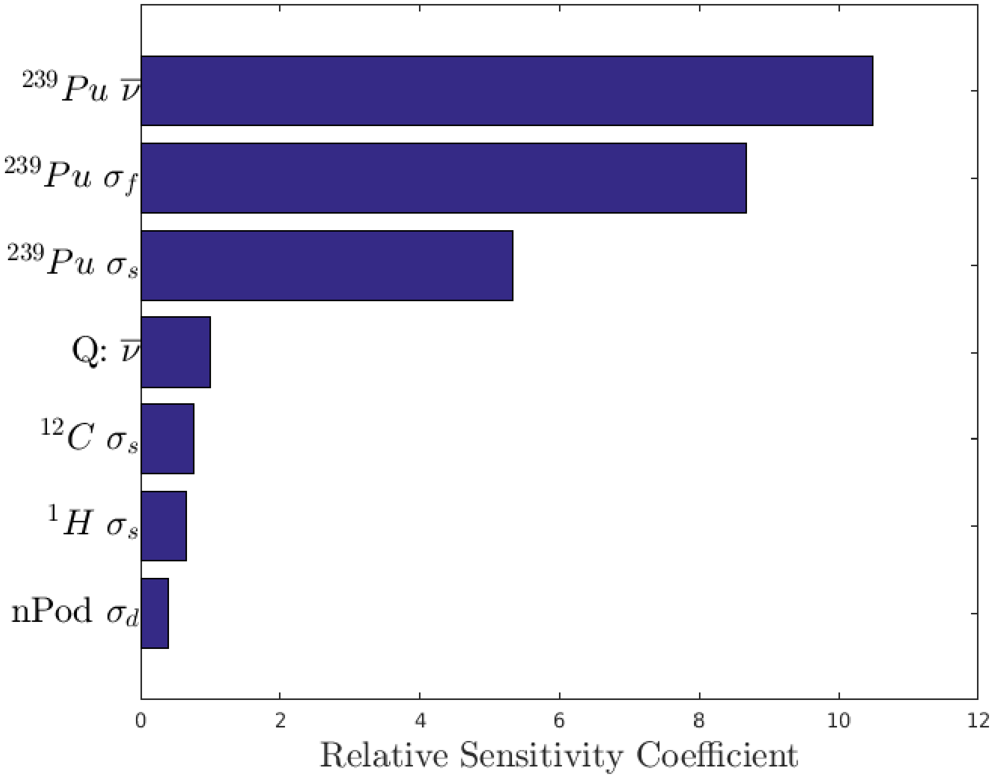

Figure 4.36: Ranked influential group collapsed mean relative sensitivity coefficients of the reflected BeRP ball.

neutron induced fissions. Now both fast fission, which generates more neutrons, and slow fission, which is more likely but has lower multiplicity, occur in the BeRP ball. We do notice that the second factorial moment sensitivity of the induced fission multiplicity is about the same between the bare and reflected BeRP ball, because $\overline{\nu(\nu-1)}$ is largest for high energy inducing neutrons.

Now we consider the third moment group collapsed relative sensitivity coefficients of the the bare BeRP ball in Figure 4.39. It is apparent that all the higher order moments are most sensitive to the induced fission parameters, as these of course are responsible for the

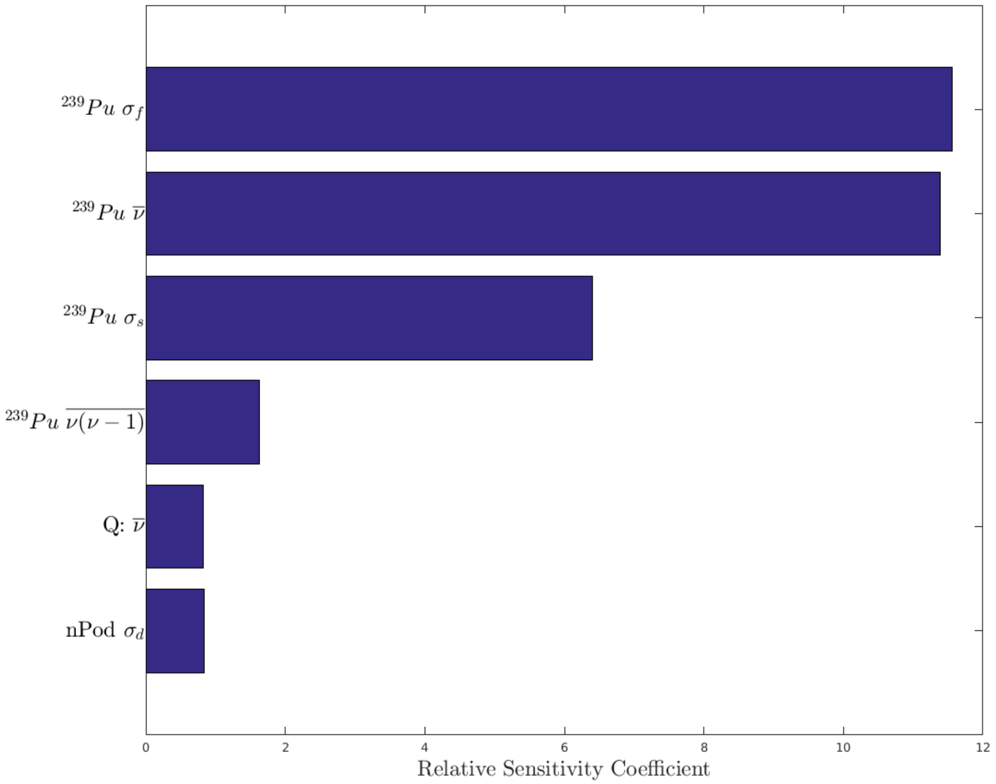

Figure 4.37: Ranked influential group collapsed second moment relative sensitivity coefficients of the bare BeRP ball.

excess to the Poisson moments of non-multiplying systems. The self-scatter cross-section is important, though it is not directly tied to fission, because it is part of the balance between capture and absorption that leads to fission. Parameters not related to induced fission are generally the same across the moments and configurations of reflector. The forward and adjoint sources collapsed sensitivities are about equal to one, these energy collapsed source terms now behave as a scalar source to a linear equation. The deviations from unity are due to the separation of the moment excess due to induced fission and from the contributions of the spontaneous fission multiplicity.

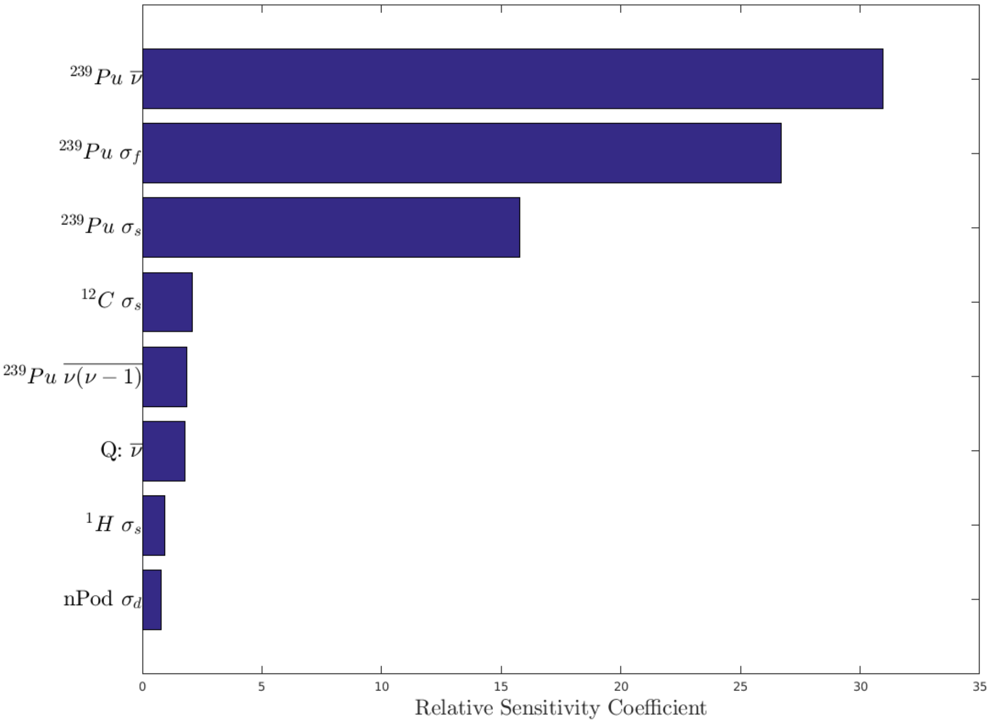

Figure 4.38: Ranked influential group collapsed second moment relative sensitivity coefficients of the reflected BeRP ball.

The third moment collapsed sensitivities of the reflected BeRP ball are seen in Figure 4.40. There is a significant increase in the collapsed sensitivities in the fission parameters. As occurred in the lower order moment sensitivities, the addition of reflector makes the negligible small slow fission sensitivities become significant. Given that about half of our 44-group energy structure accounts for energies below 1 eV, this means that the nearly the majority of our group-wise sensitivity coefficients are insignificant in the bare plutonium sphere case. The reflector parameters and source term sensitivities are effectively the same between the cases of reflector and the moments. Again, these parameters form the foundation, the mean forward and first adjoint equations, of our sequential

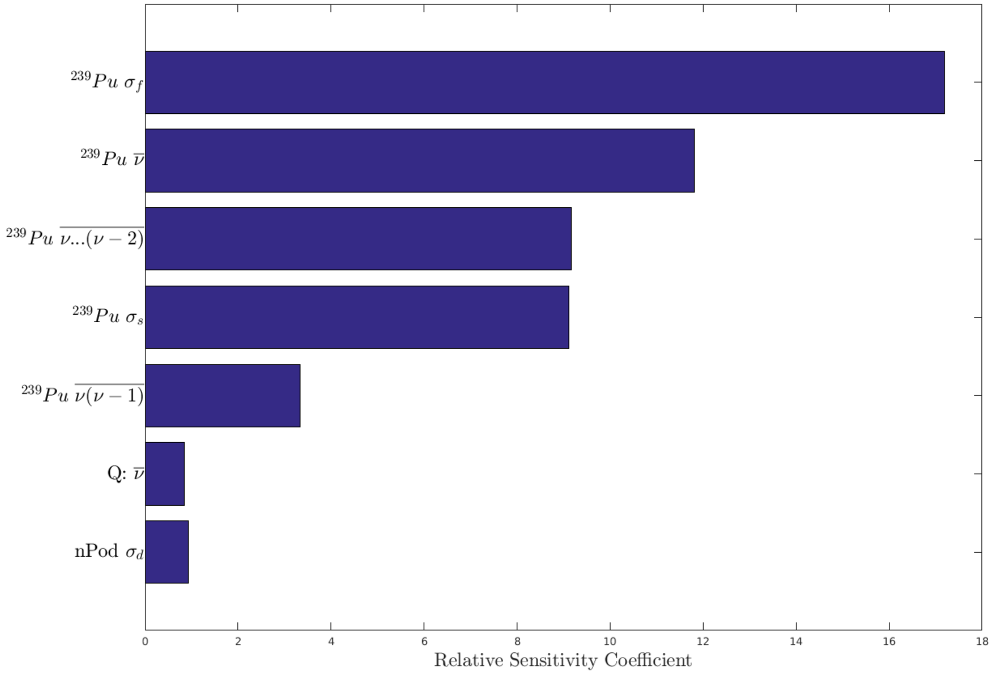

Figure 4.39: Ranked influential group collapsed third moment relative sensitivity coefficients of the bare BeRP ball.

moment calculations and sensitivity analysis closing equations. These base source parameters, when group collapsed behave as linear source terms because they are fixed and do not reappear in the operators nor the higher order adjoint sources.

4.4 Conclusion

We have performed a complete sensitivity analysis of the first three moment excesses of the neutron multiplicity counting distribution for the bare BeRP ball and the case of 1.5 inch of polyethylene reflector. The relative sensitivity coefficients of the energy dependent parameters were considered first and we found that, as anticipated, the moment

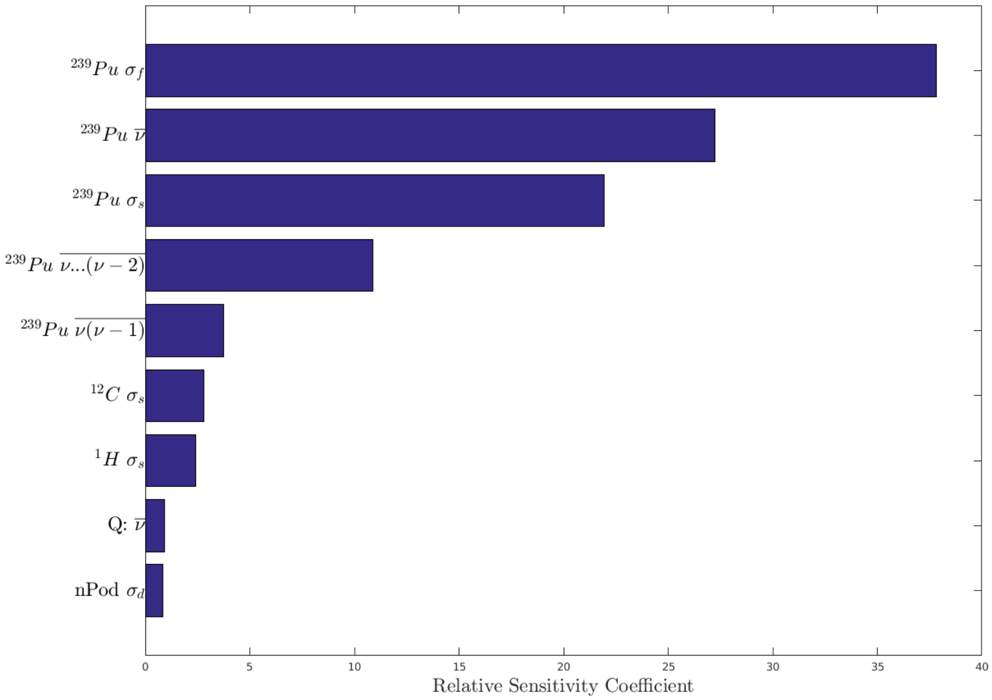

Figure 4.40: Ranked influential group collapsed third moment relative sensitivity coefficients of the reflected BeRP ball.

excesses are most sensitive to the fission parameters. The sensitivities increased with increasing moment and with the addition of polyethylene, as the reflector slows neutrons down past the resonance absorption region where the fission cross-section is large. We examined the ratio between sensitivities to reveal what physical processes governed the growth between moments and reflectors. Most ratios of sensitivities revealed increased sensitivities around the increased fission cross-section at low energies, the losses due to the resonance absorption at middle energies, and the increased fission neutron multiplicity at high energy. We found that the addition of a reflector leads to a trade off between the detector efficiency sensitivity and thermal fissions, because slower neutrons induce more fissions but the nPod detector is insensitive to neutrons below 2 eV.

Next, we considered the scalar parameter relative sensitivities. The scalar source term sensitivities, such as the geometric efficiency, are nearly unity because of the linear transport and moment inner product equations. For the higher order moments the sum of spontaneous fission source moment multiplicities ($\overline{\nu_s}$, ..., $\overline{\nu_s(\nu_s-1)(\nu_s-2)}$) were found to be near unity, as the sum of the moment excess contributions is linear. The sensitivity to the density of ^{240}Pu is also near unity for all cases, as its principle contribution to the moments is in the magnitude of the spontaneous fission source. For all the moments and cases the most sensitive scalar term is the density of the multiplying medium, ^{239}Pu. A surprising result was that sensitivity to the hydrogen density was negative for all the moments, apart from the third, because too much hydrogen can slow leaking neutrons into the insensitive detector regions.

Finally, we averaged the energy dependent parameters and integrated the sensitivity coefficients over all energy to yield an energy collapsed relative sensitivity coefficient, effectively allowing us to study a one-group sensitivity analysis of our experiment. As we expected, the collapsed sensitivities grew with each moment and with the addition of reflector because the slow sensitivities are negligible in the bare sphere case. The system is most sensitive to the fission cross-section and moments of the induced fission neutron multiplicity distribution.

Now that we have completed a thorough sensitivity analysis for all our model parameters, for the bare and reflected cases, and for the first three moments, we seek the range of validity of our first-order perturbation approximation. In the following chapter we measure the first-order truncation error by comparing the moments of direct transport solutions using perturbed parameters to the predictions of our first-order sensitivity analysis.

Chapter 5

First-Order Perturbation Truncation Error

5.1 Introduction

We have determined the sensitivities of the parameters of the bare and 1.5 inch reflected BeRP ball for the first three moments of the neutron multiplicity counting distribution. To test the range of validity of our coupled sensitivity analysis, we consider the first-order truncation error by comparing the moments of a perturbed system estimated by our first-order SA approximation and an explicit transport solve. We consider our first-order theory to be successful if the relative truncation error is less than the relative parameter perturbation. We tabulate the truncation error passing rate and find that all parameters for both reflector configurations have a passing rate greater than $\approx 87\%$ for all moments. For each configuration we examine the fission cross-section, a representative highly sensitive parameter, versus error and show that the truncation error trends with the magnitude of the relative sensitivity coefficient.

5.2 Truncation Error Calculation

In order to establish the validity of our first-order approximation, we calculate the series truncation error. In Eq. 2.43 we defined the first-order approximation but the exact perturbation equation is,

$$R_q(\alpha_0 + \delta\alpha) = R_q(\alpha_0) + \left.\frac{\partial R_q}{\partial \alpha}\right|_{\alpha=\alpha_0} \delta\alpha + \sum_{n=2}^{\infty} \left.\frac{\partial^n R_q}{\partial \alpha^n}\right|_{\alpha=\alpha_0} \frac{\delta\alpha^n}{n!} \tag{5.1}$$

where the truncated terms for each moment are contained in the summation on the right. We consider the absolute relative truncation error in our analysis because parameters and moments vary greatly in magnitude. We define the relative truncation error as,

$$e(\delta\alpha) = \left| 1 - \frac{R_q(\alpha_0) + \left.\frac{\partial R_q}{\partial \alpha}\right|_{\alpha=\alpha_0} \delta\alpha}{R_q(\alpha_0 + \delta\alpha)} \right| \tag{5.2}$$

To arrive at the truncation error, we independently perturb each parameter by a fraction f. In this work we consider maximum fractions of plus/minus ten percent, $f = [-0.1, 0.1]$. The perturbed parameter is given in terms of f,

$$\alpha + \delta\alpha = (1 + f)\alpha \tag{5.3}$$

where by definition, the relative perturbation in the parameter is f. The exact points of perturbation we studied were, in terms of percentage,

$$\begin{aligned} f =& [-10.0, -9.0, -7.0, -5.0, -2.5, -1.0, -0.5, -0.1, -.05, 0.0 \\ &, 0.05, 0.1, 0.5, 1.0, 2.5, 5.0, 7.0, 9.0, 10.0]\% \end{aligned} \tag{5.4}$$

We determine the relative truncation error by,

1. Solving the first three moment equations for α
2. Forming the sensitivity coefficients at α
3. Using the sensitivity to find the new moments given the fractional perturbation f
4. Solving the first three moment equations using a perturbed α
5. Comparing the first-order approximation to the perturbed deterministic solutions

We use the same spatial discretization and order of angular quadrature, for each moment and sensitivity calculation. We only change a single parameter at a time and by the linear nature of the transport operator we can say that the error of multiply perturbed parameters is the sum of the errors of those parameters perturbed individually. If the relative truncation error e of a parameter is less than the degree of perturbation f, we say that first-order perturbation theory is sufficient, e.g. if,

$$\begin{aligned} e(\delta\alpha) &< |f| \\ &< \left|\frac{\delta\alpha}{\alpha}\right| \end{aligned} \tag{5.5}$$

We plot the error as a function of a parameter over all energies and the range of perturbations f. We also report the fraction of perturbations which pass our metric.

In order to efficiently survey the perturbation error space we make several simplifications/reductions to our transport model and parameters, that enabled us to explore our parameters using only 5×10^4 forward/adjoint deterministic transport solves. First, we used fewer spatial cells than the core of our work, as we are not overly concerned with the accuracy of our moments with experiment but rather relative differences in the calculation of the moments. The order of angular quadrature S_{32} did not change but we considered only isotropic scattering because we did not perturb the higher order Legendre scattering coefficients. The higher order scattering moments were omitted due to file write times when rebuilding the cross-section library for each set of moment calculations. However, scattering is forward peaked in high-A media, e.g. plutonium.

We formed our cross-sections from the nuclides in our model and perturbed the result, e.g. when we perturb the scattering cross-section in the reflector, we perturb the result of adding the macroscopic cross-sections of carbon and hydrogen. When the fission and scatter cross-sections are perturbed, we enforce balanced cross-sections by adjusting the total cross-section in the cross-section library. We also account for the associated perturbation via the total cross-section sensitivity coefficient, e.g. for the fission cross-section,

$$R_q(\sigma_f + \delta\sigma_f) \approx R_q(\sigma_f) + \left(\left.\frac{\partial R_q}{\partial \sigma_f}\right|_{\sigma_f} + \left.\frac{\partial R_q}{\partial \sigma_t}\right|_{\sigma_t} \right) \delta\sigma_f \tag{5.6}$$

Finally, we do not perturb scalar quantities as the transport equation is linear and we do not perturb the terms that makeup a parameter, e.g. for the forward source $Q = \overline{\nu_s}\chi_s S_0$ we perturb the bulk of $Q(E)$, not $\overline{\nu_s}$, χ_s, or S_0 individually.

The parameters we directly perturb, for the bare and reflected cases are,

- Detector efficiency: σ_d
- Mean forward source: $Q = \overline{\nu_s}S$
- Fission cross-section: $\sigma_f = \rho_{239Pu}\sigma_{239Pu,f}$

- Average induced fission neutron multiplicity: $\overline{\nu}$
- Second moment of the induced fission neutron multiplicity of ^{239}Pu: $\overline{\nu(\nu-1)}$
- Third moment of the induced fission neutron multiplicity of ^{239}Pu: $\overline{\nu(\nu-1)(\nu-2)}$
- P_0 self-scattering cross-section in Pu: $\sigma_{Pu,s} = \rho_{239Pu}\sigma_{239Pu,s} + \rho_{240Pu}\sigma_{240Pu,s}$
- P_0 self-scattering cross-section in HDPE: $\sigma_{HDPE,s} = \rho_{1H}\sigma_{1H,s} + \rho_{12C}\sigma_{12C,s}$

We do not perturb any distribution quantities, such as the fission distribution χ, because it is ill-defined how to redistribute the effect of a energy-group perturbation (to ensure that the perturbed distribution still integrates to unity).

5.3 Bare BeRP Ball

First, we consider the truncation error of the bare BeRP ball. For all the moment calculations we used 39 spatial cells, about a factor of 10 less than our results in chap-three and chap-four, because we are more concerned with a self consistent comparison to measure a relative error and with the speed of calculation. We count the fraction of all perturbations for each parameter that pass our criterion, that the relative error is less than relative perturbation, in Table 5.1. As we would expect, our first-order approximation is valid for all parameters of the mean.

For the higher moments in Table 5.1, a fraction of our parameters start to fail our truncation error criterion. The downward coupling between moments means that the higher moment sensitivities grow and that the most sensitive parameters, the fission parameters from chap4-Collapse, are the ones that chiefly fail our passing criterion. We expect that the our criterion would fail for the fission cross-section and average neutron

Table 5.1: Fraction of first-order truncation error that meet passing criterion for the bare BeRP ball, considering perturbations between ± 10 %.

Parameter/Success	R_1	R_2	R_3
σ_d	1.0	1.0	1.0
Q	1.0	1.0	0.925
σ_f	1.0	0.986	0.949
$\overline{\nu}$	1.0	1.0	0.938
$\sigma_s : Pu$	1.0	1.0	1.0
$\overline{\nu(\nu-1)}$	—	1.0	1.0
$\overline{\nu(\nu-1)(\nu-2)}$	—	—	1.0

multiplicity $\overline{\nu}$, because they appear in the adjoint source terms and the transport operators, and they are the parameters to which R_2 and R_3 are most sensitive. The higher order neutron multiplicity moments, e.g. $\overline{\nu(\nu-1)}$, do not fail our criterion because they only appear in the source term and are less heavily coupled than terms that appear in all moment equations. The forward source Q fails for the third moment because of the increased sensitivity of source neutron induced fission chain-reactions that lead to detected triples.

We consider an energy versus relative perturbation error plot, for the bare BeRP ball in Figure 5.1, the third moment perturbation of the fission cross-section where we have set the error to 10^{-6} for any error less than 10^{-6}. The general features of the passing and failing parameters are seen in Figure 5.1, where there is minimal error below keV energies because of the small sensitivity coefficients in our fast system. The truncation error of a parameter is largest where the relative sensitivity coefficient is largest; for example the relative sensitivity coefficient of the third moment fission cross-section, recall Figure 4.2, is maximum around 1 MeV and the truncation error is largest there as well. The fraction of tests that fail our truncation criterion are where the sensitivity and absolute relative perturbation are largest.

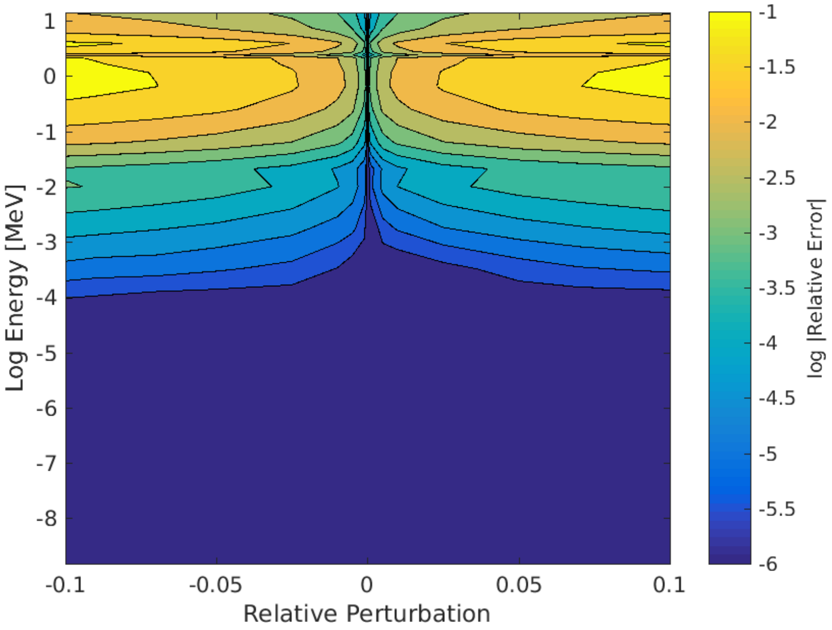

Figure 5.1: Truncation error of the fission cross-section for the third moment of the bare BeRP ball. Errors less than 10^{-6} have been set to 10^{-6}, as insignificant errors as small as 10^{-16} exist.

Our derived sensitivity analysis on the higher order moments of the neutron multiplicity counting distribution of the bare BeRP ball works for the majority of parameters across a wide range of perturbations. A conservative passing threshold for the truncation error would be ±5% for all parameters over all three moments. The great success of all passing fractions are greater than 90% for the bare BeRP ball is partially due to the lower energies, about half of the energy-groups, being insensitive due the fast fission system. The reflected BeRP ball truncation error study will involve a greater number of sensitive parameters to test.

5.4 Reflected BeRP Ball

Now, we perform the same truncation error analysis on the reflected BeRP ball. As in the bare case, we reduce the number of spatial cells to increase our speed of calculation; using 39 uniform spatial cells in the plutonium region and 39 cells in the reflector region, for a total of 78 uniform spatial cells. The angular quadrature and order of scattering remain the same. The addition of reflector increases the relative sensitivities of most parameters, recall chap-four, and the softened forward/adjoint spectra increases the influence of lower energy sensitivities, particularly between 1 eV and 1 keV. We tabulate the fraction of parameters that pass our truncation error criterion in Table 5.2, where we have the additional isotropic self-scattering cross-section of the reflector; it is also tied to changes in the total cross-section as in Eq. 5.6.

Table 5.2: Fraction of first-order truncation error that meet passing criterion for the 1.5 in HDPE reflected BeRP ball.

Parameter/Success	R_1	R_2	R_3
σ_d	1.0	1.0	1.0
Q	1.0	1.0	1.0
σ_f	0.951	0.906	0.879
$\overline{\nu}$	0.974	0.915	0.874
$\sigma_s : Pu$	1.0	1.0	1.0
$\overline{\nu(\nu-1)}$	—	1.0	1.0
$\overline{\nu(\nu-1)(\nu-2)}$	—	—	1.0
σ_s:HDPE	1.0	1.0	0.987

The first difference we note between the bare and reflected case is that the mean of the multiplicity counting distribution does not pass all relative perturbations for all parameters. However, the fission parameters are what we expect our system to be most sensitive to and we observe that with increasing moment the fraction of passing parameters decreases. Again, the only fission parameters that fail are the fission cross-section and the average multiplicity; the higher moments of the neutron multiplicity do not fail because they appear exclusively in source terms. The forward source does not fail at all for the third moment, as it did in the bare case, because of the decreased sensitivity of the source with regards to increasing moment (recall Figure 4.19), that is due to a diminished importance on slow neutrons because of the addition of moderator and an increase in overall neutron multiplication. The reflected system is sensitive to the self-scattering cross-section in the reflector as a small fraction of parameters fail for the third moment. These failings have to do with the balance between scattering and capture, but also with excess slowing down into unresponsive energies in the nPod detector.

Now we consider a representative failed parameter, the third moment with respect to fission cross-section, of the reflected BeRP ball in Figure 5.2. The truncation error is still largest in the same regions as the bare BeRP ball because the fast fissions have larger neuron multiplicity moments (recall Figure 3.3). The lower energies are nontrivial, compared to the bare case, but they pass the truncation error test criterion. The reflected third moment is very sensitive to the fission parameters, recall Figure 4.40. As seen in Figure 5.2, the error is largest for negative relative perturbations in the fast fission region for all the moments.

Overall, the reflected BeRP ball is more sensitive than the bare plutonium sphere. This is partially due to the a greater fraction of the parameters becoming relevant because of slowing down in the reflector. The more than doubling of the neutron multiplication between cases, recall Table 3.4, increases the overall sensitivity of the moments to fission chain-reactions. Conservatively the reflected BeRP ball passes our truncation error threshold for all moments and parameters at a maximum of ±2.5% perturbations. The

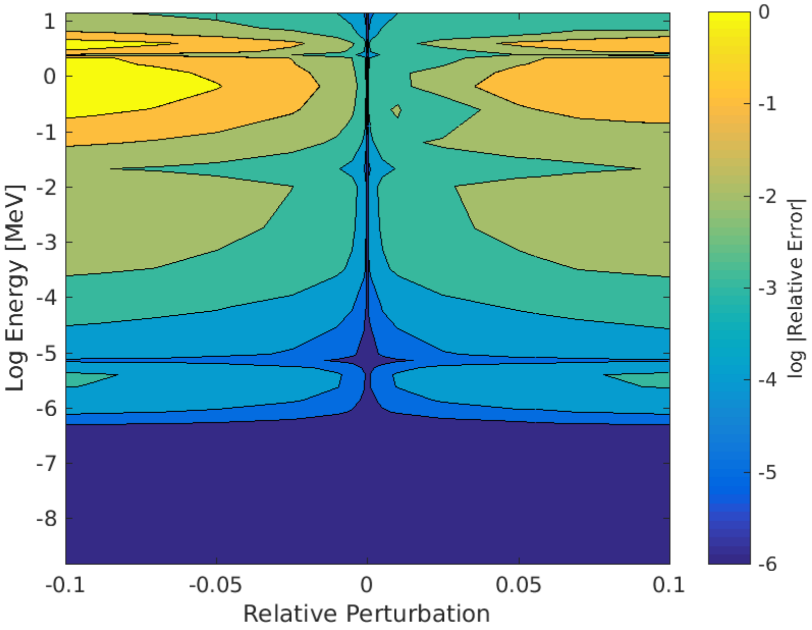

Figure 5.2: Truncation error of the fission cross-section for the third moment of the reflected BeRP ball.

fission parameters have large errors towards the maximum perturbations and there is no *a priori* reason to assume the true error surface is symmetric. However, the majority of our parameters, a minimum of $\approx 87\%$ pass our truncation error criterion.

5.5 Conclusion

We have shown that our first-order perturbation theory approximation is valid for a majority of parameters, across the first three moments, and for both the bare and reflected BeRP ball. The first-order approximation generally fails for the fission cross-section and the average neutron multiplicity for large perturbations, and has a lower passing rate for the reflected case. In conclusion, our first-order approximation of the downwardly coupled moment sensitivities is broadly applicable for a range of perturbations across all the system parameters, as long as the perturbations are on the order of a few percent.

Chapter 6

Conclusion

This dissertation has presented a method for determining the sensitivities of the moments of the neutron multiplicity counting distribution with respect to the transport parameters. Previous SA was only applicable to the mean of the counting distribution. Our work enables SA to arbitrarily high order moments of the counting distribution, where we have explicitly considered up to the third moment. Unlike earlier point-kinetics models of neutron multiplicity counting, we implement a full phase-space Boltzmann transport approach that removes many simplifying assumptions of point models. Our SA is applicable to all the transport parameters, such as cross-sections, nuclide densities, forward sources (including spontaneous fission with intrinsic multiplicities), and detector parameters. Our SA method is founded on standard first-order perturbation theory and ought to be applicable to other sensitivities not considered in this work, such as interface locations and boundary perturbations, that are successfully captured by adjoint founded SA theories.

Using the master moment generating equation and the source to detector moment generating function developed by Muñoz-Cobo in [5], we extracted the first three moment equations of the neutron multiplicity counting distribution. The moments of the counting distribution are inner products of adjoint fluxes with forward source multiplicities. The moment equations are fixed source adjoint transport equations, whose sources are functions of lower order moment adjoint fluxes. A downward coupling exists between the moments and our SA relies on new forward transport closing equations, whose fixed sources are a function of the forward flux, moment adjoint fluxes, and lower order closing equation fluxes. Our closing equations enable us to perform a complete and self-contained SA of the moments of the counting distribution to all the transport parameters. The calculation of the moments and the SA relies on solutions of the forward and adjoint transport equations with special fixed sources. The nature of the transport solves makes our method implementable in most deterministic transport solvers capable of fixed source forward and adjoints solves.

We validated our model for the moments of the neutron multiplicity counting distribution against experimental data of the BeRP ball, a sphere of plutonium metal, in both bare and polyethylene reflected configurations. Good agreement was found for both the reflected and bare BeRP ball for the first three moments. We determined the average count rates and considered the relative excess to Poisson statistics for the second (the Feynman-Y) and third moment.

With an accurate model we implemented our SA on the moments. The sensitivity of the transport parameters increases with increasing order moment because all the parameters are downwardly coupled. The sensitivity also increases with the addition of reflector, as compared to the bare BeRP ball, because the multiplication is greater and thermal energy group parameters now contribute. We ranked the energy group collapsed parameters and found that the moment equations are most sensitive to the fission parameters, in particular the fission cross-section and average induced neutron multiplicity.

We measured the truncation error in our first-order perturbation theory approximation and found that our SA is applicable for a reasonable range of relative perturbations. The first-order approximation fails for a small subset of parameters, mostly the fission parameters, at the largest relative perturbations. The fraction of parameters that fail our truncation error test increases with the order of moment and with the addition of reflector. However, at the worst $\approx 85\%$ of our perturbations, for a single parameter, pass. If perturbations are limited to $\approx 2.5\%$ all pass, where this threshold is determined by the third moment reflected BeRP ball case truncation error of the fission cross-section.

In summary, we have developed an effective SA method utilizing first-order perturbation theory for the moments of the neutron multiplicity counting distribution that uses full phase-space Boltzmann transport theory. Our SA method will improve nuclear data evaluation and enable uncertainty quantification of assays of SNM. Additional areas of application of SA of the moments of the neutron multiplicity counting distribution, of interest to the author, are in deterministic inverse solvers, sensitivities in hybrid Monte Carlo methods, and simulated data (detector data streams) of neutron multiplicity counting experiments.

REFERENCES

[1] N. Ensslin, W.C Harker, et al. Application guide to neutron multiplicity counting. Technical report, Los Alamos National Laboratory, 1998. LA-13422-M.

[2] E.C. Miller, J.K. Mattingly, S.D. Clarke, C.J. Solomon, B.Dennis, A. Meldrum, and S.A. Pozzi. Computational evaluation of neutron multiplicity measurements of polyethylene-reflected plutonium metal. *Nuclear Science and Engineering*, 176(2):167–185, 2014.

[3] Manoj K. Prasad and Neal J. Snyderman. Statistical theory of fission chains and generalized poisson neutron counting distributions. *Nuclear Science and Engineering*, 172:300–326, 2012.

[4] John Mattingly. Computation of neutron multiplicity statistics using deterministic transport. *IEEE Trans. on Nuclear Sci.*, 59(2), 2012.

[5] Jose-Louse Munoz-Cobo, R.B Perez, et al. Stochatic neutron transport theory. *Nuclear Science and Engineering*, 95:83–105, 1987.

[6] N. Ensslin. A simple self-multiplication correction for in-plant use. In *Proc. 7th ESARDA Symposyium on Safeguards and Nuclear Material Management*, Liege, Belgium, May 1985.

[7] H.O. Menlove, R. Abedin-Zadeh, and R. Zhu. The analysis of neutron coincidence data to verify both spontaneous fission and fissionalbe isotopes. Technical report, Los Alamos National Laboratory, 1989. LA-11639-MS.

[8] R.L. Macklin, F.M. Glass, J. Halperin, et al. Neutron multiplicity counter. *Nuclear Instruments and Methods*, 102:181–187, 1972.

[9] T.D. Reillya, N. Ensslin, and H.A. Smith. Passive nondestructive assay of nuclear materials. Technical report, US Nuclear Regulatory Commission, 1991. NUREG/CR-5550.

[10] M.E. Abhold and M.C. Baker. Mcnp-ren a monte carlo tool for neutron detector design. *Nuclear Instruments and Methods*, A485(3):576–584, 2002.

[11] J.E. Stewart. Hybrid monte carlo/analytical model of neutron coincidence counting. In *Proc. American Nuclear Society*, Washington, DC, USA, Nov 1986.

[12] N. Ensslin, M.S. Krick, and N. Dytlewski. Assay variance as a figure-of-merit for neutron multiplicity counting. *Nuclear Instruments and Methods*, A290:197–207, 1990.

[13] R.P. Feynman, F. De Hoffmann, and R. Serber. Dispersion of the neutron emission in u-235 fission. *J. Nuclear Energy*, 3:64–69, 1956.

[14] M.S. Zucker and N.E. Holden. Energy dependence of neutron multiplicity p_ν in fast-neutron-induced fission for $^{235,238}u$ and ^{239}pu. Technical report, Brookhaven National Laboratory, 1986. BNL-38491.

[15] J. Terrell. Distributions of fission neutron numbers. *Phys. Rev.*, 108(3):783–789, 1957.

[16] J.M. Verbeke, C. Hagmann, and D. Wright. Simulation of neutron and gamma ray emission from fission and photofission. Technical report, Lawrence Livermore National Laboratory, 2010. UCRL-AR-228518.

[17] J.W. Boldeman and M.G. Hines. Prompt neutorn emmission probabilities following spontaneous and thermal neutron fission. *Nuclear Science and Engineering*, 91(1):114–116, 1985.

[18] K. Boehnel. The effect of multiplication on the quantitative determination of spontaneously fissioning isotopes by neutron correlation analysis. *Nuclear Science and Engineering*, 91(114), 1985.

[19] A. Gavron and Z. Fraenkel. Neutron correlations in spontaneous fission of ^{252}cf. *Physical Review*, C(9), 1974.

[20] H.Y. Lee et al. Prompt fission neutron spectrum study at lansce: Chi-nu project. In *Fission and Properties of Neutron-Rich Nuclei, Proceeding of the Fifth International Conference on ICFN5*, Sanibel Island, Fl, USA, November 2012.

[21] D.G. Langner and P.A. Russo. Geometry-based multiplication correction for passive neutron coincidence assay of materials with variable and unknown (α,n) neutron rates. Technical report, Los Alamos National Laboratory, 93. LA-12504-MS.

[22] W. Hage and D.M. Cifarreli. Correlation analysis with neutron count distributions in randomly or signal triggered time intervals for assay of special nuclear materials. *Nuclear Instruments and Methods*, A236(165), 1985.

[23] D.M. Cifarelli and W. Hage. Models for a three-parameter analysis of neutron signal correlation measurements for fissile material assay. *Nuclear Inst. and Meth. in Phys. Research*, A251:550–563, 1986.

[24] I. Pazsit and L. Pal. *Neutron Fluctuations*. Elsevier, USA, 2008.

[25] L. Pal. On the theory of stochastic processes in nuclear reactors. *Nuovo Cimento*, 7:25–42, 1958.

[26] George I. Bell. Probability distribution of neutron and precursors in a multiplying assembly. *Annals of Physics*, 21:243–283, 1963.

[27] J. Lewins. Linear stochastic neutron transport theory. *Proc. R. Soc. London A.*, 362:537–558, 1978.

[28] Jose-Louse Munoz-Cobo and G. Verdu. Neutron stochastic transport theory with delayed neutrons. *Ann. Nucl. Energy*, 14(7):327–350, 1987.

[29] Erin D. Fichtl and Randal S. Baker. Computing the moments of the neutron population using deterministic transport. In *Proceeding of ANS M&C*, Sunvalley, ID, April 2013.

[30] J.J. Duderstadt and L.J Hamilton. *Nuclear Reactor Analysis.* John Wiley and Sons, New York, USA, 1976.

[31] J. Lewins. *Importance, the Adjoint Function.* Elsevier, USA, 1965.

[32] E. Greenspan. New developments in sensitivity theory. *Adv. in Nuclear Sci. and Tech.*, 14, 1982.

[33] R.C. Smith. *Uncertainty Quantification.* SIAM, USA, 2014.

[34] R.T. Evans, J.K. Mattingly, and D.G. Cacuci. Sensitivity analysis and data assimilation in a subcritical plutonium metal benchmark. *Nuclear Science and Engineering*, 167(3):325–338, 2014.

[35] W.C. Proctor. *Elements of High-Order Predictive Model Calibration Algorithms with Applications to Large-Scale Reactor Physics Systems.* PhD thesis, North Carolina State University, 2012.

[36] R.E. Alcouffe, R.S. Baker, J.A. Dahl, et al. *PARTISN: A Time-Dependent, Parallel Neutral Particle Transport Code System*, 2008. LA-UR-08-07258.

[37] E.E. Lewis and W.F. Miller. *Computational Methods of Neutron Transport.* American Nuclear Society, Inc., Lagrange Park, USA, 1993.

[38] J.K. Mattingly. Polyethylene-reflected plutonium metal sphere: Subcritical neutron and gamma measurements. Technical report, Sandia National Laboratories, 2009. SAND2009-5804.

[39] E.C. Miller, J.K. Mattingly, et al. Simulations of neutron multiplicity measurements with mcnp-polimi. Technical report, Sandia National Laboratories, 2010. SAND2010-6830.

APPENDIX

Appendix A

Appendix

A.1 Generating Function Examples

The probability generating function is a special case of the polynomial index function (PIF), where the order of the polynomial term serves to order a set. For example, the ordered set $1, 2, 3, 4$ would be represented as a PIF as $1 + 2z + 3z^2 + 4z^3$. The dummy variable z serves to indicate the order in the set.

The PGF is a special case of a PIF, where the coefficients are probabilities associated with the order of z. The general form of a PGF is

$$G(z) = \sum_{n=0}^{\infty} p_n z^n \tag{A.1}$$

where p_n is the probability of n coincident neutrons. The utility of a PGF comes in the ease of determining moments of their probability distributions. First, consider the zeroth moment, the sum of all probabilities, which must be equal to one for our function to be classified as a PGF and not a PIF. The zeroth moment, μ_0, is arrived at by setting the index/dummy variable to one, $z = 1$.

$$\begin{aligned} \mu_0 &= G(z)|_{z=1} \\ &= \sum_{n=0}^{\infty} p_n \\ &= 1 \end{aligned} \tag{A.2}$$

To determine the mean, μ_1, of the distribution we differentiate with respect to z and set $z = 1$.

$$\begin{aligned} \mu_1 &= \frac{\partial G(z)}{\partial z}\Big|_{z=1} \\ &= \sum_{n=0}^{\infty} n p_n z^{n-1}\Big|_{z=1} \\ &= \sum_{n=1}^{\infty} n p_n \end{aligned} \tag{A.3}$$

$$= \overline{n} \tag{A.4}$$

where the over-bar denotes the expected value, or mean, of n. We compute the factorial moment of order q by taking the q^{th} derivative of the PGF with respect to z and setting $z = 1$.

$$\begin{aligned} \mu_q &= \frac{\partial^q G(z)}{\partial z^q}\Big|_{z=1} \\ &= \overline{n(n-1)\ldots(n-q+1)} \end{aligned} \tag{A.5}$$

A useful property of PGF's, applicable to our study of neutron counting statistics, is the treatment of an ensemble of independent objects. The PGF for N independent objects is simply the PGF for a single object raised to the power of N. This principle hold for an ensemble of neutrons. Assume we have a beam of mono-energetic neutrons impinging on a pure absorbing slab at $x = 0$ traveling to the right. The PGF for a single neutron is:

$$\begin{aligned} G_1(x,z) &= \left(1 - e^{-\sigma_a x}\right) + e^{-\sigma_a x} z \\ &= (1 - p(x)) + p(x) z \end{aligned} \tag{A.6}$$

where $p(x) = e^{-\sigma_a x}$ and σ_a is the macroscopic absorption cross section. This PGF satisfies the requirement that $\mu_0 = 1$ and the mean/expectation of finding a neutron at x is $\mu_1(x) = e^{-\sigma_a x}$, as expected. If we have a collection of N-neutrons, that are independent (no neutron-neutron interactions or fission chains), the PGF is given by:

$$G_N(x,z) = [G_1(x,z)]^N \tag{A.7}$$

Again, the zeroth moment is unity and the mean, $\mu_1(x) = Ne^{-\sigma_a x}$, is the familiar attenuation function, arrived at by the standard transport equation. If each neutron is independent, then the probability of finding a given number of neutrons in a region of phase space is binomially distributed (A.8).

$$
\begin{aligned}
G &= \sum_{k=0}^{N} \begin{pmatrix} N \\ k \end{pmatrix} p^k (1-p)^{N-k} z^k \qquad \text{(A.8)} \\
&= \sum_{k=0}^{N} \begin{pmatrix} N \\ k \end{pmatrix} (pz)^k (1-p)^{N-k} \\
&= ((1-p) + pz)^N
\end{aligned}
$$

Where, again, $p = p(x) = e^{-\sigma_a x}$. This binomial distribution holds if we consider the full spatial, time, energy and angular dependence of the single neutron probability, $p(\vec{r}, \vec{\Omega}, E, t)$, where the independent variables are position, direction, energy and time. Any collection of independent neutrons obeys binomial statistics, which is approximated as Poisson statistics, when $N \to \infty$, $p \to 0$ and Np is finite, which is true of the neutron systems we consider.

Poisson statistics no longer apply if neutrons are not independent, as occurs in multiplying systems because the neutron population depends on previous interactions. To observe this, consider a single neutron in vacuum that interacts with an infinitesimal multiplying region, in which up to N neutrons can be produced. For the sake of simplicity assume these new neutrons move along the initial beam direction. The probability of producing m-neutrons is given by p_m, where $\sum_m p_m = 1$. The beam PGF is given by $G_{beam}(z) = z$ and after interacting with the multiplying region, the new neutron PGF is:

$$\begin{aligned} G(z) &= G_{beam}(z)\left(\sum_{m=0}^{N} p_m z^m\right) \\ &= G_{beam}(z)\left(\sum_{m=0}^{N} p_m G_{beam}(z)^m\right) \end{aligned} \tag{A.9}$$

which is clearly no longer Poisson/binomially distributed because the multiplicity of the fission chain creates dependencies between interactions.

A.2 Convergence Study

To ensure the reliability of our results we perform a spatial mesh and angular quadrature study for the first three moments (R_1, R_2, and R_3) for our comparrison cases of bare and 1.5*in* HDPE relected BeRP ball. We measured the converegence by the absolute error e using a highly refined case as our true solution.

$$e_i(X_n, S_n) = 1 - \frac{R_i(X_n, S_n)}{R_{i,true}} \tag{A.10}$$

where X_n is the number of uniform spatial cells and S_n is the order of angular quadrature, where only certain values are available in PARTISN. All PARTISN runs used 1-D spherical geometry and third-order scattering. Cross-section data was obtained from the 44-group ENDF-VII library that is packaged with the SCALE 6.1 software suite.

A.2.1 Bare BeRP

For our "true" solution we used $X_n = 2048$ spatial cells and $S_n = 48$ angular quadrature, the maximum available in PARTISN. Where the "true" values are:

$$\begin{aligned} R_{1,true} =& 8324.89806157 \\ R_{2,true} =& 2645.78477295 \\ R_{3,true} =& 2408.90791369 \end{aligned} \tag{A.11}$$

The values used in our SA were done using $X_n = 379$ spatial cells and $S_n = 32$ angular quadrature, and are sufficiently converged for our purposes as seen in Eq. A.12

$$\begin{aligned} R_1 =& 8328.80875129 \\ R_2 =& 2649.82144122 \\ R_3 =& 2415.38053785 \end{aligned} \tag{A.12}$$

We observe the nature of convergence across space and angle, noting that the convergence is most sensitive to the order of angular quadrature, in Table A.1 for the mean, in Table A.2 for the second moment excesss, and in Table A.3 for the third moment excess.

Table A.1: Convergence bare mean.

Xn/Sn	2	4	6	8	12
4	-0.05927	-0.04856	-0.02502	-0.01651	-0.01022
8	-0.05258	-0.04490	-0.02189	-0.01353	-0.007129
16	-0.05045	-0.04355	-0.02060	-0.01222	-0.005803
32	-0.04989	-0.04318	-0.02025	-0.01185	-0.005426
64	-0.04975	-0.04309	-0.02015	-0.01176	-0.005329
128	-0.04971	-0.04306	-0.02013	-0.01174	-0.005304
256	-0.04970	-0.04306	-0.02013	-0.01173	-0.005298
512	-0.04970	-0.04306	-0.02012	-0.01173	-0.005297
1024	-0.04970	-0.04306	-0.02012	-0.01173	-0.005296
2048	-0.04970	-0.04306	-0.02012	-0.01173	-0.005296
Xn/Sn	16	20	24	32	48
4	-0.007958	-0.006897	-0.006315	-0.005725	-0.005303
8	-0.004742	-0.003603	-0.002974	-0.002344	-0.001887
16	-0.003412	-0.002266	-0.001631	-0.0009876	-0.0005204
32	-0.003030	-0.001882	-0.001246	-0.0006021	-0.0001333
64	-0.002931	-0.001784	-0.001147	-0.0005025	-3.378×10^{-5}
128	-0.002906	-0.001758	-0.001121	-0.0004770	-8.705×10^{-6}
256	-0.002900	-0.001752	-0.001115	-0.0004711	-2.277×10^{-6}
512	-0.002898	-0.001750	-0.001114	-0.0004694	-1.357×10^{-7}
1024	-0.002898	-0.001750	-0.001113	-0.0004690	-5.876×10^{-8}
2048	-0.002898	-0.001750	-0.001113	-0.0004690	0.0

Table A.2: Convergence bare second moment.

Xn/Sn	2	4	6	8	12	16	20	24	32	48
4	-0.2068	-0.1503	-0.06312	-0.03391	-0.01230	-0.005539	-0.002075	-0.0001753	0.001741	0.003115
8	-0.1997	-0.1549	-0.06871	-0.03966	-0.01819	-0.01033	-0.006607	-0.004559	-0.002505	-0.001017
16	-0.1961	-0.1545	-0.06847	-0.03932	-0.01776	-0.009864	-0.006107	-0.004037	-0.001938	-0.0004211
32	-0.1951	-0.1543	-0.06829	-0.03911	-0.01750	-0.009584	-0.005820	-0.003738	-0.001642	-0.0001163
64	-0.1949	-0.1542	-0.06823	-0.03904	-0.01742	-0.009450	-0.005736	-0.003655	-0.001556	-3.048×10^{-5}
128	-0.1948	-0.1542	-0.06822	-0.03903	-0.01740	-0.009479	-0.005713	-0.003632	-0.001531	-8.459×10^{-6}
256	-0.1948	-0.1542	-0.06821	-0.03902	-0.01740	-0.009475	-0.005709	-0.003628	-0.001528	-2.275×10^{-6}
512	-0.1948	-0.1542	-0.06821	-0.03902	-0.01739	-0.009472	-0.005707	-0.003625	-0.001526	9.214×10^{-7}
1024	-0.1948	-0.1542	-0.06821	-0.03902	-0.01739	-0.009472	-0.005706	-0.003626	-0.001525	9.886×10^{-8}
2048	-0.1948	-0.1542	-0.06821	-0.03902	-0.01739	-0.009472	-0.005707	-0.003626	-0.001525	0.0

Table A.3: Convergence bare third moment.

Xn/Sn	2	4	6	8	12	16	20	24	32	48
4	-0.4174	-0.2771	-0.1081	-0.05445	-0.01670	-0.003845	0.002253	0.005587	0.008939	0.01135
8	-0.4116	-0.2920	-0.1236	-0.06976	-0.03101	-0.01702	-0.01043	-0.006817	-0.003195	-0.0005753
16	-0.4060	-0.2924	-0.1242	-0.07018	-0.03122	-0.01715	-0.01050	-0.006836	-0.003134	-0.0004618
32	-0.4043	-0.2922	-0.1241	-0.07003	-0.03098	-0.01688	-0.01020	-0.006525	-0.002826	-0.0001391
64	-0.4039	-0.2922	-0.1241	-0.06997	-0.03089	-0.01678	-0.01011	-0.006429	-0.002724	-3.688×10^{-5}
128	-0.4038	-0.2922	-0.1241	-0.06996	-0.03087	-0.01676	-0.01008	-0.006401	-0.002694	-1.053×10^{-5}
256	-0.4038	-0.2922	-0.1240	-0.06995	-0.03087	-0.01675	-0.01007	-0.006395	-0.002690	-2.519×10^{-6}
512	-0.4038	-0.2922	-0.1240	-0.06995	-0.03087	-0.01675	-0.01007	-0.006393	-0.002687	1.496×10^{-6}
1024	-0.4038	-0.2922	-0.1240	-0.06995	-0.03087	-0.01675	-0.01007	-0.006393	-0.002686	3.604×10^{-7}
2048	-0.4038	-0.2922	-0.1240	-0.06995	-0.03087	-0.01675	-0.01007	-0.006393	-0.002687	0.0

A.2.2 Convergence $1.5in$ HDPE mean.

For our "true" solution we used $X_n = 4096$ spatial cells, in order to keep the spatial size of the cells nearly the same between the bare and reflected case, shared evenly between the plutonium and HDPE regions, and $S_n = 48$ angular quadrature, the maximum available in PARTISN. Where the "true" values are:

$$\begin{aligned} R_{1,true} &= 18086.860526 \\ R_{2,true} &= 28388.6139639 \\ R_{3,true} &= 129652.092142 \end{aligned} \tag{A.13}$$

The values used in our SA were done using $X_n = 379$ spatial cells in the BeRP ball, and $X_n = 381$ spatial cells in the HDPE. Again, we used $S_n = 32$ angular quadrature. Our choice of discretizations are sufficiently converged for our purposes as seen in Eq. A.14

$$\begin{aligned} R_1 &= 18113.316662 \\ R_2 &= 28504.8740002 \\ R_3 &= 130534.183416 \end{aligned} \tag{A.14}$$

We observe the nature of convergence across space and angle, noting that the convergence is most sensitive to the order of angular quadrature, in Table A.4 for the mean, in Table A.5 for the second moment excesss, and in Table A.6 for the third moment excess.

Table A.4: Convergence HDPE mean.

Xn/Sn	2	4	6	8	12	16	20	24	32	48
8	-2.179	-0.2404	-0.1092	-0.07405	-0.04697	-0.03774	-0.03329	-0.03094	-0.02798	-0.02600
16	-1.628	-0.2209	-0.1053	-0.07075	-0.04749	-0.03863	-0.03462	-0.03219	-0.02982	-0.02812
32	-1.445	-0.1969	-0.08690	-0.05475	-0.03243	-0.02449	-0.02071	-0.01853	-0.01635	-0.01477
64	-1.371	-0.1834	-0.07600	-0.04478	-0.02324	-0.01548	-0.01181	-0.009800	-0.007737	-0.006229
128	-1.342	-0.1773	-0.07080	-0.03988	-0.01863	-0.01104	-0.007445	-0.005451	-0.003450	-0.001978
254	-1.329	-0.1752	-0.06898	-0.03811	-0.01690	-0.009336	-0.005771	-0.003806	-0.001824	-0.0003783
512	-1.327	-0.1747	-0.06863	-0.03780	-0.01658	-0.009016	-0.005450	-0.003483	-0.001507	-0.00006740
1024	-1.327	-0.1746	-0.06855	-0.03772	-0.01651	-0.008958	-0.005393	-0.003426	-0.001448	-1.107×10^{-5}
2048	-1.327	-0.1746	-0.06855	-0.03771	-0.01650	-0.008946	-0.005382	-0.003416	-0.001440	-1.839×10^{-6}
4096	-1.327	-0.1746	-0.06854	-0.03771	-0.01650	-0.008945	-0.005380	-0.003414	-0.0014370	0.0

Table A.5: Convergence HDPE second moment.

Xn/Sn	2	4	6	8	12	16	20	24	32	48
8	-10.26	-0.4809	-0.09903	-0.008059	0.05118	0.07094	0.08011	0.08504	0.09034	0.09411
16	-11.38	-0.6772	-0.2470	-0.1412	-0.07505	-0.05168	-0.04090	-0.03480	-0.02884	-0.02462
32	-10.85	-0.6642	-0.2394	-0.1356	-0.06997	-0.04745	-0.03685	-0.03092	-0.02499	-0.02067
64	-10.41	-0.6394	-0.2225	-0.1208	-0.05652	-0.03440	-0.02401	-0.01833	-0.01260	-0.008420
128	-10.24	-0.6283	-0.2147	-0.1138	-0.05010	-0.02823	-0.01795	-0.01232	-0.006673	-0.002552
254	-10.17	-0.6247	-0.2121	-0.1114	-0.04783	-0.02603	-0.01580	-0.01019	-0.004574	-0.0004779
512	-10.16	-0.6239	-0.2116	-0.1110	-0.04742	-0.02561	-0.01538	-0.009783	-0.004163	-8.994×10^{-5}
1024	-10.16	-0.6237	-0.2115	-0.1109	-0.04734	-0.02554	-0.01532	-0.009701	-0.004086	-6.846×10^{-6}
2048	-10.16	-0.6237	-0.2115	-0.1109	-0.04732	-0.02553	-0.01531	-0.009690	-0.004076	2.268×10^{-6}
4096	-10.16	-0.6237	-0.2115	-0.1109	-0.04732	-0.02552	-0.01531	-0.009696	-0.004080	0.0

Table A.6: Convergence HDPE third moment.

Xn/Sn	2	4	6	8	12	16	20	24	32	48
8	-39.72	-0.7625	-0.07892	0.06415	0.1499	0.1777	0.1904	0.1973	0.2044	0.2095
16	-59.10	-1.311	-0.4027	-0.2108	-0.09694	-0.05826	-0.04050	-0.03074	-0.02121	-0.01443
32	-58.39	-1.330	-0.4146	-0.2218	-0.1066	-0.06828	-0.05041	-0.04053	-0.03068	-0.02353
64	-55.91	-1.291	-0.3930	-0.2037	-0.09066	-0.05296	-0.03544	-0.02590	-0.01634	-0.009394
128	-54.95	-1.274	-0.3831	-0.1954	-0.08325	-0.04590	-0.02853	-0.01907	-0.009622	-0.002749
254	-54.61	-1.268	-0.3800	-0.1926	-0.08072	-0.04350	-0.02619	-0.01677	-0.007356	-0.0004938
512	-54.55	-1.267	-0.3794	-0.1921	-0.08028	-0.04304	-0.02575	-0.01632	-0.006901	-9.929×10^{-5}
1024	-54.54	-1.267	-0.3793	-0.1920	-0.08020	-0.04298	-0.02567	-0.01622	-0.006816	-1.193×10^{-6}
2048	-54.54	-1.267	-0.3793	-0.1920	-0.08018	-0.04297	-0.02567	-0.01621	-0.006807	1.521×10^{-5}
4096	-54.54	-1.267	-0.3793	-0.1920	-0.08016	-0.04295	-0.02567	-0.01621	-0.006806	0.0

A.3 Sensitivity Coefficients

For a complete sensitivity analysis the P_0 double differential scattering cross-section relative sensitivities are included here. Many of the trends seen in chap-four between increasing moment and the effect of adding reflector are present here. First, we consider the scattering sensitivity of plutonium and compare, for each moment, the bare and reflected cases. Next, we compare the sensitivity of hydrogen and carbon for each moment.

A.3.1 Plutonium Differential Scattering

As with our previous SA, we only report the sensitivities of ^{239}Pu. The mean cross-section relative sensitivity in Figure A.1 shows that Pu is in not effective at slowing down neutrons. In the bare configuration, the thermal scattering sensitivity is especially small due to the minimal flux in this energy domain. The addition of reflector increases the sensitivity in the thermal regions by many orders of magnitude, because the thermal neutron population has grown. The maximum sensitivity has increased by a factor of one hundred in the reflected case because multiple scatterings are possible because of reflection.

The second moment in Figure A.2 and third moment in Figure A.3 relative sensitivities follow the same trends. Where the addition of reflector increases slow region sensitivities.

The maxiumum sensitivity is about the same between the bare and relfected cases, across the second and third moments, because doubles and triples are more sensitive to down-scatter and capture, which competes with fission.

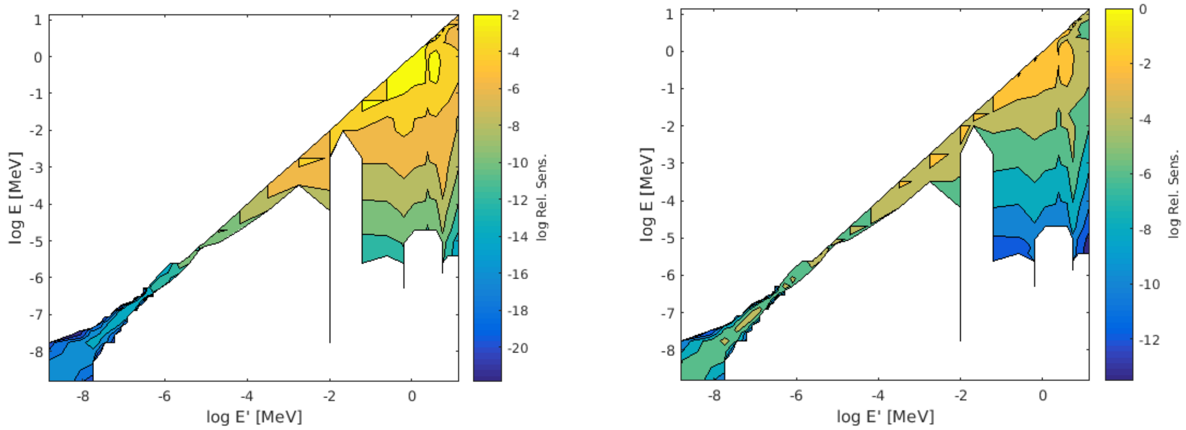

Figure A.1: Mean relative sensitivity coefficient for double differential scattering cross section of ^{239}Pu for the bare (left) and reflected (right) BeRP ball.

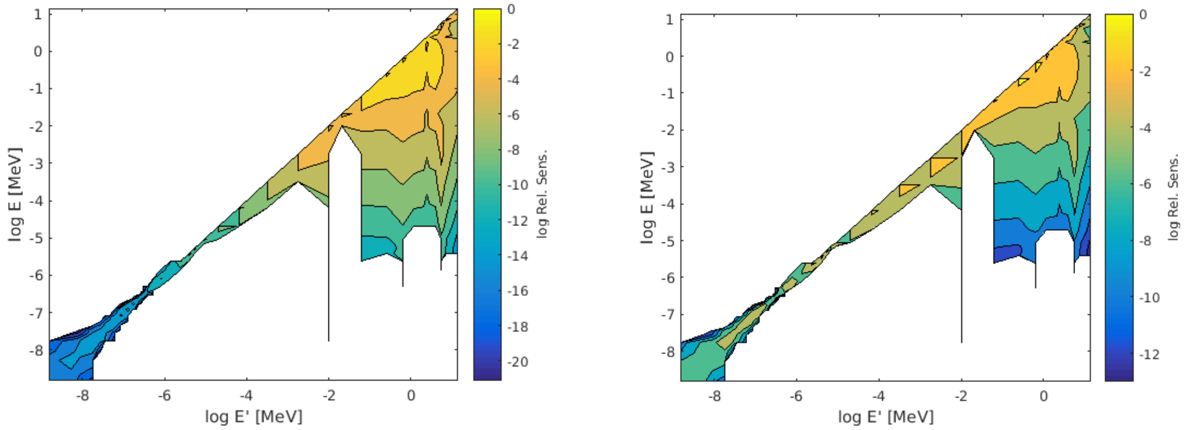

Figure A.2: Second moment relative sensitivity coefficient for double differential scattering cross section of ^{239}Pu for the bare (left) and reflected (right) BeRP ball.

A.3.2 Polyethyelene Differential Scattering

The addition of reflector is what increases the multiplication and thus sensivitivity of the moments compared to the bare configuration. We compare the differential scattering cross-section relative sensitivities of hydrogen and carbon for each moment. We observe that hydrogen is a much more effective moderator due to its ability to slow a neutron

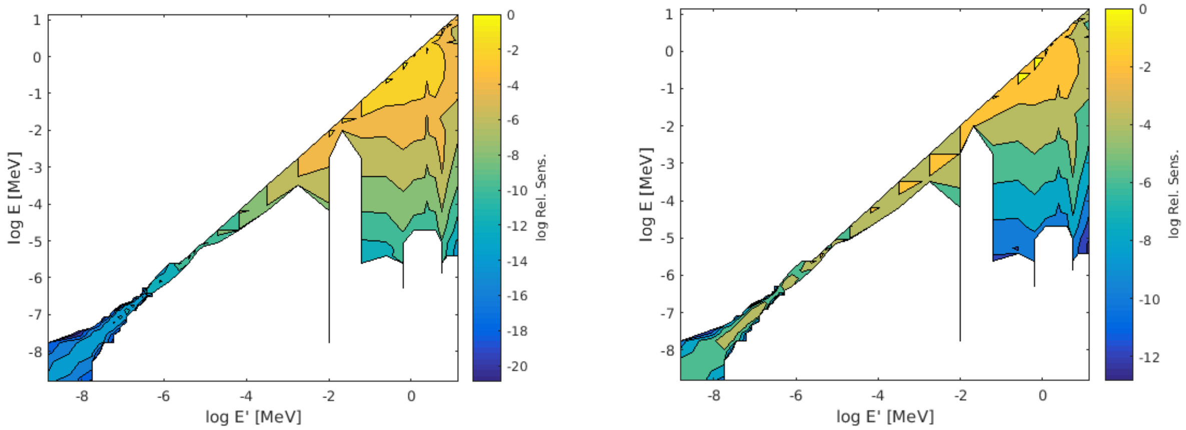

Figure A.3: Third moment relative sensitivity coefficient for double differential scattering cross section of ^{239}Pu for the bare (left) and reflected (right) BeRP ball.

with much fewer collisions than carbon.

For the mean, hydrogen is more sensitive than carbon as seen in Figure A.4. However, carbon has a larger minimum sensitivity because of the size of the cross-section in the relative sensitivity coefficient.

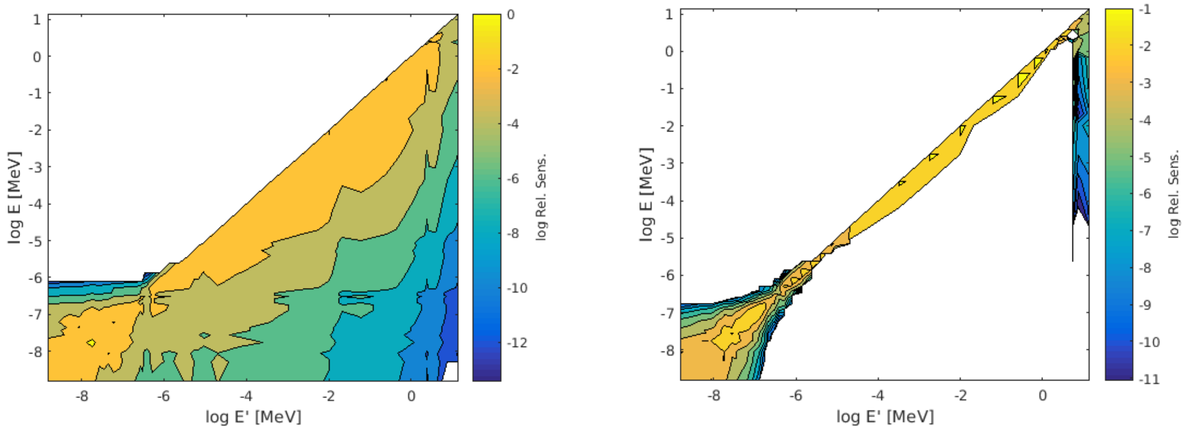

Figure A.4: Mean relative sensitivity coefficient for double differential scattering cross section for ^{1}H (left) and ^{12}C (right).

The second moment in Figure A.5 and the third moment in Figure A.6 relative sensitivities are generally the same, with a slight increase in the minimum sensitivity.

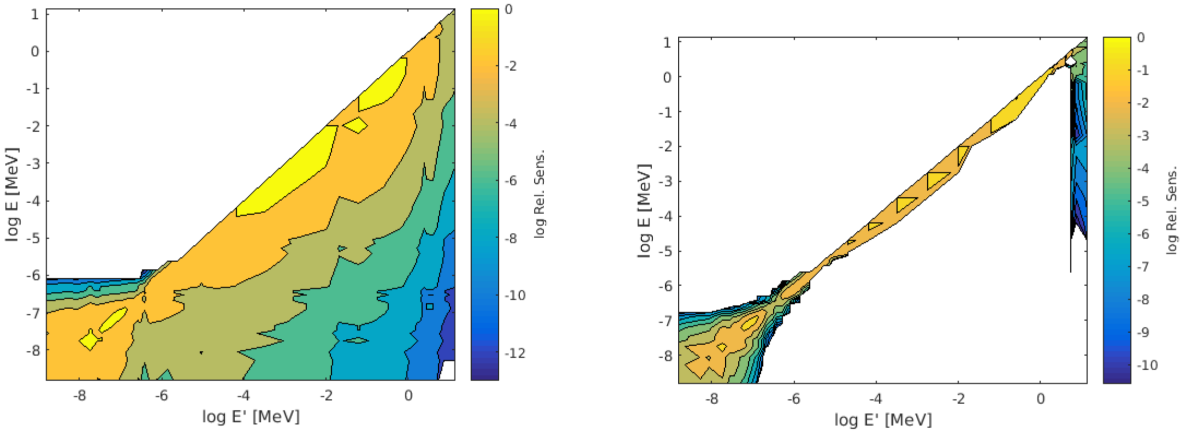

Figure A.5: Second moment relative sensitivity coefficient for double differential scattering cross section for ^{1}H (left) and ^{12}C (right).

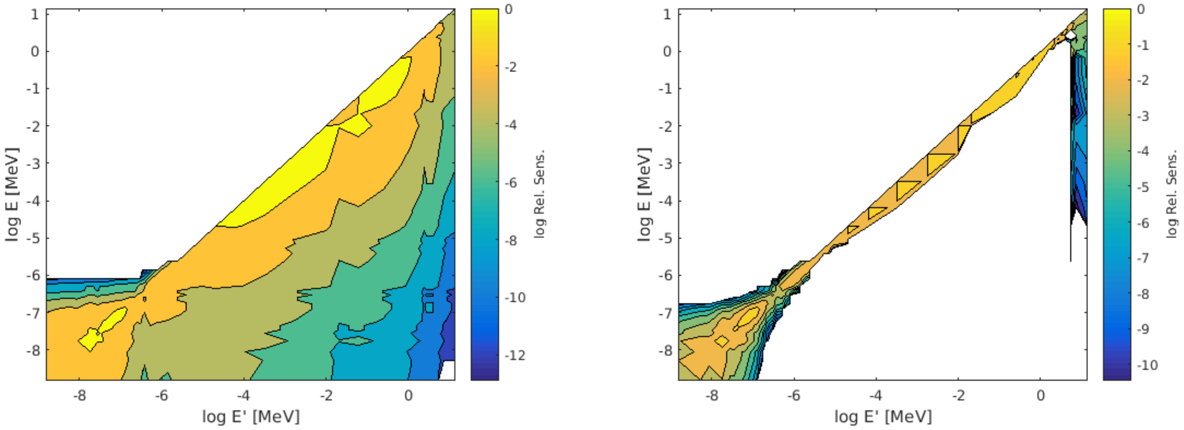

Figure A.6: Third moment relative sensitivity coefficient for double differential scattering cross section for ^{1}H (left) and ^{12}C (right).